Fabrication, Design and Characterization of Silicon-on-Insulator Waveguide Amplifiers Coated in Erbium-Doped Tellurium Oxide

Fabrication, Design and Characterization of Silicon-on-Insulator Waveguide Amplifiers Coated in Erbium-Doped Tellurium Oxide

By Cameron Naraine, B.Sc.

A Thesis Submitted to the School of Graduate Studies in the Partial Fulfillment of the Requirements for the Degree Master of Applied Science

Master of Applied Science (August 2020)

Department of Engineering Physics

McMaster University

Hamilton, Ontario, Canada

TITLE: Fabrication, Design and Characterization of Silicon-on-Insulator Waveguide Amplifiers Coated in Erbium-Doped Tellurium Oxide

AUTHOR: Cameron Naraine, B.Sc. (McMaster University)

SUPERVISORS: Dr. Jonathan D. B. Bradley, Dr. Andy P. Knights

NUMBER OF PAGES: xiv, 116

Abstract

This research introduces tellurium oxide (TeO_2) glass doped with optically active erbium ions (Er^{3+}) as an active oxide cladding material for silicon-on-insulator (SOI) waveguides for realization of a silicon-based erbium-doped waveguide amplifier (EDWA) for integrated optics. Optical amplification of this nature is enabled by energy transitions, such as stimulated absorption and emission, within the shielded 4f shell of the rare-earth atomic structure caused by excitation from photons incident on the system. Er^{3+} ions are doped into the TeO_2 film during deposition onto the SOI waveguides using a reactive magnetron co-sputtering system operated by McMaster's Centre for Emerging Device Technologies (CEDT). Prior to fabrication, the waveguides are designed using photonic CAD software packages, for optimization of the modal behaviour in the device, and Matlab, for characterization of the optical gain performance through numerical analysis of the rate and propagation equations of the Er^{3+}-based energy system. Post fabrication, the waveguide loss and gain of the coated devices are experimentally measured. The fabricated waveguide amplifier produces a peak signal enhancement of 3.84 dB at 1533 nm wavelength for a 1.7 cm-long waveguide device. High measured waveguide losses ($>$ 10 dB/cm) produce a negative internal net gain per unit length. However, the demonstration and implementation of an active rare-earth doped cladding material on a silicon waveguide is successful, which is a major step in developing integrated optical amplifiers for conventional silicon photonics platforms.

Acknowledgements

So many people to thank!

Dr. Jonathan Bradley, my supervisor, whose door is always open for help, ideas and conversation. Your critical analysis helped me deeply understand what it takes to deliver quality research work, and your passion and enthusiasm for photonics overall not only strengthened my love for it, but also got me through tough days by keeping my head clear and my aim focused.

Dr. Andy Knights, my co-supervisor, without whom I would not have plentiful opportunities and relationships, such as those at NRC, creative insight towards problem-solving and analyzing information, as well as the drive necessary to push through obstacles and excel in this field. Your knowledge has been expressed throughout this work, and I would not be as versatile of a researcher without your expertise and guidance.

Dr. Pavel Cheben, my mentor at NRC Canada, for giving me a chance to prove myself as a researcher and supporting me throughout my work, both professionally and personally. I am excited to continue our work together during my Ph.D. project!

Dr. Jens Schmid, my other mentor at NRC Canada, whose keen mind and valuable insight opens doors for new ideas and provides solutions around every corner. Your in-depth wisdom of what is possible in our field brings many possibilities to light and keeps our work extremely interesting and appealing!

Dawson Bonneville, for bringing enthusiasm into the lab and displaying passion for the work I have grown to love and enjoy through this journey. You have taught me much about STEM as a whole and encourage me to think creatively about project ideas and solutions to problems.

Henry Frankis, for initiating this project, performing all my film depositions on a dime's notice, and developing the Matlab and Pyxis scripts for everyday tasks that we now probably consider to be trivial. I would be months behind where I am now had you not laid this groundwork for our group.

Khadijeh Miarabbas Kiani, for displaying ongoing devotion to her lab work and being kind to me at every turn in the road. I can always count on you for a favour or a genuine conversation.

Jeremy Miller, for originally taking the lead on and showing me the ropes of what will now be my Ph.D. project, and for being my partner in crime (for SWGs and thesis writing) who I could count on for advice or a pleasant conversation.

Bruno Luis Segat Frare, for picking up my slack on TAing and designing grating couplers while I focused on work terms, other projects and thesis writing. Your efforts do not go unnoticed, and I would be a completely overwhelmed wreck without you.

Chenglin Zhang, who reached out a helping hand when necessary, even if not physically present, and provided a good template and reference for this thesis.

Arthur Mendez-Rosales, who, back in the early days, taught me much about what it takes to be in these lab groups and provides fun, insightful and enthusiastic conversations about my two greatest passions: music and science.

My Knights Group colleagues, Matt Vukovic and Connor Wong, for being the best hotel buddies a guy could ask for whenever I visited (either to work or just to heat up my lunch in the microwave). You provided me sanity with silly shenanigans, great senses of humour and light-heated conversations about anything and everything.

To all the folks I have met and gotten to know at NRC Canada, thank you for including me in your everyday lunchroom group, sharing world-renowned foods with

me, and taking interest in the work I do.

The Johnston family (Connor, Gillian and Owen), for housing and feeding me during the COVID-19 pandemic and considering me a part of your family throughout the years I have known you. Without the lovely office space that you provided me, I would still be writing this thesis!

Courtney, my love, for your patience while I spend all of my time working, your support through all the hard times, your encouragement enabling me to shoot for the stars and live a fuller life, and your love that makes every day better than the last.

My family (mom, dad and Chris), for shaping me into the man I am today and for always giving me your love and support in all my endeavours. None of this would be possible without you.

And finally, to any other colleagues, peers, mentors and friends I may have missed, for everything you have done for me. Your presence was felt during this journey and it has helped to get me to where I am today.

Contents

List of Figures

List of Tables

Chapter 1

Introduction

1.1 Silicon photonics in integrated optics

The demand for internet connectivity is at an all-time high due to the continually advancing capabilities of enabling technology, such as computers, smart phones and smart devices, as well as the now ingrained status of online services, such as social media, streaming, e-commerce and cloud computing, in today's society. Fiber optic networks have adequately maintained this application over the years, providing solutions for data transmission that are now far too dense for electronic circuits and electrical copper-based channels, which are limited in terms of speed and distance due to susceptibility to electromagnetic interference and crosstalk, as well as high loss, heat generation and power consumption. However, as the need for higher bandwidth continues to skyrocket with the perpetual uprising of enterprises feeding the "Internet of Things" (IoT), fiber optic solutions are becoming too large and bulky, particularly for data center applications, and new solutions for such infrastructure will be required very soon to avoid being trampled over by the ever-increasing data traffic.

Integrated optics has been developing over the years with the hope of realizing a full system-on-a-chip that is capable of transmitting, receiving, emitting, amplifying,

guiding, modulating and detecting light signals that carry our precious information [1]. Chips of this nature, often referred to as **photonic integrated circuits** (PICs), offer the main benefit of footprint reduction over fiber optics with sizes on the micron- and sub-micron-scales. One of the greatest applications of PIC implementation lies in optical interconnects for data centers, high-performance computers, microprocessor data buses and server rack interconnects, which primarily run on electronic framework that is limited in terms of speed, power consumption, latency, and, more importantly, bandwidth and data density [2, 3]. Electrical-optical (E-O) conversion on **integrated circuits** (ICs) is currently of prime importance as purely optical solutions are far from ready for full-scale implementation of such applications [4]. Nevertheless, the search for a singular medium in which such interconnects and a so-called "optical superchip" may be realized is still ongoing.

Silicon has dominated the microelectronics industry as the primary ingredient in electronic components such as transistors and ICs. Because of this, it continues to receive plenty of attention as an easily accessible and inexpensive material solution for PICs and integrated optical devices. This has spawned the widely accepted and ever-expanding field of **silicon photonics** (SiP), which studies the optical properties of silicon and the design and fabrication of silicon-based devices for generating, manipulating and detecting light. The most notorious platform for SiP and PICs is **silicon-on-insulator** (SOI), which consists of a silica-silicon-silica sandwich arrangement atop a durable silicon handle for support. The high index contrast between the thin silicon layer ($n \sim 3.5$) and its surrounding silica neighbours ($n \sim 1.45$) enables high confinement of light within the silicon through the principles of total internal reflection, providing miniaturization of optical processing to the sub-micron scale. SOI is compatible with highly accurate and mature **complimentary-metal-oxide-semiconductor** (CMOS) technology that has led to high yield, robust and reproducible silicon-based circuits [4]. Furthermore, silicon has an optical transparency window between 1.1 μm and 8.5 μm with low-loss,

low-dispersion peaks near 1.3 μm and 1.55 μm, making it a very suitable medium for modern day telecommunications [5, 6]. From an initial overview, these benefits would appoint silicon to take the integrated photonics industry by storm. However, a deeper investigation of silicon reveals several issues that prevent it from enabling every optical functionality that would deem it "the one material to rule them all" in photonics.

Intrinsically, silicon suffers as an **indirect bandgap** material. In its bandstructure, the minima of the conduction band and maxima of the valence band are not aligned, signifying different momentum values and an offset in k space. Thus, before electron-hole (e-h) radiative recombination can occur between these bands, there must be a shift in momentum, which is accomplished by absorption or emission of a phonon, or lattice vibration. This type of band to band transition does not conserve momentum, so the likeliness of radiative recombination is extremely low [6]. Non-radiative recombination of e-h pairs is dominant in intrinsic silicon due to short non-radiative and long radiative lifetimes. The internal quantum efficiency, or ratio of probabilities of excited e-h pair radiative recombination versus overall e-h pair recombination, is on the scale of 10^{-6} [7, 8]. Indirect bandgap material such as silicon are also highly susceptible to **two photon absorption** (TPA), an optical nonlinear absorption process which involves simultaneous absorption of two light quanta (i.e. photons) that typically results in optical power depletion [9]. Silicon also does not exhibit the first order electro-optic effect known as Pockel's effect very well, which is a traditional characteristic for fast modulation of light enabled by small changes in material refractive index caused by an applied electric field [1, 8]. As a result of all these conditions (indirect bandgap, low quantum efficiency, intrinsic second-order nonlinearity, low electro-optic coefficient), silicon alone is an inefficient emitter of light [1, 3, 8, 10]. Integration of an on-chip light source is essential to the SOI platform as its high index contrast results in high propagation losses caused by sidewall scattering and high fiber-chip coupling loss [3]. Thus, the exploration of other solutions to on-chip light amplification in silicon-based

devices is still ongoing.

1.2 Optical amplification

Amplification of optical signals is required in optical systems to restore light that has deteriorated in a waveguiding medium, such as optical fibers and waveguides. In the late 1980s, the **erbium-doped fiber amplifier** (EDFA) was successfully demonstrated and enabled the development of multichannel wavelength division multiplexing (WDM) systems that heavily increased the bandwidth in long-haul optical communications, which require signal regeneration every few tens of kilometers as light travelled through globetrotting fiber lengths [11]. This method of amplification uses excitation properties of **erbium**, a lanthanide, or rare-earth element, through the process of stimulated emission of photons. A similar approach of optical amplification used in EDFAs may also be applied on-chip for interconnects and integrated devices, which require light amplification to restore signals for efficient detection that is essential to E-O signal conversion [4]. Generally, these miniaturized amplifiers are known as **erbium-doped waveguide amplifiers** (EDWAs).

Some methods of on-chip light amplification have sought to avoid silicon and its indirect bandgap. This includes the developments of III-V-based semiconductor optical amplifiers (SOAs), which utilize electrical pumping schemes rather than optical ones. However, their multi-step fabrication process is hard to manipulate on a mass production scale, part of which involves additional bonding steps of epitaxial layers onto already well-established silicon waveguide platforms to avoid issues relating to lattice mismatch [12]. In contrast, less complex approaches that still include silicon have been tried, such as silicon-based Raman amplifiers, which utilize interactions between optical fields and crystal lattice oscillations to induce stimulated Raman scattering for light amplification. However, strong free carrier absorption (FCA), usually in the form of TPA, limits the

efficiency of Raman gain at high pump powers, giving net loss [3]. Direct doping of silicon with optically active materials, such as erbium, has also been explored, but challenges ranging from impeccable fabrication precision and high potential for optically inactive dopants to poor room-temperature performance and monolithic integration with other photonic components have hindered the prospects of achieving of a commercially viable silicon-based amplifier device of this nature [10].

Another plausible solution to constructing a silicon-based light source is via hybridization of silicon with functional active cladding materials. This approach is simple in terms of fabrication and has been demonstrated in various media, including alumina (Al_2O_3), silica (SiO_2) and fluoride-based glasses [13]. In this thesis, we propose another viable candidate as an integrated cladding material for all-optical amplification on silicon-based devices.

1.3 Tellurium oxide thin films for optical amplification

Tellurite-based glasses have an outstanding history in the development of optical communication fiber networks [14]. Their most common form, **tellurium oxide** (TeO_2), is an amorphous glass material with significant potential as a high index waveguide material (n ~ 2.1) for integrated optical devices [15]. TeO_2 exhibits exceptional light transmission characteristics in the visible and infrared spectra, ranging between 0.4 to 7 μm, with low dispersion [16]. Low propagation losses ~ 0.1 dB/cm in the 1550 nm wavelength window have been demonstrated in tellurite-based thin films [17] and planar rib waveguide structures [18]. Tellurite glasses are also robust materials with good corrosion resistance and high thermal and mechanical stability [13] that can be deposited at low temperatures [18].

For active devices, TeO_2 has excellent rare-earth solubility [19], which pairs nicely with its wide optical transparency as TeO_2 can host different optically active materials

with various active transition ranges, including the second and third telecom windows near 1.3 μm and 1.53 μm, respectively, and beyond 2 μm, which will be crucial for future active integrated optics components and applications [18, 20]. This is accompanied by low quenching, large emission bandwidth and low phonon energies (600 – 800 cm^{-1}) that enable radiative transitions which are not possible in other oxide-based rare-earth hosts [16, 20]. The high index of TeO_2 also increases the stimulated emission cross section of rare-earth ions by a factor of $(n^2 + 2)/n$ for electron-dipole transitions [21]. TeO_2 also possesses a high nonlinear refractive index ($n_2 = 1.3 \times 10^{-18}$ m^2/W at 1900 nm) and exhibits optical nonlinear processes, such as Raman gain, more than any other oxide glass [18, 22].

TeO_2 has many advantages over SiO_2 and other cladding materials for silicon-based amplifiers. Light-matter interaction is increased as the high index of the TeO_2 delocalizes the mode from the silicon waveguide and attracts it to raise the mode overlap with the gain material. The index contrast between Si and TeO_2 is also less than that of silicon and other lower index claddings, which significantly reduces scattering losses, by approximately 40% in comparison to SiO_2 cladding with equal mode overlap, caused by light interactions at core-cladding interfaces [23, 24]. Finally, unlike purely tellurite waveguides [18, 25, 26], these devices do not require an additional etch step that may reduce device performance as the uniformity of the deposited TeO_2 film onto an already existing waveguide creates a ridge-like structure with deposition alone. Various active TeO_2 claddings have already been demonstrated on silicon nitride (Si_3N_4) waveguides, including an erbium-based device exhibiting 5 dB peak net gain and 1.7 dB/cm gain per unit length in the 1550 nm wavelength window [27], as well as a thulium-based device demonstrating 7.6 dB total gain and 1.1 dB/cm gain per unit length at 1870 nm wavelength, targeting applications in the 2 μm telecom band [28].

Though it is not yet developed for mass fabrication, **erbium-doped tellurium**

oxide (TeO_2:Er^{3+}) has received and continues to receive lots of research attention as an attractive material for active integrated optics and optoelectronics. In this thesis, we propose TeO_2:Er^{3+} as an active cladding material deposited onto SOI waveguides in hopes of recognizing a fully compatible and active EDWA light source integrated onto a SiP waveguide platform for integrated optics.

1.4 Thesis outline

Chapter 2 reviews the background and theory behind optical waveguides, explaining the phenomena that allow light to travel through the media we incorporate on these devices and the loss mechanisms which affect the behaviour and properties of light within them. Optical amplifier theory is also discussed, including the spectroscopy of rare-earth ions, particularly erbium, and the various energy transitions that enable amplification via optical processes. Equations for modelling optical amplifiers in a two-level energy system are detailed at the end of the chapter.

Chapter 3 describes the fabrication processes we utilize to manufacture our devices, including the SOI waveguide platform and our sputtering system for tellurium oxide thin film deposition. Following this, the design process of our waveguide amplifiers is stated with full details of the simulation steps and results, as well as the design mask layouts sent out for fabrication, provided. The amplifier model used to characterize the gain performance of our device finalizes the chapter.

Chapter 4 states the experimental results of our fabricated devices, including passive waveguide loss measurements and active gain measurements. Suggestions for improvement are given afterwards.

Chapter 5 concludes the thesis with a summary of significant results achieved here and provides insight into future projects that may be realized from this work. Skills

acquired by the primary researcher (me) are also listed. The Matlab code for the optical amplifier model is provided in Appendix A.

1.5 Internship

Multiple trips to the National Research Council of Canada (NRC Canada) in Ottawa, Ontario were made between the period of June 1, 2019 and March 21, 2020. The primary focus of this internship was on the design process for optical waveguide amplifiers like the ones presented in this thesis. Many resources, such as various simulation tools and access to relevant literature, as well as the expertise of senior research officers at NRC Canada were given, providing a fruitful learning experience. The techniques and knowledge gained during this time also provided insight into design considerations for more advanced waveguide structures, such as subwavelength gratings (SWGs). This experience has led to a stronger relationship between our groups at McMaster University and NRC Canada, and even outputted a publication in Optics Express [24]. A Ph.D. project building off the work presented in this thesis is also underway.

Chapter 2

Background & Theory

This chapter discusses the background and theory of the devices presented in this thesis. Insight on the principles of light, their behaviour in optical waveguides and the performance of optical waveguides is given first. Afterwards, details on the spectroscopy of rare-earth ions is given, which finally leads to the science behind all-optical amplification and methods of modelling active rare-earth-based integrated optical devices.

2.1 Waveguide theory

An electromagnetic wave that travels in air or through free space is unguided as it propagates through and diffracts across the bulk media. Applications that make use of electromagnetic waves require control over their direction and spatial coherence. This is accomplished by confining the wave within a medium or device called a **waveguide**, which provides a pathway for the wave to travel through.

Optical waveguides are specific to the field of optics and are used to guide light. The most common type of optical waveguide is the **optical fiber**, which uses a cylindrical structure composed of a silica core and cladding, each with a slightly different refractive index. In this thesis, we study and discuss silicon **wire waveguides** (sometimes better known as "channel" or "strip" waveguides) and the principles in which they operate.

In this section, we will discuss the phenomenon of total internal reflection, how it can be applied to various optical waveguide structures, and the characteristics and performance of light itself within such optical waveguide structures.

2.1.1 Total internal reflection

Consider the scenario in Figure 2.1. An electromagnetic wave travels through a dielectric medium with refractive index n_1 (medium 1) and strikes an interface between medium 1 and an adjacent dielectric medium with refractive index n_2 (medium 2) at an incident angle, θ_I, relative to the normal of the interface. Part of the incident wave is transmitted through the interface into medium 2, while the remainder is reflected through medium 1. The angles of the reflected and transmitted waves can be calculated using **Snell's Law of Refraction** [29]:

$$n_1 \sin\theta_R = n_2 \sin\theta_T, \tag{2.1}$$

where θ_R and θ_T are the reflected and transmitted angles, respectively. In the case where $n_1 > n_2$, it is possible to achieve an incident angle that allows $\theta_T > 90°$ in Eq. (2.1). While this is not physically possible, it implies that the energy dissipation/perturbation caused by interaction at the interface confines the wave strictly to medium 1. This is the phenomenon known as **total internal reflection** (TIR), and it is made possible when the incident angle is larger than the critical angle [29]:

$$\theta_I > \theta_C = \sin^{-1}(n_2/n_1). \tag{2.2}$$

These conditions allow equivalent intensities of the incident and reflected electromagnetic waves and form the basic operation of optical waveguides.

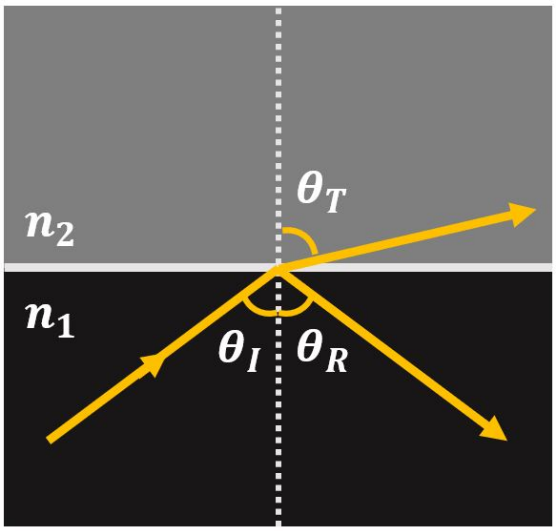

FIGURE 2.1: Snell's law of refraction.

2.1.2 Optical waveguides & modes

The simplest geometry of an optical waveguide is in the form of a **dielectric planar waveguide**, which is depicted in Figure 2.2. It consists of 3 layers (from bottom to top): a substrate layer, a film layer and a cladding layer, each with their own refractive indices, n_s, n_f and n_c, respectively. Using the explanation of TIR above, light may be confined and guided within the film layer if the materials are selected such that $n_f > n_c$ and $n_f > n_s$, and if the angles of the light incident on the cladding and substrate layers are greater than the following critical angles: $\theta_{C_1} = \sin^{-1}(n_c/n_f)$ and $\theta_{C_2} = \sin^{-1}(n_s/n_f)$, respectively. Figure 2.2 also includes a ray tracing diagram in the case that the above conditions are satisfied. If the conditions are not satisfied, some of the light will leak out of and no longer be fully confined to the film layer, resulting in either a radiation mode, in the case of leakage into the cladding layer, or a substrate mode, in the case of leakage into the substrate layer.

Based on the planar waveguide structure and coordinate system of Figure 2.2, a guided wave confined to the waveguide core will propagate through the waveguide in

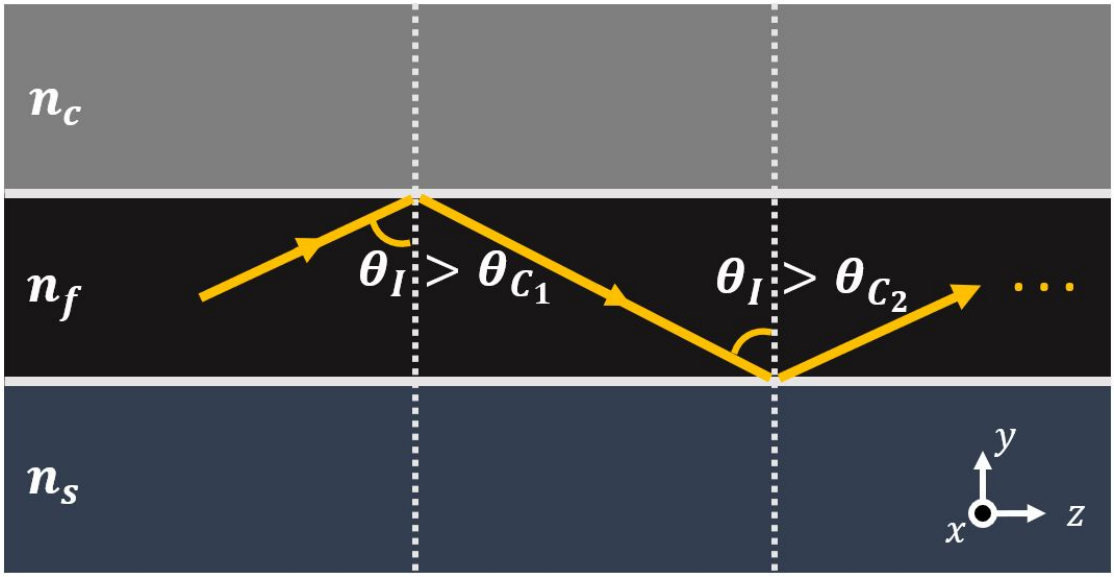

FIGURE 2.2: Total internal reflection in a dielectric planar waveguide.

the z direction. As this happens, a phase shift will occur every time the wave strikes an interface. The **wave vector**, $k = 2\pi/\lambda$, where λ is the wavelength, determines the direction of propagation of the wave and is used to quantify the phase change of the electromagnetic wave per unit length of propagation. The field patterns will interfere with each other either constructively or destructively depending on the phase difference between the two counter-propagating waves. If conditions for constructive interference are met, superposition of the two waves will occur, resulting in a standing wave field pattern of the guided modes in the y direction of the waveguide.

Optical modes are defined as the spatial distribution of optical energy in waveguides in one or more dimensions. Let us consider a mathematical definition of an electromagnetic field of a monochromatric wave of the form:

$$E(r,t) = E(r)e^{i\omega t}, \tag{2.3}$$

which is a solution to the Maxwell's self-supporting **wave equation** [30]:

$$\nabla^2 E(r,t) = \frac{n^2(r)}{c^2}\frac{\partial^2}{\partial t^2}E(r,t), \tag{2.4}$$

where $E(r,t)$ is the position- and time-dependent energy, $\omega = 2\pi\nu$ is the radian frequency of the wave, $n(r)$ is the refractive index of the waveguiding material (in this case, the dielectric film layer with refractive index n_f) and $c = 1/\sqrt{\varepsilon_0\mu_0}$ is the speed of light in vacuum, with ε_0 and μ_0 representing the electric permittivity and magnetic permeability in vacuum, respectively. Assuming complex notation of Eq. (2.3) and time independence of Eq. (2.4), we can express Eq. (2.4) as:

$$\nabla^2 E(r) + k^2 n^2(r) E(r) = 0, \tag{2.5}$$

where $k \equiv \omega/c$. The spatial dependence of the mode propagation can then be expanded to the three dimensions specified in the coordinate system of Figure 2.2. The intensity mode profile represents energy distribution at various cross sections along the waveguide structure. As the mode propagates along the z-axis, the intensity changes due to reasons that will be discussed in Section 2.1.4. We can express the energy as $E(r) = E(x,y)e^{-i\beta z}$, where $E(x,y)$ represents the energy profile at a given transverse cross section along the waveguide and β is the **propagation constant**. Assuming an infinite slab in the x-axis, Eq. (2.5) now becomes:

$$\frac{\partial^2 E(x,y)}{\partial t^2} + [k^2 n^2 - \beta^2]E(x,y) = 0. \tag{2.6}$$

Since β is just the z-component of the wave vector k, the propagation is only dependent on the $[k^2n^2 - \beta^2]$ term. It is important to note that both $E(x,y)$ and $\partial E(x,y)/\partial y$ must be continuous at the interface boundaries. Therefore, the only solutions to Eq. (2.6) are either sinusoidal or exponential.

FIGURE 2.3: Various guided mode intensity profiles in dielectric planar waveguide structure such that $kn_f > \beta > kn_{c,s}$.

Figure 2.3 displays a variety of behaviours that the intensity profile may exhibit such that $kn_f > \beta > kn_{c,s}$, or more generally, $kn_2 > \beta > kn_{1,3}$. Outside of the waveguide core, within the cladding and substrate regions, exponential behaviour dominates as light leaks out of the waveguide and disperses into the lower index cladding or substrate material regions. This exponentially decaying section of the intensity profile is generally referred to as the **evanescent tail**, and is largely responsible for the loss mechanisms that will be discussed in Section 2.1.4. Meanwhile, inside the waveguide core, the energy field is supported due to standing wave conditions as it exhibits sinusoidal behaviour along the y-axis. The modal behaviour supported in the planar waveguide is determined by the geometric parameters of the waveguide, primarily the waveguide core thickness h. Through decomposition of the wave vector, we can erect an equation for the phase matching condition under a standing wave configuration and determine the appropriate geometry required for each modal behaviour of interest. It is also helpful to note that the intensity profiles in Figure 2.3 are analogous to the wave functions derived in the infinite particle in a box problem commonly discussed in quantum mechanics.

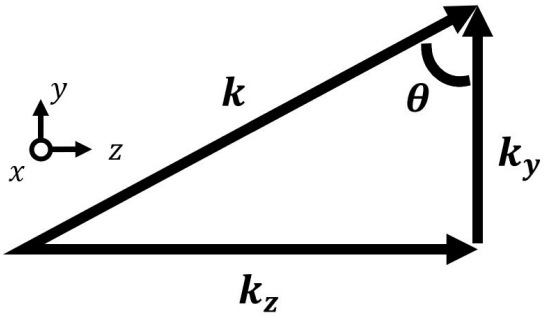

FIGURE 2.4: Wave vector decomposition diagram

Consider the wave vector k of the initial ray of the electromagnetic wave in Figure 2.2, which is replotted with respect to its components in Figure 2.4. θ corresponds to the angle of incidence in which the wave strikes the film-cladding interface in Figure 2.2. Because the wave is propagating through the film layer, we may define the wave vector as $k = k_0 n_f$, where $k_0 = 2\pi/\lambda_0$. Basic trigonometry can be applied to establish expressions for each wave vector component:

$$k_z = k \sin\theta = k_0 n_f \sin\theta, \tag{2.7a}$$

$$k_y = k \cos\theta = k_0 n_f \cos\theta. \tag{2.7b}$$

For guided modes confined to the film layer, k_y must be a standing wave. The phase shift that the wave encounters due to propagation is written as:

$$\Phi_p = 2hk_y = 2hk_0 n_f \cos\theta, \tag{2.8}$$

where h is the thickness of the film layer. The standing wave configuration is also accompanied by phase shifts due to alternating wave interactions at the film-cladding interface and film-substrate interface, which we will denote as Φ_c and Φ_s, respectively. The total phase change for a point on a wavefront that makes a round trip to the film-cladding interface, the film-substrate interface and back again, must be a multiple

of 2π to avoid optical energy decay and destructive interference. Thus, altogether, accounting for every phase shift term and assuming constructive interference conditions, the resulting **phase matching condition** is:

$$2\pi m = 2hk_0 n_f \cos\theta + 2\Phi_c + 2\Phi_s, \tag{2.9}$$

where m is the mode number and a positive integer. The $2\Phi_c$ and $2\Phi_s$ terms are called Goos-Hanchen shifts, which are interpreted as penetrations of zig-zag rays of a certain depth into the confining layers before reflection occurs [30]. We neglect these terms for this derivation and equate them to zero. The modes depicted in Figure 2.3 correspond to mode orders of $m = 0, 1, 2$, from left to right. Any positive integer value for m will satisfy the phase matching condition in Eq. (2.9) and characterize a guided mode. As the waveguide core thickness increases, so do the number of supported modes, or m values, that satisfy Eq. (2.9).

The devices discussed in this thesis are **single mode waveguides**, meaning they only support the fundamental, or zeroth order ($m = 0$), mode. To ensure a waveguide is single mode, we need to determine the waveguide core thickness at which the first order mode is supported and set the thickness below that threshold. Plugging in $m = 1$, as well as $2\Phi_c = 2\Phi_s = 0$, into Eq. (2.9), we obtain an equation for waveguide thickness in which only the fundamental and first order modes are supported:

$$h = \frac{\lambda}{2\pi n_f \cos\theta}, \tag{2.10}$$

where λ is the wavelength of light. Assuming a silicon-on-insulator (SOI) material configuration, the material index profiles of Figure 2.3 become $n_f \approx 3.5$ and $n_c = n_s \approx 1.45$. TIR in the silicon waveguide layer of an SOI configuration is ensured as long as the angle of incidence θ is greater than the critical angle $\theta_c = \sin^{-1}(1.45/3.5) \approx 24.48°$. If we plug $\theta = \theta_c$ into Eq. (2.10), the calculated waveguide core thickness is $\sim$ 243 nm for 1550

nm wavelength light. Therefore, waveguides with a core thickness $h < 243$ nm will not support the first order mode and will be single mode along the y axis, similar to the leftmost mode depicted in Figure 2.3. Many SOI foundries implement a 220 nm silicon slab thickness for this reason [12].

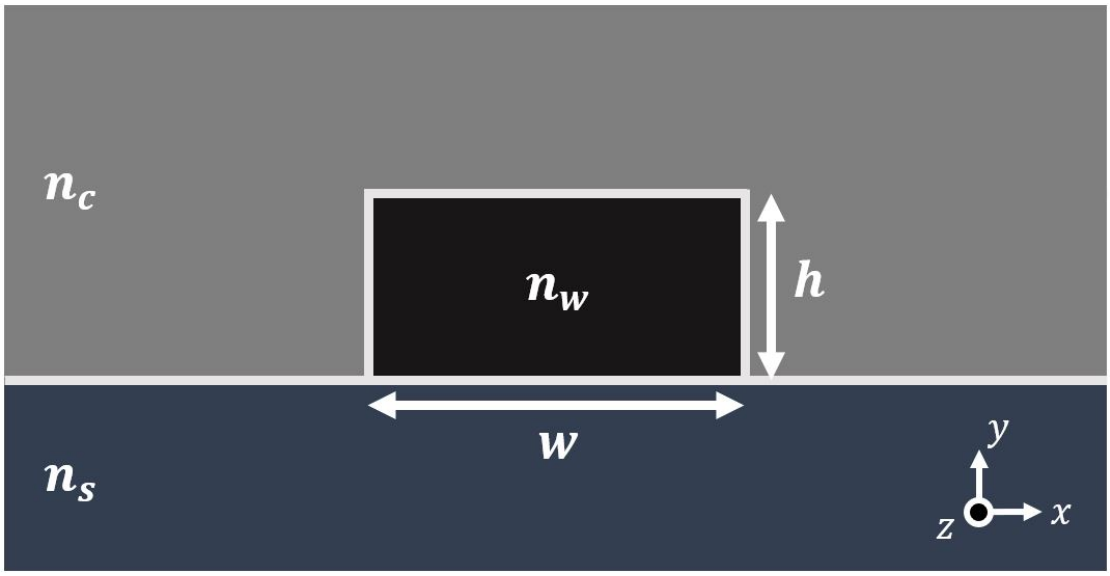

FIGURE 2.5: Channel waveguide structure with refractive index n_w, width w and thickness h.

Channel waveguides are like planar waveguides but with geometrical and modal restrictions in both the x and y axes. The type of channel waveguides investigated in this thesis are depicted in Figure 2.5. The waveguide with refractive index n_w, width w and thickness h sits atop a substrate with refractive index n_s like in the configuration depicted in Figure 2.2. However, the waveguide now has boundaries in the x direction and is surrounded on all other sides by the cladding material with refractive index n_c. While planar waveguides offer confinement in one dimension, channel waveguides are beneficial by confining light in two dimensions. The calculations carried out above can be modified to find a suitable waveguide width w in which only the fundamental waveguide mode is supported in the x direction. Solving modes in 2-D rectangular waveguides is essential and can be done analytically using approaches such as Marcatili's method

[31]. In this thesis, we perform mode calculations in Section 3.2.1 using Synopsis RSoft [32], a simulation software suite with tools that allow us to design and characterize various photonic devices. Once single mode conditions are established in both the x and y directions, the waveguide dimensions are small enough ($< 0.5\ \mu m^2$) to allow tight confinement within the waveguide core and propagation of the electromagnetic field along the length of the waveguide in the z direction. From a footprint perspective, this makes optical waveguides much more advantageous over optical fibers. However, dimensions too small may result in higher optical losses. Reasons for this will be discussed in the coming sections.

2.1.3 Chromatic dispersion

Chromatic dispersion is described as the dependence of an electromagnetic wave's frequency on its wave vector. Different types of dispersion are encountered as an electromagnetic wave travels through a waveguide. The two most common are material dispersion and waveguide dispersion.

Let us consider an electromagnetic wave traveling through vacuum. The speed of this wave ν is equal to $c \equiv 3 \times 10^8 m/s$, or the speed of light. This is because vacuum does not influence the speed of the wave relative to the speed of light. The **refractive index** of a medium is defined as the ratio of these two values: $n = c/\nu$. For the case of vacuum, as well as air, $n = 1$, so ν is unaffected. However, if the wave travels through any other medium, which usually have a refractive index greater than 1 ($n > 1$), the velocity of the wave in that material will be less than c due to this relation. This forms the basis of **material dispersion**.

Assuming this wave is linearly polarized in the $+x$-direction and propagates in the $+z$-direction, its electric field may be described as follows:

$$E_x(z,t) = E_x e^{-i(kz-\omega t)}, \tag{2.11}$$

where k is the wave vector and ω is the angular frequency of the wave. In a dispersive, non-magnetic material, the wave vector may be expressed in terms of its real and imaginary parts such that: $k = \beta + i\frac{\alpha}{2}$ [33]. Plugging this into Eq. (2.11) outputs:

$$E_x(z,t) = E_x e^{-i(\beta z - \omega t)} e^{-\frac{\alpha z}{2}}. \tag{2.12}$$

The exponential term containing α in Eq. (2.12) describes a decaying exponential function that represents the rate at which the intensity of the electromagnetic wave decays, while the exponential term containing β represents the function of a propagating plane wave. Given these definitions, α and β are considered the **attenuation coefficient** and propagation constant, respectively, and both are dependent on the material in which the electromagnetic wave is propagating. The propagation constant can easily be calculated for a non-absorptive material ($\alpha = 0$). In such a case, $k = \beta$. Using the modified version of the wave equation from Eq. (2.4), as well as other relations already mentioned, such as $n = c/\nu$, $k = \omega/c$ and $\omega = 2\pi c/\lambda$, we find that:

$$\beta = \frac{2\pi n}{\lambda}. \tag{2.13}$$

Furthermore, we develop a simplified equation for the angular frequency of the wave that is dependent on its wave vector. This is known as the **dispersion relation** [34]:

$$\omega = \frac{ck}{n}. \tag{2.14}$$

The refractive index of a material may also be expressed as $n = \sqrt{\varepsilon_r \mu_r}$, where ε_r and μ_r are the electric permittivity and magnetic permeability of the material, respectively. It may or may not be dependent on the wavelength or wave vector ($n = n(\lambda)$). If not, the dispersion relation in Eq. (2.14) is linear and implies that every frequency of light will travel through the material at a constant velocity, such as in free space or vacuum, where $n = 1$ and $\nu = c$ for all wavelengths. On the other hand, if the refractive index

is wavelength-dependent, the dispersion relation is non-linear, and this implies that electromagnetic waves of different frequencies will propagate with different velocities. A material is considered **dispersive** if it has a wavelength-dependent refractive index.

When we introduce the topic of dispersion to a waveguide structure, we must first consider the non-uniformity of materials. In the simplest case, we have a planar waveguide structure described in Figure 2.2 with refractive indices such that $n_f > n_c \geq n_s$. The propagation constant of an electromagnetic wave travelling through the waveguide is dependent on all material properties within the waveguide as well as the mode profiles which are supported by the waveguide and is defined as:

$$\beta = \frac{2\pi n_{eff}}{\lambda}, \tag{2.15}$$

where n_{eff} is the **effective (refractive) index**, which replaces the n term in Eq. (2.13). Effective refractive index describes the rate at which the speed of light is reduced not only by the material, but also by the interactions between the light and the various dielectric interfaces that are dependent on the geometric properties of waveguide. This is the foundation of **waveguide dispersion**. We calculate the effective refractive indices of our devices using computational software, such as RSoft, and provide details of these calculations in Section 3.2.1.

2.1.4 Waveguide loss mechanisms

Though optical waveguides provide many benefits over both electrical copper wires and optical fibers, their major drawback arises from high loss. Optical fibers exhibit propagation loss on the scale of dB/km, whereas waveguides suffer from losses on the scale of dB/cm. Much of the research behind optical waveguides focuses on how to minimize losses and optimize the performance. To do this, an analysis of the different waveguide loss mechanisms must first be considered.

The Lambert-Beer law for the change in light intensity I at wavelength λ propagating through an infinitesimal waveguide length Δz states that:

$$\frac{dI(z)}{dz} = -a(\lambda)I, \tag{2.16a}$$

$$I(z + \Delta z, \lambda) = I(z, \lambda) \cdot \exp[-a(\lambda)\Delta z], \tag{2.16b}$$

where $a(\lambda)$ is the wavelength-dependent **absorption coefficient** (cm^{-1}). This coefficient can be expressed in dB/cm and rewritten as:

$$\alpha(\lambda) = 10 \log_{10}(e) \cdot a(\lambda), \tag{2.17}$$

which we will use throughout this thesis. The total absorption coefficient or background loss is defined as the sum of all relevant loss mechanisms in optical waveguides:

$$\alpha_{Total}(\lambda) = \alpha_{pas}(\lambda) + \alpha_{act}(\lambda), \tag{2.18}$$

where $\alpha_{pas}(\lambda)$ and $\alpha_{act}(\lambda)$ are the background losses due to passive and active processes, respectively. $\alpha_{act}(\lambda)$ only applies to optical amplifiers doped with excitation material, such as our waveguide amplifiers, and will be described later in Section 2.2.3.

TABLE 2.1: Correlation of index contrast and waveguide loss in various waveguides, primarily due to interface induced scattering.

Waveguide Type	Optical fibers	SOI waveguides
Index Contrast (Δn)	~0.01	~2
Scattering Loss Factor [23]	17.4	206.0
Loss Units	dB/km	dB/cm

On the other hand, passive waveguide loss mechanisms apply to any type of optical waveguide and come in many forms. The prime suspect contributing to $\alpha_{pas}(\lambda)$ is interface induced scattering. When light interacts at an interface between two media of

varying refractive index, scattering naturally occurs and may cause light to unintentionally radiate out of and away from the waveguide, thus deterring the optical intensity of the confined mode. Interface induced scattering loss increases with index contrast between the two media, particularly by a factor of $(n_1^2 - n_2^2)^2$ [23]. This provides an excellent explanation of the difference in unit loss magnitude between silica-based optical fibers and SOI waveguides, which is summarized in Table 2.1. Furthermore, scattering loss is amplified with surface roughness, which can be quantified and correlated based on the Payne-Lacey model [35]. This is much harder to manage and control on nanoscale optical waveguides in comparison to micron-thick optical fibers. It also has a much larger effect on the very tightly confined modes of optical waveguides and is dependent on the quality of the fabrication process.

Material-dependent background loss also contributes to $\alpha_{pas}(\lambda)$ and is primarily caused by the absorption characteristics of the material. However, because the materials we use for our devices (silicon and tellurium oxide) both exhibit low loss and low dispersion at our 1550 nm target wavelength, loss from this source will be relavtively low and insignificant compared to loss from scattering. Other waveguide loss mechanisms include scattering from volumetric refractive index inhomogeneity and coupling of guided modes to substrate modes [36]. However, these losses are also considered negligible for our devices.

2.2 Optical amplifier theory

In this section, we discuss the spectroscopy of rare-earth ions, including the types of energy transitions that occur within them and the parameters that affect these transitions. Specific study is given to those of erbium, and equations describing how light behaves within a rare-earth-based optical amplifier are stated and explained. These equations will be used in our amplifier model described later in Section 3.2.2.

2.2.1 Spectroscopy of rare-earth ions

Rare earth elements, scientifically referred to as lanthanides, have a special atomic structure given in the atomic form (Xe)$4f^{N'}6s^2$ or (Xe)$4f^{N'-1}5d6s^2$, where (Xe) represents the Xenon core. For most rare earths, such as erbium, the partially filled 4f shell contracts and becomes bound within the 5s and 5p subshells. This provides shielding for the 4f shell and allows the transitions to occur independent of the host material [37].

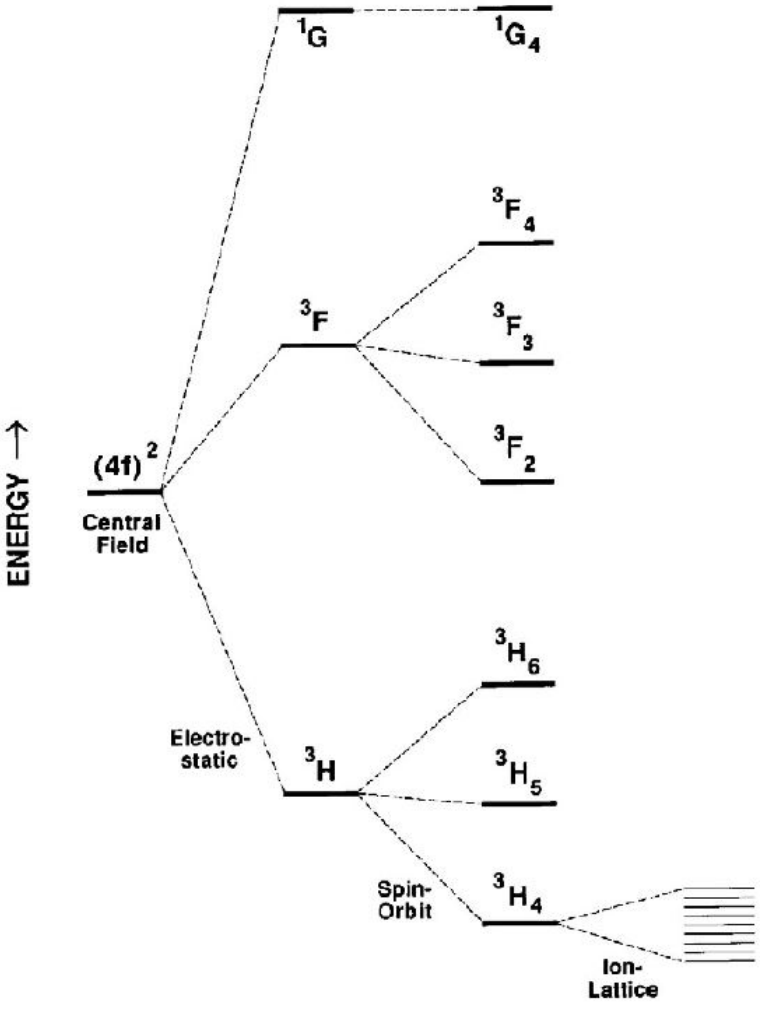

FIGURE 2.6: $4f^N$ energy diagram illustrating hierarchy of splittings resulting from electron-electron and electron-host interactions [38].

The $4f^N$ configuration is composed of multiple states in which the 4f electron may

be excited prior to excitation with outer shells of the ion, such as 5d and 5g. The degeneracies of the energy levels are lifted due to various atomic interactions between the 4f electrons. A set of quantum numbers describes the different levels of the energy system and are labelled using Russell-Saunders notation in the form $^{2S+1}L_J$, where 2S+1 represents the spin angular momentum, L represents the orbital angular momentum and J represents the total angular momentum. Electrostatic interactions lift the angular degeneracy and produce a spectrum of states in which the energies only depend on L and S. Spin-orbit coupling, the strongest magnetic interaction, causes further energy level splitting of the LS coupling states, lifting the total angular momentum degeneracy into separate J levels [38]. An illustration of these splittings is given in Figure 2.6. For erbium, the ground state is represented as $^4I_{15/2}$, which equates the quantum numbers to S = 3/2, L = 6 and J = 15/2.

Rare-earth ions may be embedded in glass hosts in a trivalent state (i.e. Ln^{3+}), which is the most stable. In this scenario, further splitting of the rare-earth energy levels in the 4f shell occurs due to the ion-lattice interactions caused by the crystal field of the host. This additional splitting that the orbitals undergo is called **Stark splitting** and results in different Stark components of the parent manifolds. Optical transitions that occur in rare earth ions between the various 4f states manifest as weak and narrow bands that are dominated by the Stark splitting [39]. These sharp line shapes result in efficient emission that is useful for applications such as lasing [38], which is why we are interested in exploring amplification in rare-earth doped devices.

Erbium (Er^{3+}) is a rare earth element that is used abundantly in telecommunications due to its emission properties in the low loss and low dispersion C-band and its notoriety in the success of the erbium-doped fiber amplifier (EDFA) [40]. The energy diagram of Er^{3+} is displayed in Figure 2.7. The energy difference between the ground state ($^4I_{15/2}$) and the first excited energy state ($^4I_{13/2}$) corresponds to a transition around a

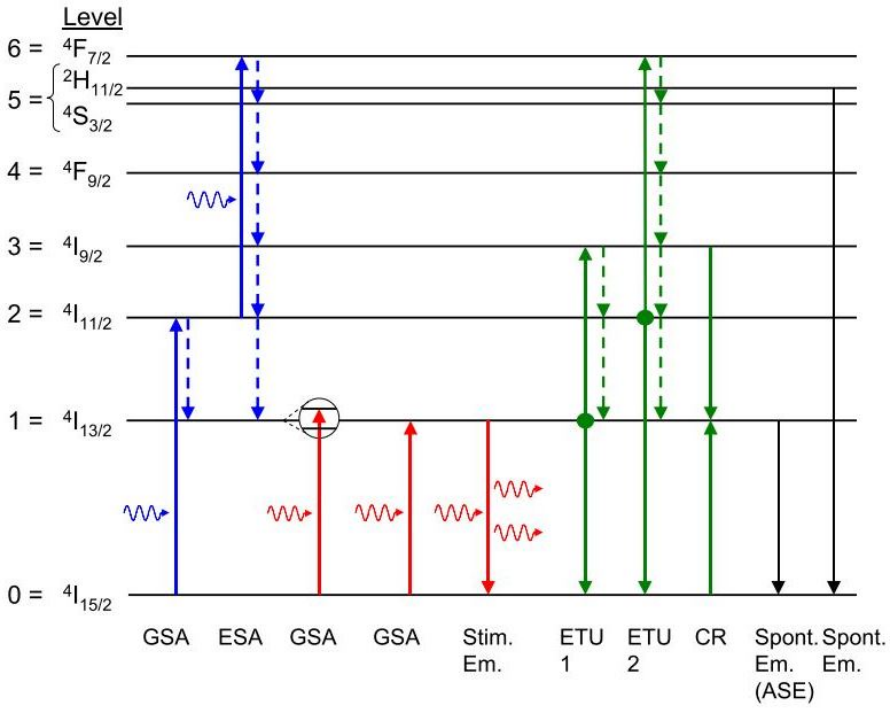

FIGURE 2.7: Schematic diagram of energy levels and transitions relevant to Er^{3+}-based amplifier operation. Adapted from [41].

1530 nm wavelength, which can be used to excite the 1550 nm wavelength commonly used in telecommunications applications. Er^{3+} has several absorption lines as depicted by the peaks in the absorption spectra in Figure 2.8. These spectra apply to Er^{3+}-doped tellurite glass, which we implement on the devices discussed in this thesis. The absorption lines become broadened due to the amorphous nature of the tellurite host material. Because we plan to incorporate erbium-doped tellurite glass onto a silicon waveguide for our amplifiers, we cannot utilize light sources below 1.1 μm due to the absorption spectrum of silicon. Thus, we implement a 1477 nm laser pump source to optically excite Er^{3+} ions in our devices.

2.2.2 Energy transitions and cross sections

Rare-earth-based optical amplifiers operate through the process of ion energy transitions within the 4f shell. The transitions are usually the result of ion interaction with

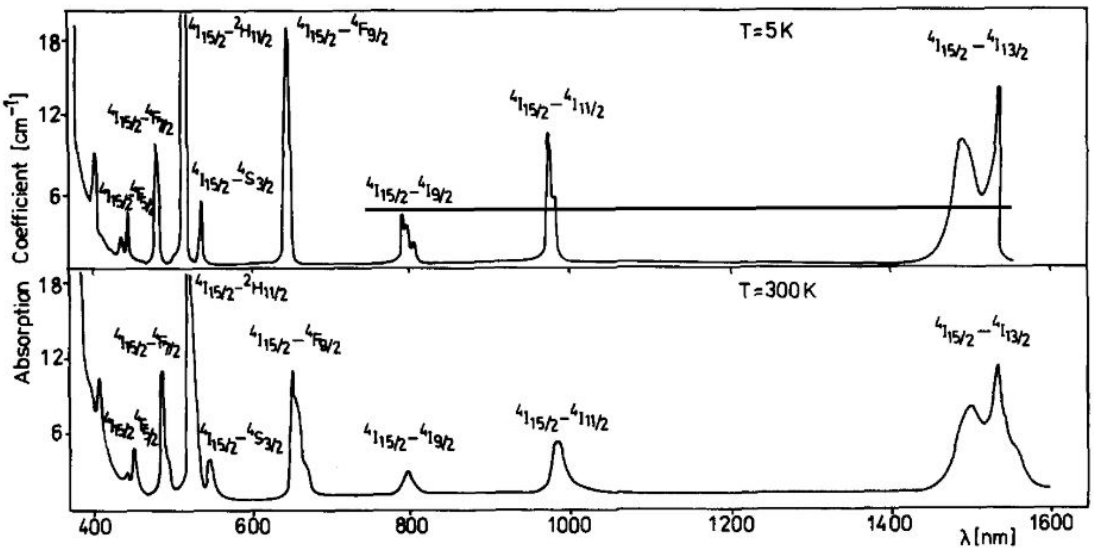

FIGURE 2.8: Absorption spectrum of Er^{3+}-doped tellurite glass recorded at 5K and 300K temperature. Erbium concentration = 1.2×10^{21} ions/cm^3 [42].

an external stimulus, such as a photon. The most general transitions that occur from this interaction are excitation of the ion to a higher energy state by absorbing the incident photon (**stimulated absorption**) or an already excited ion emitting a photon of equal phase and frequency to the incident photon (**stimulated emission**). There is also the possibility that an excited ion will fall back down to the ground state and emit a photon of random phase and direction without external stimulus (**spontaneous emission**). These three transitions are depicted in Figure 2.9. An unperturbed rare-earth energy system in thermal equilibrium contains little to no excited states that are necessary for radiative recombination via emission. External stimuli are typically provided, or pumped, optically into the system using an external laser source with a specific wavelength to induce stimulated absorption and excite the relaxed ions. Spontaneous emission is more likely to occur over stimulated emission unless if significant pumping is continuously applied and maintained. Once stimulated emission dominates, most of the excited energy states are filled with ions and ground states are filled with holes. This condition is known as **population inversion** and is essential for enabling gain within

an amplifier.

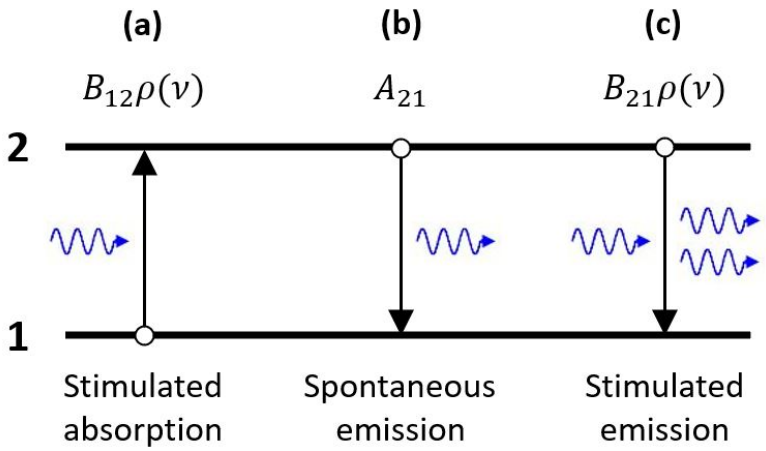

FIGURE 2.9: Visualization and associated transition rates of (a) stimulated absorption, (b) spontaneous emission and (c) stimulated emission of photons in a nondegenerate two-level energy system.

The transition (**absorption** and **emission**) **cross sections**, $\sigma^{(a)}$ and $\sigma^{(e)}$, are defined as the probabilities in which stimulated absorption or emission can occur between two energy states of an ion, respectively. The amount of absorbed or emitted optical power is equal to the product of the associated cross section of the ion and the incident optical intensity:

$$P_{a/e}(\lambda) = \sigma^{(a/e)}(\lambda) I(\lambda), \tag{2.19}$$

where $P_{a/e}(\lambda)$ is the absorbed or emitted optical power and $I(\lambda)$ is the optical intensity. The fundamental concept of cross sections is derived from the Einstein relations that describe absorption and emission of light in a nondegenerate two-level system, like the one in Figure 2.9, based on quantum mechanical principles. Strongly coupled sub-levels are assumed with equal occupation and transition strengths between them, resulting in equal absorption and emission cross sections ($\sigma^{(a)} = \sigma^{(e)}$). The change in population of the first excited state, i.e. level 2, due to absorption and emission processes is defined

as:

$$\left(\frac{dN_2}{dt}\right)_{abs} = B_{12}\rho(\nu)N_1, \tag{2.20a}$$

$$\left(\frac{dN_2}{dt}\right)_{em} = -(A_{21} + B_{21}\rho(\nu))N_2, \tag{2.20b}$$

where N_1 and N_2 are the populations of the lower and upper states, respectively, $\rho(\nu)$ is the photon flux density (number of photons per unit frequency bandwidth per unit volume) and B_{12}, A_{21} and B_{21} are the Einstein coefficients that describe the strength of the stimulated absorption, spontaneous emission and stimulated emission transition rates, respectively. For the case of rare-earth ions, these two states are made up of a comb of Stark-split sub-levels that are populated to various extents based on the thermal distribution. Degeneracies g_1 and g_2 are introduced and indicate the total number of Stark sub-levels for the lower and upper state manifolds, respectively. The change in population can then be described by the sum of the rates of the various transitions, particularly for stimulated absorption and emission:

$$\left(\frac{dN_2}{dt}\right)_{abs} = \sum_{i,j=0}^{g_1,g_2} R(m_{1,i}, m_{2,j})N_{m_{1,i}}, \tag{2.21a}$$

$$\left(\frac{dN_2}{dt}\right)_{em} = \sum_{i,j=0}^{g_1,g_2} [A(m_{1,i}, m_{2,j}) + R(m_{1,i}, m_{2,j})]N_{m_{2,j}}, \tag{2.21b}$$

where $m_{1,i}$ and $m_{2,j}$ represent the sub-levels in the lower and upper states, respectively, and $A(m_{1,i}, m_{2,j})$ and $R(m_{1,i}, m_{2,j})$ are the spontaneous and stimulated transition rates, respectively. Further assumptions of certain lineshape functions and equal population in the sub-levels such that $N_{m_i} = N_i/g_i$, where $i = 1, 2$ represents the level number label from Figure 2.9, allow a relationship to be derived between the **radiative lifetime** and the transition cross sections known as the **Füchtbauer-Ladenburg** equation [43]:

$$\frac{1}{\tau_{21}} = A_{21} = \frac{8\pi}{\lambda^2}\int \sigma^{(e)}(\nu)d\nu = \frac{8\pi}{\lambda^2}\frac{g_1}{g_2}\int \sigma^{(a)}(\nu)d\nu. \tag{2.22}$$

However, the assumption of equally populated sub-levels and neglection of thermal Boltzmann statistics poses an issue with Eq. (2.22) as the calculated transition cross section values do not agree well with experimental results for erbium-doped fibers.

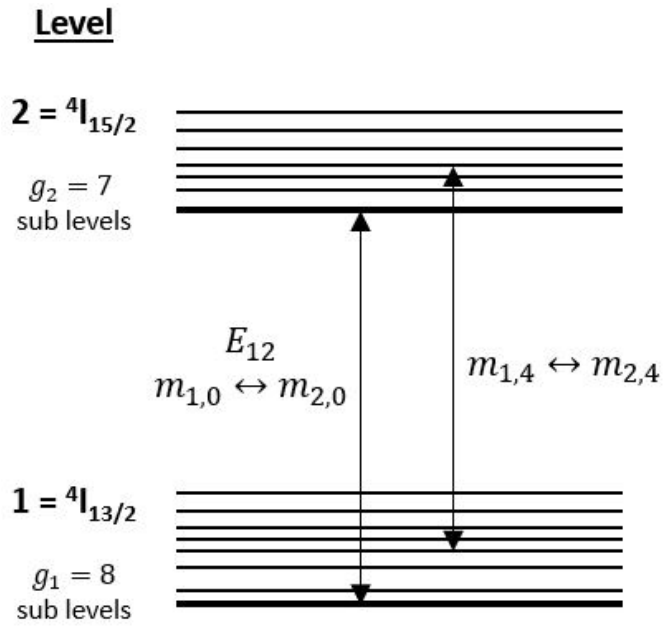

FIGURE 2.10: Two-level energy structure for Er^{3+} ion with Stark-split multiplets. Degeneracies have been lifted by an external field, resulting in, for the case of Er^{3+}, 8 sublevels in the $^4I_{15/2}$ state and 7 sublevels in the $^4I_{13/2}$ state.

A more accurate description of the cross sections was given by McCumber [44], who considered the thermal Boltzmann distribution that cause various extents of the population characteristics in Stark sublevels. In the case of the Er^{3+} ion, the spread of the sublevels for the lower levels of the erbium ion, $^4I_{15/2}$ and $^4I_{13/2}$ with respective degeneracies $g_1 = 8$ and $g_2 = 7$ (300 – 400 cm^{-1}), is larger than the average thermal energy kT (200 cm^{-1}). Thus, we expect significant differences among thermal populations of different sublevels and depart from the Füchtbauer-Ladenburg case in Eq. (2.22). Under the condition that thermal equilibrium is reached within a multistate manifold in a time shorter than the radiative lifetime of the manifold, the absorption and emission cross

section can be related such that:

$$\sigma^{(e)}(\lambda) = \sigma^{(a)}(\lambda) \cdot \frac{Z_1}{Z_2} \cdot \exp\left(\frac{E_{12} - h\nu}{kT}\right). \tag{2.23}$$

where Z_1/Z_2 is a ratio of energy partition functions based on Stark splitting and thermal distribution of the ground and excited states, respectively, E_{12} is the energy separation between the lowest-lying states of each multiplet, as depicted in Figure 2.10, h is Planck's constant, ν is the frequency corresponding to the transition energy, k is Boltzmann's constant, and T is the temperature. Replacement of the partition functions generalizes Eq. (2.23) and expresses it in the form (2.24):

$$\sigma^{(e)}(\lambda) = \sigma^{(a)}(\lambda) \cdot \exp\left(\frac{\epsilon - h\nu}{kT}\right). \tag{2.24}$$

where ϵ is the mean transition energy between the manifolds. The McCumber theory was re-introduced in the context of Er^{3+}-doped glasses by Miniscalco and Quimby [45], who provide an accurate solution to the value of ϵ. By this mannerism, the cross sections are only equal at a crossing frequency $\nu_c \equiv \epsilon/h$ and exhibit condition statements such that if $\nu < \nu_c$, then $\sigma^{(a)}(\lambda) < \sigma^{(e)}(\lambda)$, and vice versa for $\nu > \nu_c$. We use Eq. (2.24) later for our amplifier model, which is described in Section 3.2.2.

2.2.3 Amplification in an erbium-based two-level energy system

The above analysis of cross sections can be used for modelling gain in an erbium-doped fiber/waveguide amplifier (EDFA/EDWA). The amplifier response is based on rate equations that consider transition properties of the ions as they interact with various external stimuli and how the atomic population changes with respect to time. Furthermore, light flux propagation equations are reviewed as photon quanta travel through the amplifying medium over a given length. The following equations are applied later to our amplifier model in Section 3.2.2.

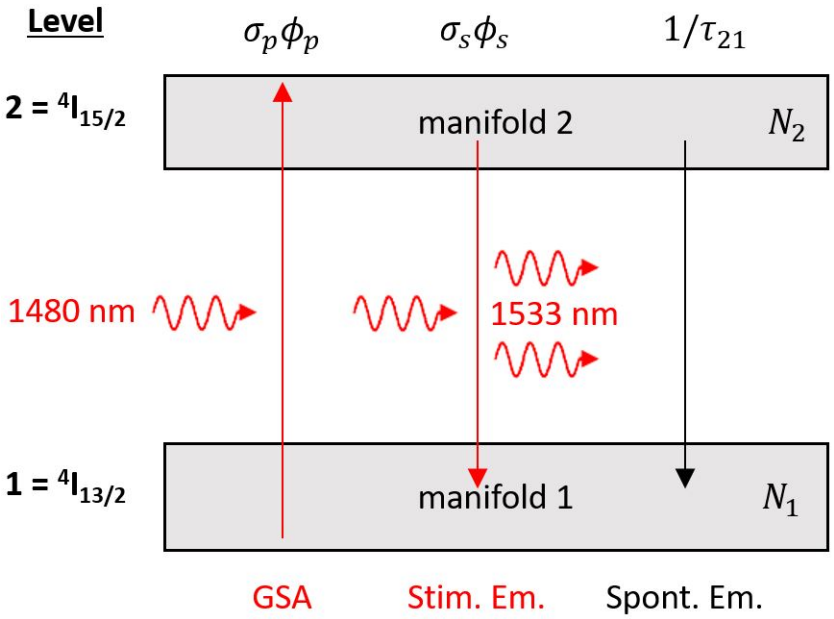

FIGURE 2.11: Simplified two-level energy diagram for Er^{3+} labelling transitions and corresponding terms relevant for the 1480 nm pumped TeO_2:Er^{3+} amplifier.

The two-level energy system of Er^{3+} with inhomogeneously broadened Stark manifolds depicted in Figure 2.10 is revised, generalized with transition relations relevant to our system and shown in Figure 2.11. We only consider the $^4I_{15/2}$ ground state and $^4I_{13/2}$ first excited state in this model as our experimental setup utilizes a 1477 nm pump source and 1550 nm tunable signal source that enable transitions between these two energy levels only. Spontaneous emission is not considered in these equations.

We consider a one-dimensional case in which light propagates in the z direction along the length of the amplifier. The light field intensities are derived from the light field powers such that:

$$I(z) = \frac{P(z) \cdot \Gamma}{A_{eff}}, \tag{2.25}$$

where Γ is the normalized mode overlap factor representing a ratio between the light field intensity that overlaps with the active region containing the Er^{3+} ions and the overall light field intensity, and A_{eff} is the effective cross-sectional area of the distribution of

erbium ions. Two light fields denoted as the pump and signal with intensities I_p and I_s, respectively, travel through the waveguide and interact with the ions. Their photon fluxes are described as:

$$\phi_{p/s} = \frac{I_{p/s}(z)}{h\nu_{p/s}} = \frac{I_{p/s}(z)\lambda_{p/s}}{hc}, \tag{2.26}$$

where $\lambda_{p/s}$ is the wavelength of the pump/signal source. From the McCumber-Miniscalco -Quimby Theory discussed in Section 2.2.2, the absorption and emission cross sections in a two-level energy system will be unequal at all but one wavelength described by the mean transition energy ϵ [45]. From here on, the notation we apply to the cross sections is $\sigma_{p/s}^{(a/e)}$, where the subscript denotes wavelength (pump or signal) and the superscript denotes the transition type (absorption or emission).

The **rate equations** describe how the populations of the lower and upper energy levels, N_1 and N_2, respectively, change with respect to time. Given all the transitions listed in Figure 2.11, the rate equations for this two-level model are:

$$\frac{dN_2}{dt} = -N_2/\tau_{21} + N_1\sigma_s^{(a)}\phi_s - N_2\sigma_s^{(e)}\phi_s - N_2\sigma_p^{(e)}\phi_p + N_1\sigma_p^{(a)}\phi_p, \tag{2.27a}$$

$$\frac{dN_1}{dt} = N_2/\tau_{21} + N_2\sigma_s^{(e)}\phi_s - N_1\sigma_s^{(a)}\phi_s - N_1\sigma_p^{(a)}\phi_p + N_2\sigma_p^{(e)}\phi_p = -\frac{dN_2}{dt}, \tag{2.27b}$$

where τ_{21} is the upper state ($^4I_{13/2}$) radiative lifetime. Because there are only the two energy levels, the assumption is that the total Er^{3+} concentration in the system is the sum of the populations at the two energy levels:

$$N = N_1 + N_2. \tag{2.28}$$

This is further supported by the sign opposition between Eq. (2.27a) and Eq. (2.27b). Under steady state conditions, the time derivatives are all equated to zero:

$$\frac{dN_1}{dt} = -\frac{dN_2}{dt} = 0. \tag{2.29}$$

This represents a divergence of the change in population with respect to time, signifying constant population densities in each level after a given amount of time in which the pump and signal fields are continuously applied upon the system. When we apply the steady state conditions of Eq. (2.28) and Eq. (2.29) to Eq. (2.27a) and Eq. (2.27b), we can derive a time-independent equation that determines the upper state population at a given position along the amplifier:

$$N_2(z) = \frac{\tau\sigma_s^{(a)}\phi_s(z) + \tau\sigma_p^{(a)}\phi_p(z)}{1 + \tau(\sigma_s^{(a)} + \sigma_s^{(e)})\phi_s(z) + \tau(\sigma_p^{(a)} + \sigma_p^{(e)})\phi_p(z)}N, \tag{2.30}$$

where $\tau = \tau_{21}$ from Eq. (2.27) and $\phi_{p/s}(z)$ are calculated using Eq. (2.26). Subsequently, N_1 can be calculated by substituting the result of Eq. (2.30) into Eq. (2.28).

The **propagation equations** describe the change in light field intensity of a given source as the beam travels down the length of the amplifier. For this system, we evaluate the propagation equations as:

$$\frac{dI_{p/s}(z)}{dz} = \left(N_2\sigma_{p/s}^{(e)} - N_1\sigma_{p/s}^{(a)}\right) I_{p/s}(z). \tag{2.31}$$

From Eq. (2.28), population inversion is defined as $N_2 > N_1$, or $N_2/N > 0.5$, and is necessary in order to achieve positive gain from the signal propagation equation. This is done only if the pump intensity is greater than the threshold pump intensity corresponding to signal gain at the signal wavelength ($dI_s/dz > 0$):

$$I_p \geq I_{th,p} = \frac{h\nu_p}{\tau_{21}} \frac{1}{\sigma_p^{(a)}\left(\sigma_s^{(e)}/\sigma_s^{(a)}\right) - \sigma_p^{(e)}}, \tag{2.32}$$

Integration of Eq. (2.31) and application of Lambert-Beer law similar to that discussed in Section 2.1.4 results in a simplified form of the propagation equations:

$$I_{p/s}(z + \Delta z) = I_{p/s}(z) \cdot \exp\left(\left(N_2\sigma_{p/s}^{(e)} - N_1\sigma_{p/s}^{(a)} - a_{p/s}\right)\Delta z\right), \tag{2.33}$$

where $a_{p/s}$ is the pump/signal absorption coefficient (cm^{-1}) that characterizes the overall background absorption loss of the material. This absorption coefficient is equivalent to $\alpha_{Total}(\lambda)$ from Eq. (2.18) for the pump and signal wavelengths, respectively, apart from the unit conversion expressed in Eq. (2.17), and is usually determined experimentally. In this case, $\alpha_{act}(\lambda)$ can be expressed as $\alpha_{Er}(\lambda)$ to describe absorption loss due to Er^{3+} ions in the doped waveguide, which equates to:

$$\alpha_{Er}(\lambda) = \sigma^{(a)}(\lambda) \cdot N \cdot \Gamma(\lambda) \cdot 10 \log e, \tag{2.34}$$

where $\Gamma(\lambda)$ is the calculated confinement factor within the active TeO_2:Er^{3+} layer, and N is the ground state population density. We only consider absorption loss due to passive processes in our model for now ($a_{p/s} = a_{pas}(\lambda)$).

After the above rate equations and propagation equations are calculated, the optical performance can be determined using the **internal gain** (dB):

$$g(\lambda) = 10 \log_{10}[I(z = L, \lambda)/I(z = 0, \lambda)], \tag{2.35}$$

the **total internal net gain** (dB):

$$G(\lambda) = g(\lambda) - \alpha_{Total}(\lambda), \tag{2.36}$$

and **internal net gain per unit length** (dB/cm):

$$\gamma(\lambda) = \frac{G(\lambda)}{L}, \tag{2.37}$$

where $I(z = 0, \lambda)$ and $I(z = L, \lambda)$ are the measured intensities of the signal light at the input and output waveguide facets, respectively, $\alpha_{Total}(\lambda)$ is the total absorption coefficient or background loss calculated using Eq. (2.18) and L is the amplifier length.

These equations (2.35 - 2.37) provide figures of merit that will allow us to compare to other amplifier devices in literature and characterize the true optical performance of our EDWA devices. Further details will be provided in Section 3.2.2 for simulation of the proposed device using our amplifier model and Chapter 4 for the experimental results.

Chapter 3

Fabrication & Design

3.1 Fabrication

3.1.1 Silicon-on-insulator platforms

Our devices were fabricated on 200 mm multi-project wafer (MPW) runs on a silicon-on-insulator (SOI) platform via both **Advanced Micro Foundry** (AMF) in Singapore [46] and **Applied Nanotools** (ANT) in Edmonton, Alberta, Canada [47]. Typical SOI wafers include (from bottom to top) a silicon substrate handle, a thermal buried oxide (BOX) layer, a crystalline silicon waveguide layer and an optional top cladding oxide layer which is typically deposited via plasma enhanced chemical vapour deposition (PECVD), as shown in the schematic in Figure 3.1. Our work primarily utilizes the samples that do not receive top oxide cladding as we deposit our own films directly onto the exposed waveguides. Table 3.1 describes the thicknesses of each layer on the silicon photonics platforms offered by AMF and ANT used for our two respective designs.

TABLE 3.1: Layer thicknesses of the SOI platforms from AMF and ANT

Layer thickness (μm)	AMF	ANT
Top cladding oxide[1]	3	2.2
Silicon waveguide	0.22	0.22
Buried oxide (BOX)	2	2
Silicon substrate	750	675

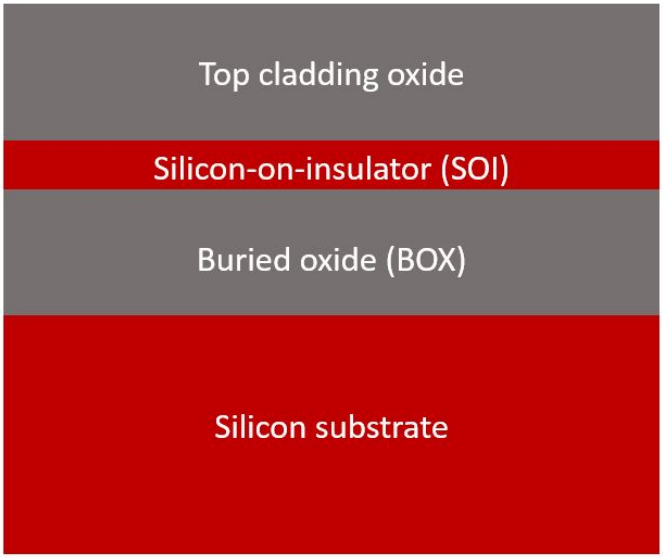

FIGURE 3.1: Cross-sectional side view of a silicon-on-insulator wafer.

Each foundry uses a different lithographic patterning technique to etch the waveguide structures in the crystalline silicon layer. AMF uses a deep ultraviolet (DUV) photolithography process with either a 193 nm or 248 nm wavelength, while ANT uses an electron beam lithography (EBL) process. Minimum feature sizes for the AMF and ANT processes are 180 nm and 60 nm, respectively. While this is not a concern for our wire waveguide designs with features much larger than these values, it would be a significant consideration for much smaller devices such as subwavelength structures.

Following wafer-scale fabrication, the wafer is diced into chips. Deep silicon trenches are created along the chip edges to facilitate fiber-chip edge coupling. The chips are then ready for post-process deposition at our facilities.

3.1.2 Tellurium oxide thin film deposition

Our tellurium oxide (TeO_2) films are deposited using our radio frequency (RF) **reactive magnetron sputtering system**, which is depicted in Figure 3.2 and described in

[1]No top cladding oxide may be requested (i.e. thickness = 0 μm)

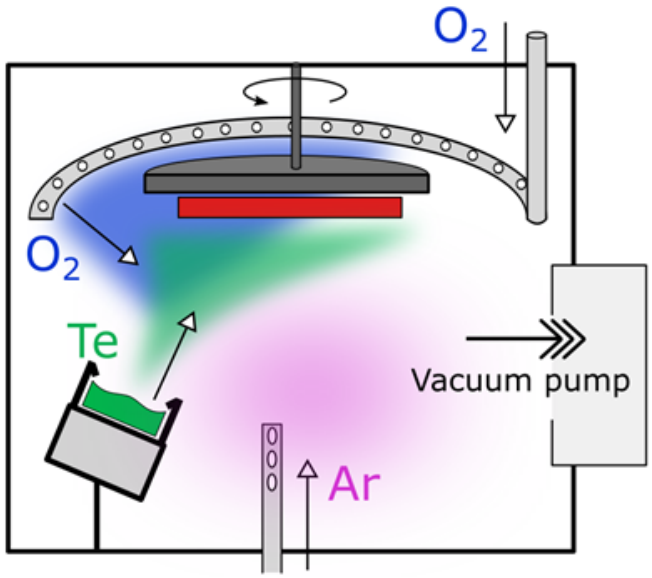

FIGURE 3.2: Radio frequency reactive magnetron sputtering system. Adapted from [48].

[17]. In this system, the sample chip receiving the film is inverted and mounted to a substrate holder within the sputtering chamber using carbon tape. A high purity, metallic tellurium (Te) target is sputtered using a magnetron sputtering gun that is driven by an RF power supply. Meanwhile, oxygen (O_2) and argon (Ar) are injected into the chamber via gas inlets near the sample holder and target material, respectively. The Ar flow rate is adjusted to maintain chamber pressure while the O_2 maintains a constant mass flow rate to achieve the appropriate film ratio. Previous studies have found a 2:1 stoichiometry ratio of oxygen to tellurium yields the lowest film losses [18, 25, 26] and is thus applied to all our depositions. The Te reacts with the oxygen-argon ambient at room temperature and the TeO_2 film adheres to the surface of the sample. The holder containing the loaded sample is located 15 cm away from the Te target and rotates at 8 rpm to enable film uniformity over the entire substrate area. In the case of active film depositions, a second magnetron gun holding a metallic rare-earth material target, such as erbium (Er^{3+}), is used simultaneously in the chamber [27]. The RF sputtering power

used on the second target varies depending on the desired dopant concentration of the deposited film.

Reactive sputtering provides many benefits over traditional chemical vapour deposition techniques, especially for our samples. First, this is a straightforward backend deposition procedure for chip-scale samples that are commonly used in exploratory research for new silicon photonics material platforms [49, 50]. Fast deposition rates are realized, ranging between 20-25 nm/min, and depositions can be carried out at room temperature, preserving film quality that enables low loss. Frankis et al. [17] reported film losses < 0.1 dB/cm for the fundamental transverse electric (TE) mode at 1550 nm wavelength light in TeO_2 films with thicknesses between 200 nm and 400 nm. The use of a high purity target material also eliminates the potential for hydrogen and hydroxide contamination in the deposited film that can cause luminescence quenching and lead to gain reduction in optically active films.

3.1.3 Design mask layout

TABLE 3.2: Design details of fabricated SOI wire waveguides

Parameter {Fig. 3.4 symbol}	Design #1 (AMF)	Design #2 (ANT)
Designated design space (mm x mm)	1 x 3	2.48 x 8.78
Test structures	1 Straight* 5 Paperclips	1 Straight* 3 Paperclips
Waveguide lengths (cm) {L*/L}	[0.3*, 0.47, 0.58, 0.69, 0.80, 0.93]	[0.9*, 1.4, 1.7, 2]
Waveguide widths (nm) {W}	450	[200, 250, 300, 350, 400]
1^{st} paperclip bend radius (μm) {R_1}	50	[230, 290, 50, 50, 290]
2^{nd} paperclip bend radius (μm) {R_2}	50	[110, 50, 290, 290, 50]
Total # of waveguides	6	20

We use Mentor Graphics Pyxis to generate high-resolution GDS files containing the mask layouts of our SOI wire waveguide designs, which are shown in Figure 3.3. Table 3.2 details the specific parameters of each waveguide structure featured on these designs. Straight waveguides and paperclip structures (containing two 180° bends) are

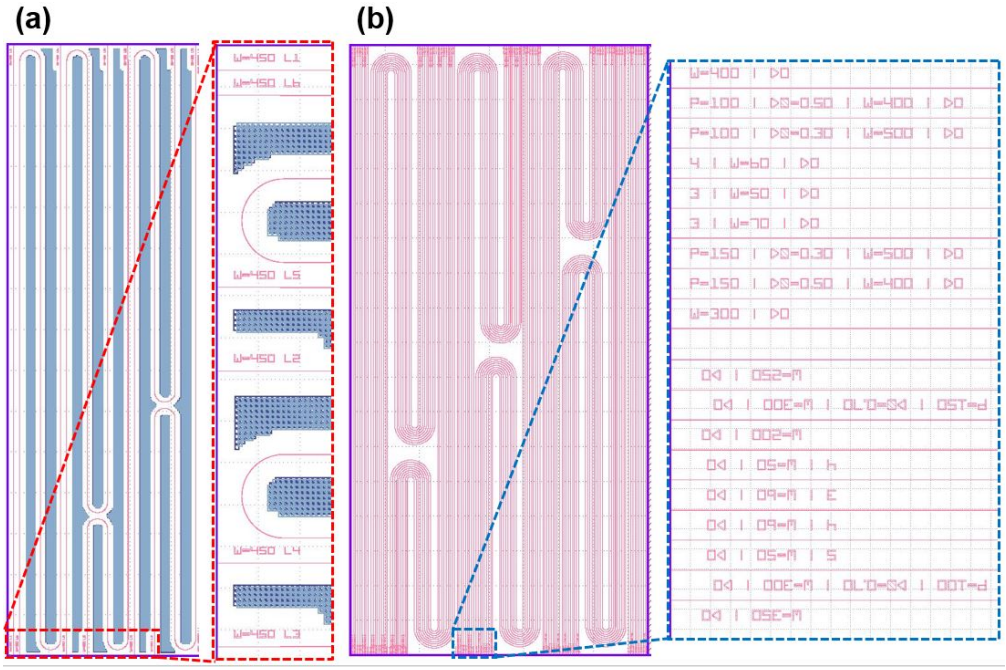

FIGURE 3.3: Mask layout overview with zoomed in images of the waveguide labels for the SOI wire waveguide structures submitted for fabrication with (a) AMF and (b) ANT.

implemented in the design to provide test structures with varying lengths for loss measurements via the cutback method. The waveguides are laid out on the mask to optimize chip space while enabling edge coupling on opposing sides of the chip, which is necessary for our experimental setup. The parameters in Table 3.2 that include symbols in brace brackets (**{}**) correspond to the symbols listed on the top view schematic shown in Figure 3.4. Symbols and values with an asterisk (*) beside them correspond to the straight waveguide structures, while all others correspond to paperclip structures. Figure 3.3 also includes zoomed-in images of the etched labels on each design used to help lab personnel quickly identify each waveguide as they measure. For the wire waveguide structures, only the width (W) and length (L) are indicated on the chip.

The AMF design, referred to as "Design #1", only has wire waveguide test structures with widths of 450 nm. We define these as **high-confinement waveguides**

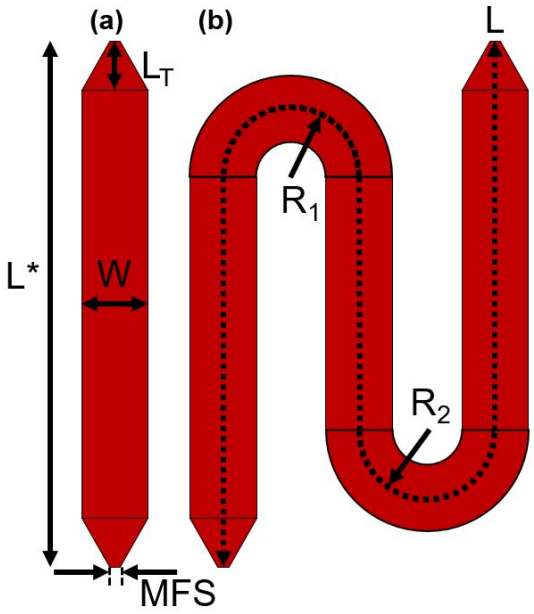

FIGURE 3.4: Top view schematic of (a) straight and (b) paperclip SOI wire waveguide structures included on both designs.

(HCWGs) since their comparatively higher width greatly confines the light within the silicon waveguide core and thus limits the overlap with the cladding material. These structures provide a baseline of what gain can be achieved in silicon wire waveguides coated in erbium-doped TeO_2 (TeO_2:Er^{3+}) while ensuring lower scattering losses. Higher confinement also enables smaller bend radius, which we fix at 50 μm for all bends. The width of every waveguide bend matches the connecting straight waveguide structures—in this case, 450 nm. Smaller lengths (< 1 cm) are used due to the design space limitations on the MPW run. We include 75 μm-long tapers ($L_T = 75$ μm) on both the input and output of each waveguide structure that reduce to a width of 180 nm (the minimum feature size of the AMF fabrication process) at the edge facet in order to maximize overlap with the fiber mode and reduce coupling loss. Figure 3.5 shows SEM images of these waveguide edge facets, both without and with TeO_2 cladding.

The ANT design, referred to as "Design #2", includes wire waveguide test structures with widths varying between 200 nm and 400 nm. We define these as **high-overlap**

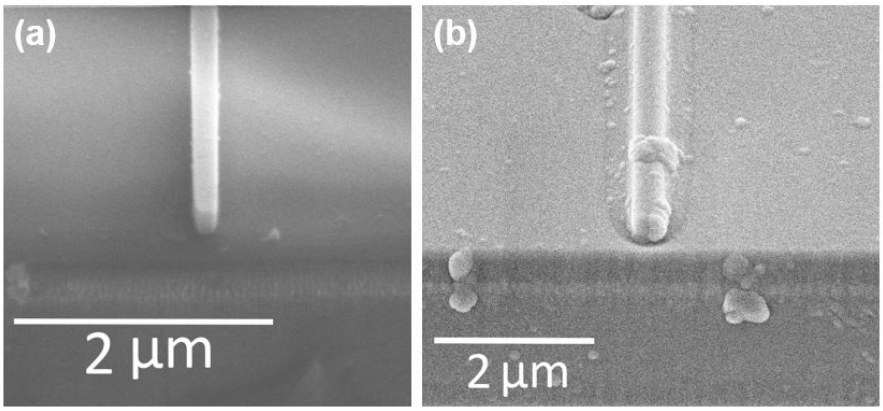

FIGURE 3.5: Scanning electron microscope (SEM) images of the edge facet of the (a) uncoated and (b) 101 nm-thick TeO_2-coated high-confinement SOI wire waveguides fabricated by AMF.

waveguides (HOWGs) because their comparatively lower width enables a higher overlap with the cladding gain material. Waveguide bend structures included here vary dependent on the waveguide width. Total bend length in each structure is constant, with the sum of each bend radius equaling 340 μm. Each bend radius listed in Table 3.2 for this design corresponds to the waveguide width it is under. A minimum bend radius of 50 μm is used for all waveguide structures apart from the 200 nm-wide waveguides which have a minimum bend radius of 110 μm. This is done to prevent significant leakage from the thinner bend structure. Tapers at the edge facets included in the AMF design are excluded from this design as the waveguide widths are already reduced and held constant throughout each device.

3.2 Design

3.2.1 Finite element method mode solver simulations

We use FemSIM, the 2D mode solver tool in Synopsys RSoft [32] based on the Finite Element Method (FEM) to characterize the design and modal performance of our proposed waveguide structures. The FEM is a numerical technique for solving partial differential

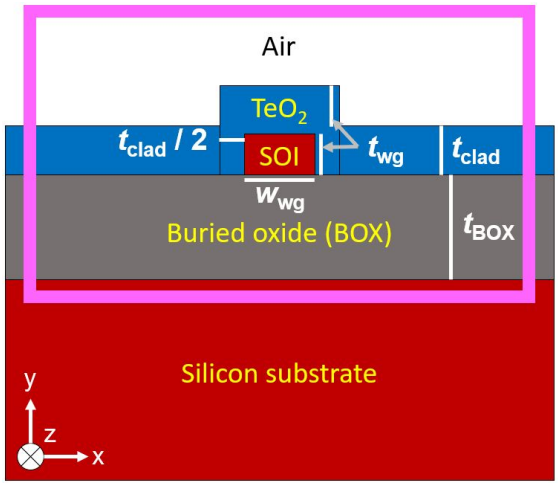

FIGURE 3.6: Cross-sectional schematic of the simulated TeO_2-coated SOI wire waveguide structure.

TABLE 3.3: Waveguide parameters and their variations in the RSoft simulations.

Parameter Variables	Symbol	Range (μm)
Waveguide Width	w_{wg}	[0.2 : 0.05 : 0.45]
TeO_2 Cladding Thickness	t_{clad}	[0.1 : 0.025 : 0.35]
Wavelength	λ	[1.48, 1.55]

equations and has a wide range of applications in the STEM disciplines [51]. In photonics, its non-uniform meshing algorithm offers low computational expense for arbitrarily shaped structures with multiple perturbations, such as optical waveguides [52, 53].

Figure 3.6 shows the cross-sectional schematic of the FEM simulation setup we use to solve the modes of our proposed device. Table 3.3 lists the parameters which we vary and scan through using MOST, RSoft's built-in optimizer/scanner. 1480 nm and 1550 nm are selected and tested as the pump and signal wavelengths, respectively, which we will use experimentally to test our erbium-doped waveguide amplifiers (EDWAs). Our fabricated waveguides range between 200 nm and 450 nm in width, and the TeO_2 cladding thickness may be adjusted from tens of nanometers to micron-scale thickness. The waveguide thickness (t_{wg}) is fixed at 220 nm due to fabrication standards, as indicated in Table 3.1.

The geometry of optical waveguides is essential in determining which modes a waveguide can support, or guide. In general, a mode is supported if its effective refractive index is higher than the refractive index of the surrounding cladding material, which is usually SiO_2 ($n \sim 1.444$) for silicon-based waveguides. In this thesis, we are only interested in supporting the fundamental modes in our waveguides as they are the most well-confined modes, having the highest effective refractive index, and carry most of the optical power [6]. Back in Section 2.1.2, the wave vector of a wave striking a dielectric interface within a planar waveguide structure was decomposed. From this analysis, it was determined that the single mode condition for an SOI planar waveguide structure, similar to the one depicted in Figure 3.1, is fulfilled such that $h < 243$ nm, where h is the thickness of the SOI waveguide layer. The 243 nm thickness is referred to as the **single mode cutoff** (SMC) thickness for SOI waveguides. A SMC defines a geometric waveguide parameter (i.e. thickness or width) quantity in which the waveguide stops supporting higher order modes. It is the maximum value for this given parameter such that the single mode condition is satisfied. 220 nm thickness for SOI waveguide layers has become standard for many SOI foundries because it lies well below this SMC thickness.

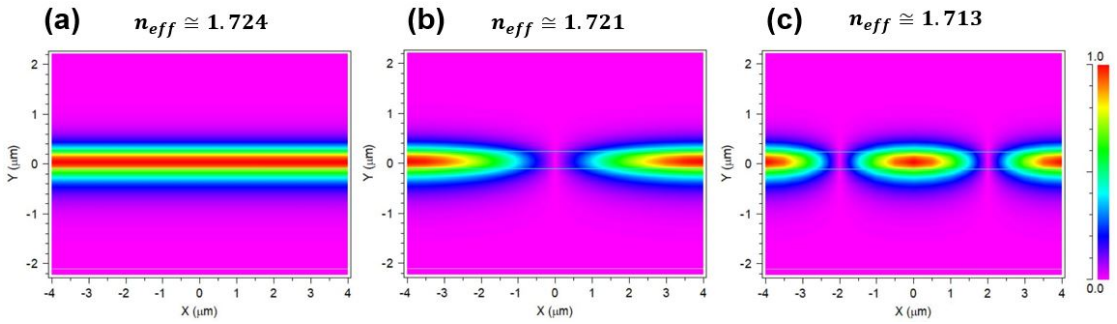

FIGURE 3.7: Mode profiles for the (a) zeroth, (b) first, and (c) second order TE modes for a 300 nm-thickness TeO_2 slab waveguide structure.

The SMC mentioned above only applies to SOI waveguides surrounded by SiO_2 cladding on both sides. Because we use TeO_2 as a top cladding material, the threshold refractive index that defines modal guidance is higher than the typical value of 1.444

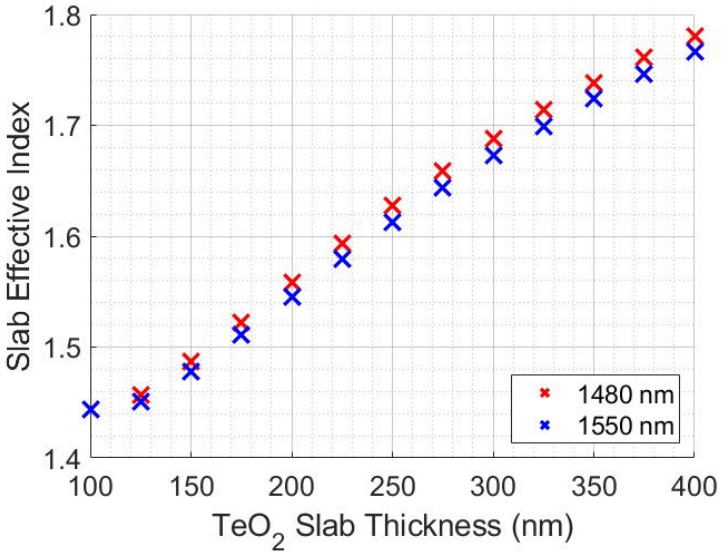

FIGURE 3.8: RSoft FemSIM simulation results for the fundamental slab mode effective index calculations with varying TeO_2 slab thicknesses at 1480 nm and 1550 nm wavelengths.

and varies dependent on the TeO_2 cladding thickness. We use RSoft FemSIM to simulate a TeO_2 slab waveguide structure (like that in Figure 3.6 but without the silicon waveguide and increased TeO_2 ridge height) to calculate the slab effective index of our device. Figure 3.7 depicts the first three slab mode profiles (zeroth, first and second order modes, respectively) for our structure with a TeO_2 thickness of 300 nm. The effective index results of each slab mode are also included above their mode profile. As expected, the fundamental mode has the highest real effective index of 1.724. For this TeO_2 thickness, once the silicon waveguide is re-introduced in the simulation, if its geometric conditions are inadequate to support a given mode, the mode effective index will be less than 1.724, indicating modal leakage out of the silicon waveguide and into the TeO_2 film where guidance is not insured. We use this method to calculate the threshold indices in which modal guidance is supported, simply referred to as the "cut-off", for multiple TeO_2 cladding thicknesses and display the results in Figure 3.8.

This thesis deals with channel, or wire, waveguides, which, unlike planar waveguide

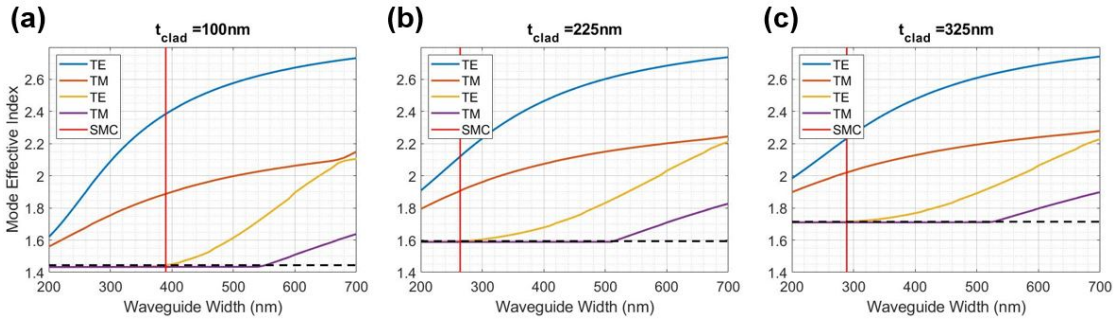

FIGURE 3.9: Single mode conditions for TeO_2 cladding thicknesses of (a) 100 nm, (b) 225 nm and (c) 325 nm at 1480 nm wavelength.

structures, are confined in two dimensions. Single mode wire waveguides are defined as waveguides that only support the fundamental TE and TM modes in the horizontal (x) and vertical (y) directions. Once a third mode (i.e. second-order TE mode) is supported, the single mode condition is no longer satisfied. Our waveguides maintain the 220 nm standard silicon waveguide thickness due to the MPW fabrication services we employ–AMF and ANT–so multi-mode conditions in the y-direction are not a concern. However, if the waveguide width is set too high, multi-mode behaviour may be possible in the x-direction [54].

We use RSoft's built-in optimizer/scanner, MOST, and FemSIM to conduct single mode condition calculations by sweeping over multiple waveguide width values and plot them against the calculated real mode effective indices for the first four modes. Figure 3.9 depicts the results for three structures with different TeO_2 cladding thicknesses. The black dotted line in each figure represents the cut-off calculated from Figure 3.8 for each corresponding TeO_2 cladding thickness. Effective index values above the cut-off indicate that modal guidance is supported by the SOI waveguide. To meet the single mode condition, only the first TE and TM mode may be supported. Once a second TE or TM mode has crossed the cut-off threshold, the waveguide supports that mode and is no longer single mode. This occurs with increasing waveguide width as wider waveguides are known to support multiple modes. The red line in each figure indicates the SMC

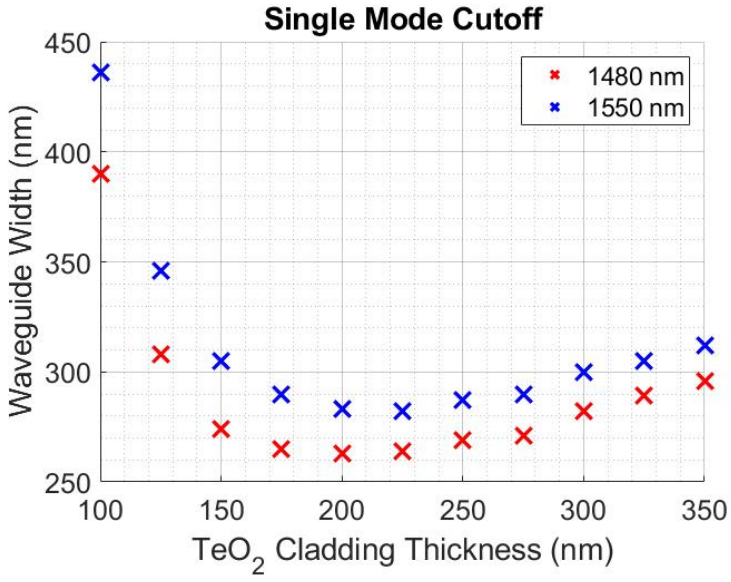

FIGURE 3.10: Single mode cutoff values for various SOI waveguide structures with different TeO_2 cladding thicknesses at 1480 nm and 1550 nm wavelengths.

width, or maximum waveguide width in which the waveguide remains single mode. All waveguide widths above this SMC display a second TE mode with a mode effective index greater than the cut-off threshold, and therefore support multi-mode behaviour. For TeO_2 cladding thicknesses of 100 nm, 225 nm and 325 nm, the SMCs for 1480 nm wavelength light are 390 nm, 264 nm and 289 nm, respectively. The SMCs are calculated for other TeO_2 cladding thicknesses using this method and are summarized in Figure 3.10. Thinner TeO_2 films have a much lower slab mode effective index and are less likely to support higher order modes, thus raising the SMC significantly. Furthermore, if the TeO_2 film is very thick, the width of the TeO_2 ridge that results from the high uniformity of the film deposition over the waveguide increases. This ridge forms its own rib-like waveguide structure that can efficiently support a large single mode while discarding higher order modes into its thick slab region. The single mode condition must be satisfied for both 1480 nm and 1550 nm wavelengths in our devices. Thus, we use the SMC values at 1480 nm since 1480 nm light is more susceptible to multi-mode

behaviour than 1550 nm light. This is evident in the higher mode effective indices 1480 nm displays in Figure 3.8 and is a condition of the relation in Eq. (2.15).

Confinement factor is another figure of merit that is important in establishing modal guidance in waveguides. It is defined as the ratio of optical power residing within a given area of the waveguide and the overall optical power. For SOI waveguides, this area is the silicon waveguide core, which we will defined as **Si confinement factor** (Γ_{Si}). A high Si confinement factor implies that most of the waveguide mode is focused inside of the silicon waveguide core, which is representative of lower waveguide loss and scattering losses caused by sidewall interactions. While this is generally important for all waveguides, our waveguides actually benefit from a lower Si confinement factor. Our amplifiers acquire gain through light-matter interaction between the light sources and the active TeO_2 cladding material. We will quantify the amount of optical power residing in the TeO_2 cladding as the **TeO_2 confinement factor** (Γ_{TeO_2}). Generally, the higher the TeO_2 confinement factor, the higher the gain, which is essential in our devices. TeO_2 has the benefit of higher refractive index, which will attract the mode more than lower index claddings, thus increasing the TeO_2 confinement factor. Furthermore, the mode will expand, increasing the **mode effective area** (A_{eff}), which also increases the overlap with the TeO_2. A mode effective area too high may limit the guiding capabilities of the waveguide and increase interface induced scattering. However, utilizing a Si waveguide core maintains the confinement of the mode and balances the above parameters.

RSoft FemSIM enables calculation of the partial power percentage of the overall mode in various regions of the simulation window and the overall mode effective area using pathway monitors. With this feature, the Si confinement factor, TeO_2 confinement factor and mode effective area can be calculated for a given waveguide device. Figure 3.11 shows the Si confinement factor, TeO_2 confinement factor and mode effective area results for simulated waveguide structures with various waveguide widths and TeO_2 cladding

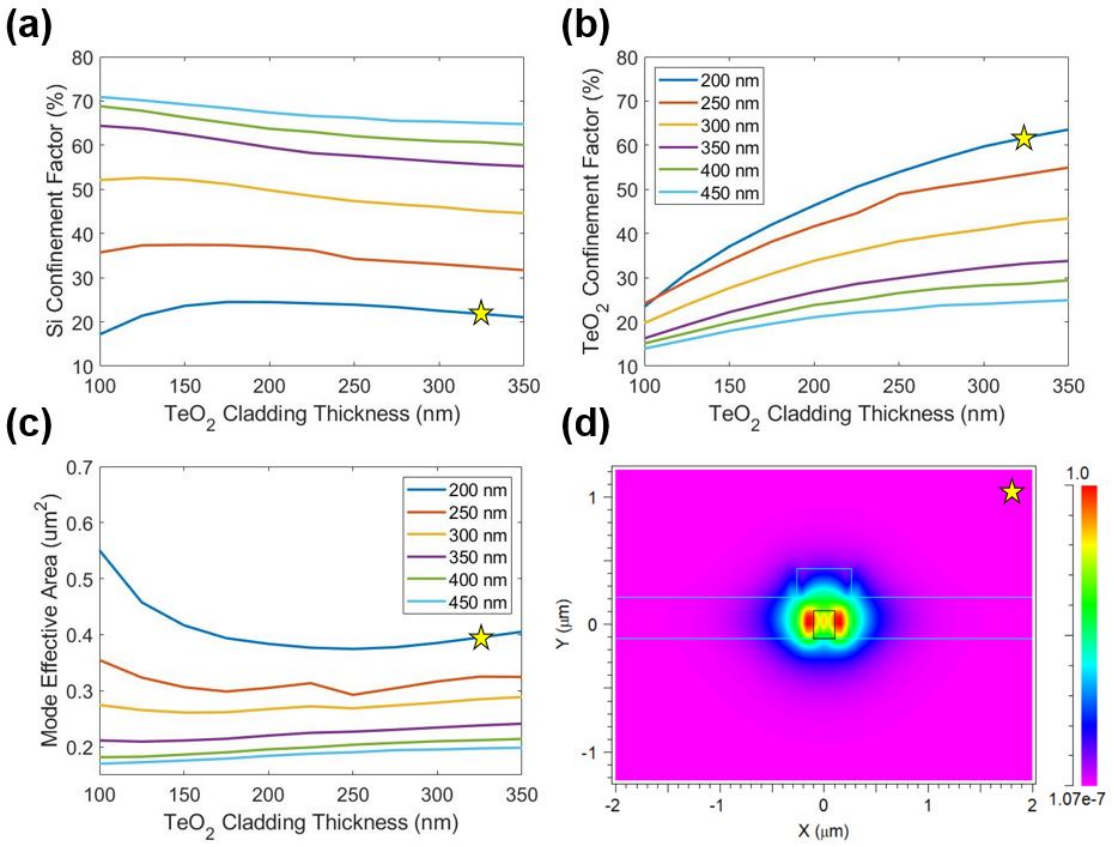

FIGURE 3.11: TeO_2 cladding thickness vs. (a) Si confinement factor, (b) TeO_2 confinement factor and (c) mode effective area of our waveguide structures with various waveguide widths at 1550 nm wavelength. Yellow stars correspond to (d) fundamental mode profile of waveguide structure with 200 nm waveguide width and 325 nm TeO_2 cladding thickness.

thicknesses. Generally, mode effective area scales proportionally with TeO_2 confinement factor and inversely with Si confinement factor. Waveguide width has the largest effect on these results and is what we use to define our waveguides as either high-confinement ($w_{wg} > 400$ nm) or high-overlap ($w_{\text{wg}} \leq 400$ nm). The mode profile included in Figure 3.11 corresponds to a waveguide structure with 200 nm waveguide width and 325 nm TeO_2 cladding thickness, which we classify in this thesis as a high-overlap waveguide (HOWG) that is expected to exhibit significantly higher gain than a high-confinement waveguide (HCWG).

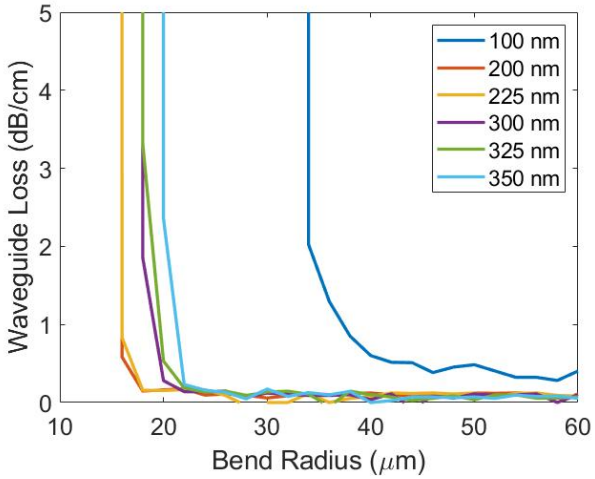

FIGURE 3.12: Bend radius vs. waveguide loss of our 200 nm width waveguide structures with various TeO_2 cladding thicknesses.

The use of paperclip waveguide structures introduces 180° bends that may introduce additional waveguide loss, so it is important to simulate these bends and quantify this loss. The main contributing factor to this loss is the bend radius. The smaller, or tighter, the bend radius is, the higher the loss since the light is less equipped to adjust to the nonlinear path change in the waveguide, causing leakage in the outer direction of the bend. RSoft has a built-in bend simulator that allows a given bend radius to be simulated and the mode profile to be calculated using FemSIM. The calculated waveguide loss is based off a modified version of the Discrete Spectral Index method [55] and is given by:

$$loss(dB) = 10\log_{10}(e) \cdot 4\pi n_i/\lambda_0 \tag{3.1}$$

where n_i is the imaginary effective refractive index calculated in RSoft using perfectly matched layer (PML) boundary conditions and λ_0 is the center wavelength (in this case, 1550 nm) [56]. Figure 3.12 shows the waveguide loss plotted against bend radius for a 200 nm-wide waveguide with various TeO_2 cladding thicknesses. The loss is consistent when the bend radius is sufficiently large. However, as it is decreased, a point is reached where the loss drastically increases, indicating a complete loss of modal guidance. We

select 50 μm as a minimum bend radius in all our structures as it shows waveguide losses of < 0.5 dB/cm for all simulated waveguide structures. We disregard simulations for higher waveguide widths as they will have larger confinement factors that result in smaller overall bend losses.

3.2.2 Optical gain characterization & amplifier model

We simulate the performance of our optical waveguide amplifiers using a model scripted in Matlab, which is attached in Appendix A. Our model is based off previous EDWA models that include the parameters discussed in Chapter 2, which are determined either from experiment or prior literature review, to solve the rate and propagation equations of their respective systems. These models include erbium-doped alumina (Al_2O_3:Er^{3+}) cladding [41] and erbium-doped TeO_2 (TeO_2:Er^{3+}) cladding [57] which each implement a 3-level energy system due to usage of a 980 nm pump source. Our model has been adjusted for a 2-level energy system that incorporates a 1480 nm pump source due to the presence of silicon in our devices.

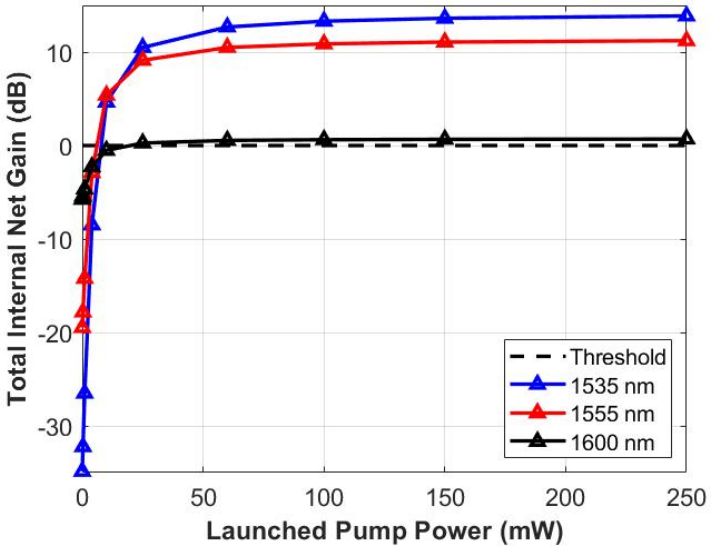

FIGURE 3.13: Launched pump power vs. (a) signal enhancement at different wavelengths and (b) signal enhancement and internal net gain at 1535 wavelength for model validation using results from [19].

TABLE 3.4: Summary of TeO_2:Er^{3+} amplifier model validator [19]

Parameter Variables	Symbol	[19]	Source
Pump Wavelength (nm)	λ_p	1475	[19]
Signal Wavelength (nm)	λ_s	1535	[19]
Mode effective area, pump (μm^2)	$A_{\text{eff,p}}$	5.24	RSoft
Mode effective area, signal (μm^2)	$A_{\text{eff,s}}$	5.32	RSoft
TeO_2 confinement factor, pump (%)	Γ_p	100	N/A
TeO_2 confinement factor, signal (%)	Γ_s	100	N/A
Absorption cross section, pump (10^{-21} cm^2)	$\sigma_p^{(a)}$	3.54	[27]
Absorption cross section, signal (10^{-21} cm^2)	$\sigma_s^{(a)}$	6.49	[27]
Emission cross section, pump (10^{-21} cm^2)	$\sigma_p^{(e)}$	1.03	[45]
Emission cross section, signal (10^{-21} cm^2)	$\sigma_s^{(e)}$	6.91	[45]
Fluorescent lifetime (ms)	τ	1.3	[19]
Background loss, pump (dB/cm)	α_p	0.6	[19]
Background loss, signal (dB/cm)	α_s	0.4	[20]
Parameters of Interest	//	//	//
Amplifier length (cm)	L	5	[19]
Er concentration (10^{20} cm^{-3})	N	2.2	[19]
Launched power, signal (μW)	$P_{s,0}$	10	[19]
Launched power, pump (mW)	$P_{p,0}$	250	[19]
Results	//	//	//
Total internal net gain (dB)	G	14 13.87	[19] [Our model]
Internal net gain (dB/cm)	γ	2.8 2.77	[19] [Our model]

We validate our model by using data and results from [19], which uses a 1475 nm pump source to excite erbium in a hybrid doped/undoped TeO_2 rib waveguide structure. The details of the parameters and results used to model this device are summarized in Table 3.4. Some of the parameters that are not mentioned in the literature are substituted using our data and methods, namely mode effective area and the cross sections. TeO_2 confinement factor is assumed to be ideal. The resulting plots from the model are highlighted in Figure 3.13 with a peak total internal net gain of 13.87 dB and internal net gain per unit length of 2.77 dB/cm at a launched pump power of 250 mW. This closely matches the peak total internal net gain and internal net gain per unit length results from [19] within a $\pm$ 0.2 dB and $\pm$ 0.1 dB/cm discrepancy, respectively, thus

verifying good accuracy within our model.

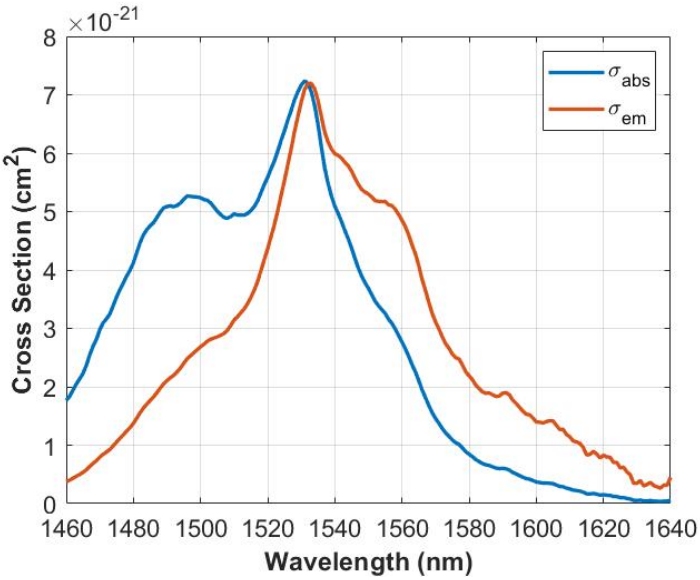

FIGURE 3.14: Wavelength vs. measured absorption cross section and calculated emission cross section via McCumber-Miniscalco-Quimby Theory [45].

Our 1-D model uses the rate equations and propagation equations based on the 2-level energy system of erbium discussed in Section 2.2.3 to determine the erbium population states and light intensity in the amplifier along the longitudinal (z) axis. Light amplification in a 2-level energy system is made possible by Stark splitting and inhomogeneous broadening of the Er^{3+} orbitals. Thus, McCumber Theory [44] specified in Eq. (2.24) may be applied to describe the relationship between the absorption and emission cross sections ($\sigma^{(a)}(\lambda)$ and $\sigma^{(e)}(\lambda)$, respectively). The absorption cross sections of our TeO_2:Er^{3+} films were determined experimentally [27]. McCumber-Miniscalco-Quimby Theory [45] provides a good estimation of the mean transition energy ϵ, but requires detailed knowledge of the Stark-manifolds within the $^4I_{15/2}$ and $^4I_{13/2}$ energy levels of the doped Er^{3+} ions, which are currently unknown for our films. We assume the ϵ value corresponds to a wavelength of 1532 nm, which was used in [58] and aligns with the peak absorption cross section in our measured data. The emission cross section

is then solved using Eq. (2.24) for each wavelength and is plotted against our measured absorption cross section in Figure 3.14. Notice how the the absorption and emission cross sections are only equal at a crossing frequency $\nu_c \equiv \epsilon/h$ corresponding to $\lambda = 1532$ nm, and that $\sigma^{(a)}(\lambda) < \sigma^{(e)}(\lambda)$ when $\nu < \nu_c$ and vice versa for $\nu > \nu_c$, therefore satisfying the conditions of McCumber-Miniscalco-Quimby Theory.

TABLE 3.5: Simulated waveguide parameters in RSoft for amplifier model.

Waveguide Design	Design #1 (HCWG)	Design #2 (HOWG)
Waveguide Length (mm)	0.93	1.70
Waveguide Width (nm)	450	200
TeO_2 Thickness (nm)	121	330
TeO_2 Refractive Index	1.986	2.071

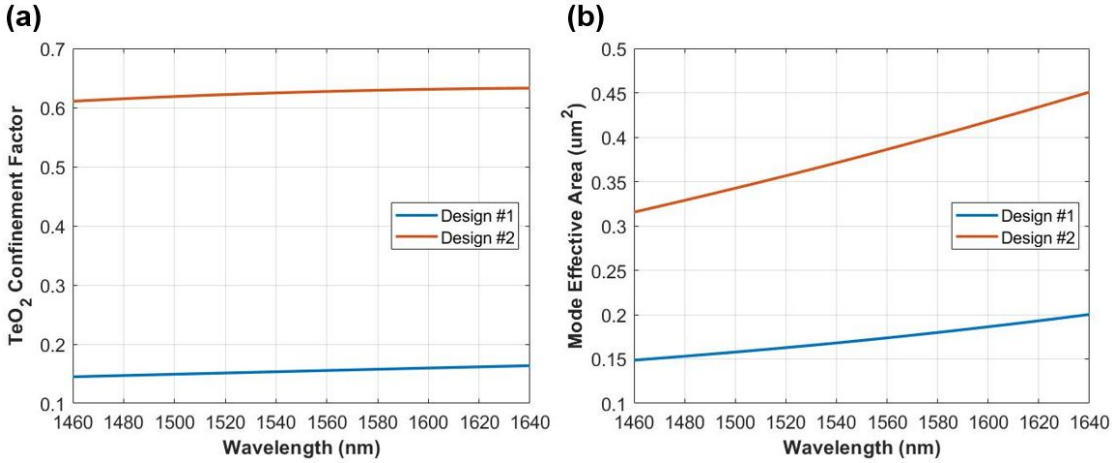

FIGURE 3.15: Wavelength vs. (a) TeO_2 confinement factor and (b) mode effective area for both designs described in Table 3.5.

We account for the waveguide geometry of our designs to quantify the modal parameters in the model—TeO_2 confinement factor and mode effective area. We use the methods in Section 3.2.1 above to simulate these parameters in RSoft FemSIM across a series of wavelengths for the waveguides described in Table 3.5, which will be measured experimentally and described in Section 4.2.2. The RSoft results are shown in Figure 3.15. Both the TeO_2 confinement factor and mode effective area are very low for the HCWG and significantly higher in the HOWG, as expected. Our fluorescent lifetime

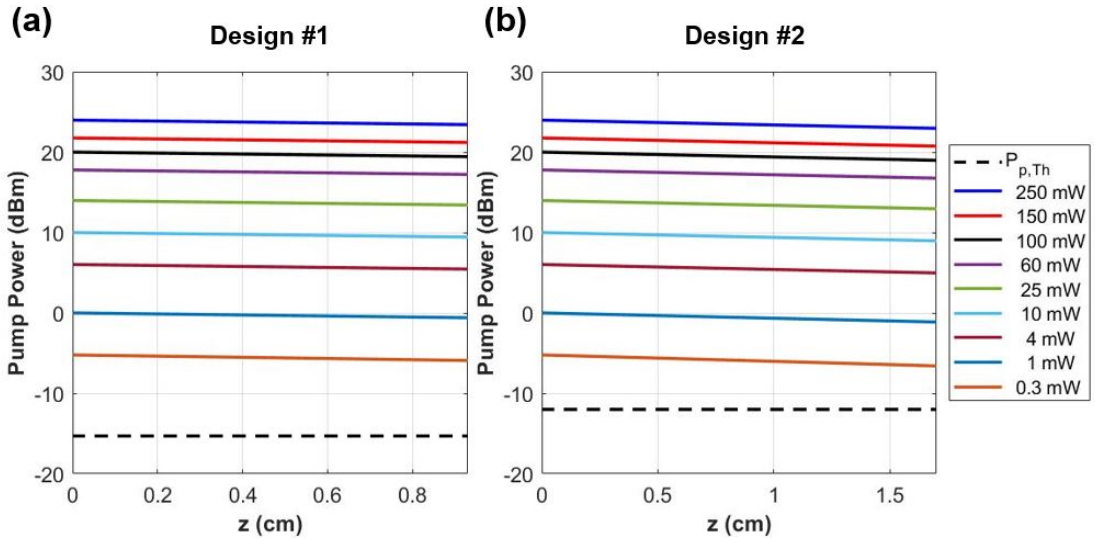

FIGURE 3.16: Position z along the amplifier length vs. pump power for (a) Design #1 and (b) Design #2 at 1533 nm wavelength and various pump powers.

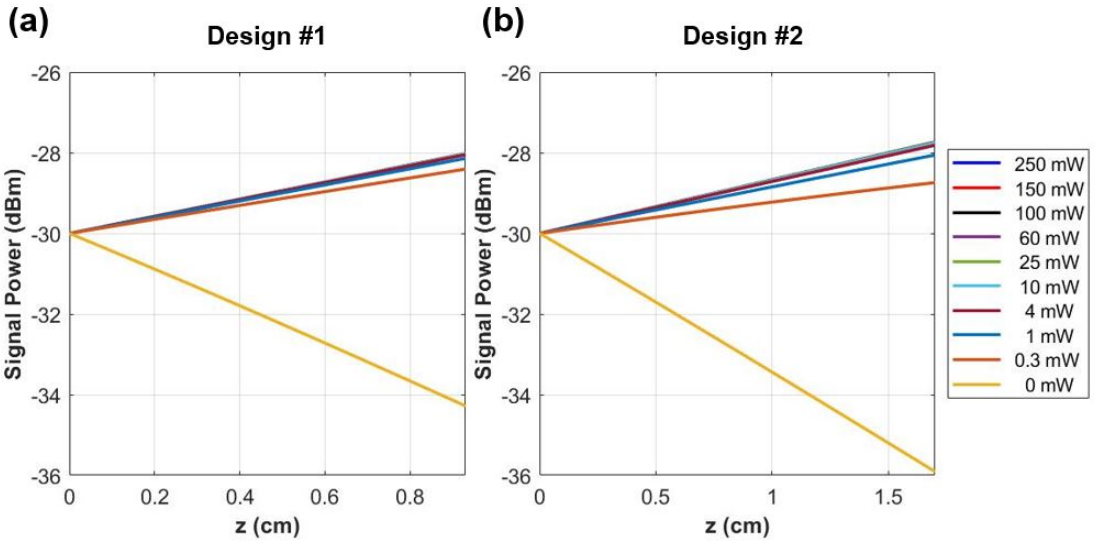

FIGURE 3.17: Position z along the amplifier length vs. signal power for (a) Design #1 and (b) Design #2 at 1533 nm wavelength and various pump powers.

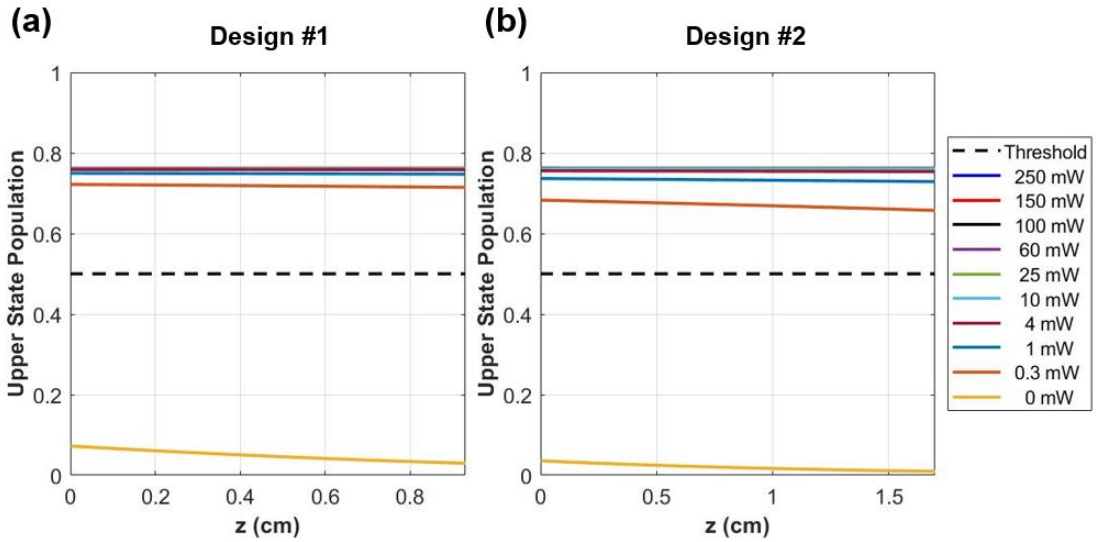

FIGURE 3.18: Position z along the amplifier length vs. upper state population for (a) Design #1 and (b) Design #2 at 1533 nm wavelength and various pump powers.

value is taken from [57], who used the same deposition system and the film has been previously characterized. Energy transfer upconversion (ETU), excited state absorption (ESA) and amplified spontaneous emission (ASE) are all excluded from this model and are outside the scope of this thesis.

Initial analysis of our amplifier investigates the effect of various launched pump power on the pump power, signal power and population states along the z axis for our two fabricated designs, which are plotted in Figures 3.16, 3.17 and 3.18, respsectively. Figure 3.16 displays a gradually decaying pump source due to stimulated absorption as it travels through the waveguide. This occurs simultaneously as incoming signal photons interact with the excited ions and cause stimulated emission, which increases the signal power, as seen in Figure 3.17. This is the case if population inversion is achieved ($N_2 > N_1$) at a given z position, which is indicated in Figure 3.18 as an upper state population (N_2/N) above 0.5 (the black dotted line). Eventually, the power of the pump source will decay below the pump threshold power determined by Eq. (2.32). At this point, signal gain at the signal wavelength ($dI_s/dz > 0$) no longer occurs and the signal power will begin to

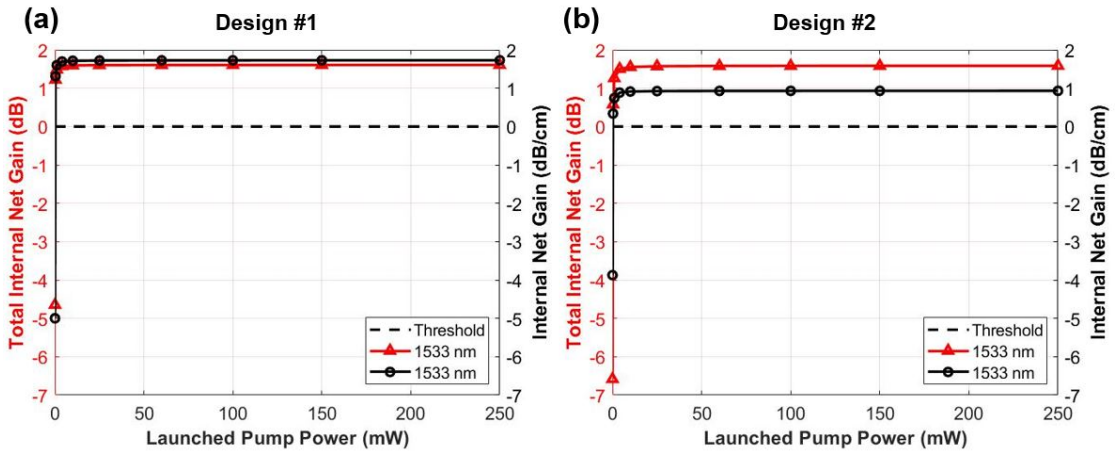

FIGURE 3.19: Launched pump power vs. total internal net gain and internal net gain per unit length for (a) Design #1 and (b) Design #2 at 1533 nm wavelength.

decrease. For each case in these figures, this does not occur and population inversion is maintained for each launched pump power. This indicates that the selected waveguide lengths are too short since the gain saturation regime has not yet been reached. The optimal amplifier length is determined by the relation in Eq. (2.32) for each given launched pump power and is explored later in this chapter for these waveguides.

This initial analysis gives us insight to the total internal net gain and internal net gain per unit length described by Eq. (2.36) and Eq. (2.37), repsectively. We equate the total background absorption in our model to the loss due to passive processes only ($\alpha_{Total}(\lambda) = \alpha_{pas}$), which are explained in Section 2.1.4. The total internal net gain and internal net gain per unit length results are depicted against launched pump power in Figure 3.19 for 1533 nm wavelength and against wavelength in Figure 3.20 for various launched pump powers. Both designs show gain saturation above 4 mW launched pump power, most likely due to the short waveguide lengths. For a signal wavelength of 1533 nm and a launched pump power of 250 mW, the model displays total internal net gain values of 1.61 dB and 1.58 dB and peak internal net gain per unit length values of 1.73 dB/cm and 0.93 dB/cm for Design #1 and Design #2, respectively. Both designs exhibit

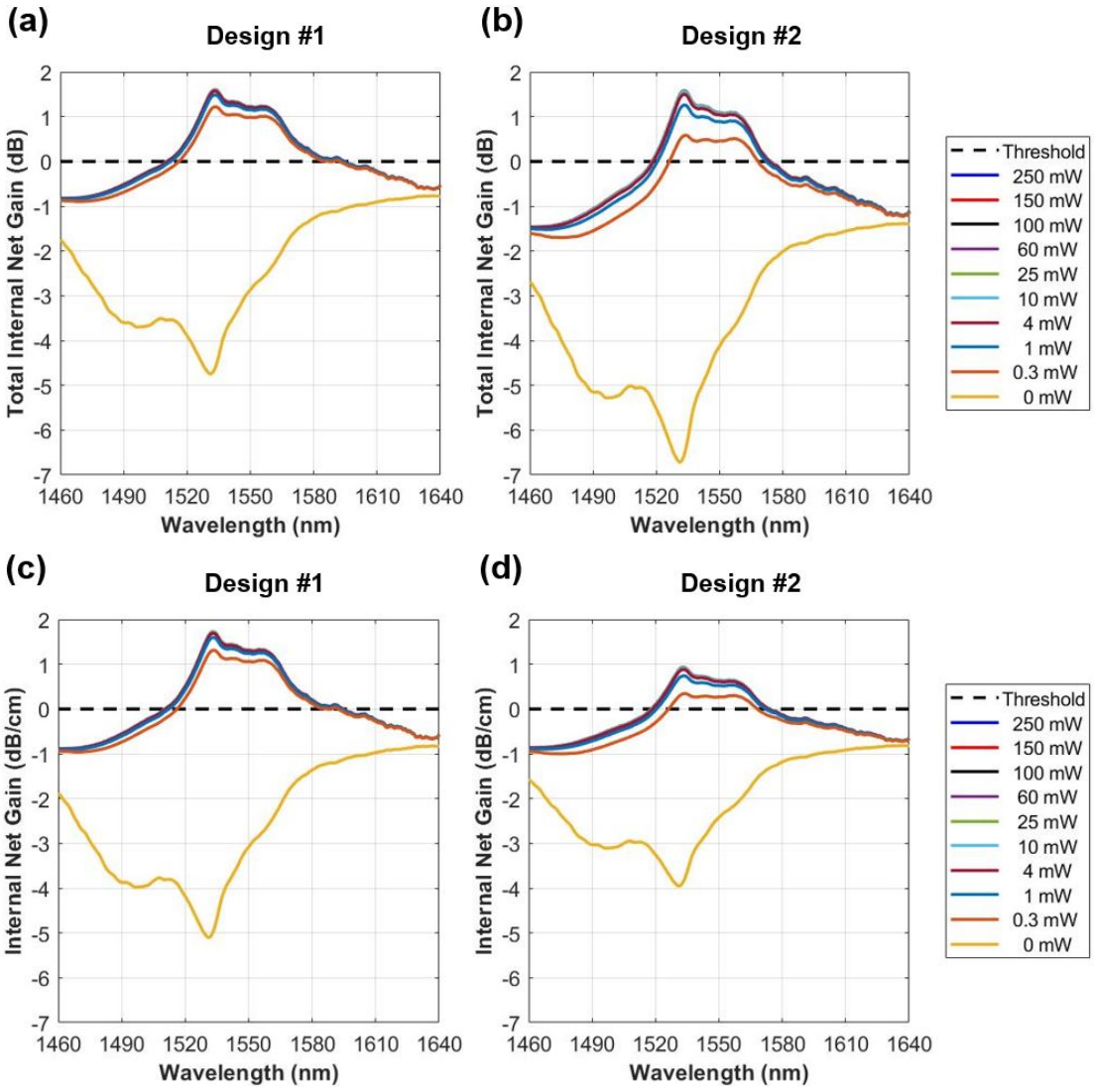

FIGURE 3.20: Wavelength vs. (a-b) total internal net gain and (c-d) internal net gain per unit length for (a,c) Design #1 and (b,d) Design #2 at various launched pump powers.

a very similar total internal net gain. However, the internal net gain per unit length of Design #2 is much smaller than that of Design #1 due to its greater waveguide length.

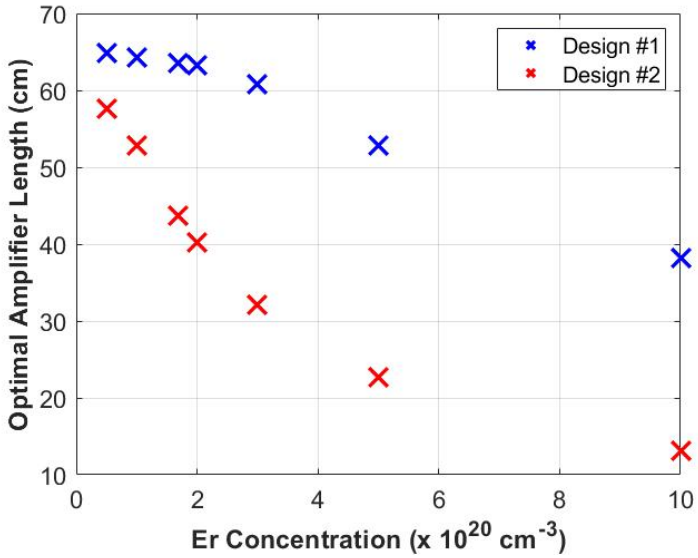

FIGURE 3.21: Erbium dopant concentration vs. optimal amplifier length for both designs at 1533 nm wavelength and 250 mW launched pump power.

These gain results are much lower than that of [19] for a couple of reasons. First, the gain medium overlap is much higher in [19] than in our designs, enabling higher overall light intensities, light-matter interaction and achievable optical gain. Second, the amplifier length is not optimized accordingly to the maximum launched pump power and each chosen erbium concentration. We can modify the model to calculate the optimal amplifier length at various erbium concentrations for each waveguide design and plot it like in Figure 3.21. Amplifiers with higher erbium concentrations operate better at short lengths since the pump light is absorbed more rapidly and becomes saturated more quickly. This statement is evident in Figure 3.21 by the decrease in optimal amplifier length with increasing erbium concentration. Our design selections of 10.0 x 10^{20} cm^{-3} Er concentration for Design #1 and 1.68 x 10^{20} cm^{-3} Er concentration for Design #2 output optimal amplifier lengths of 38.22 cm and 43.75 cm, respectively. A much wider

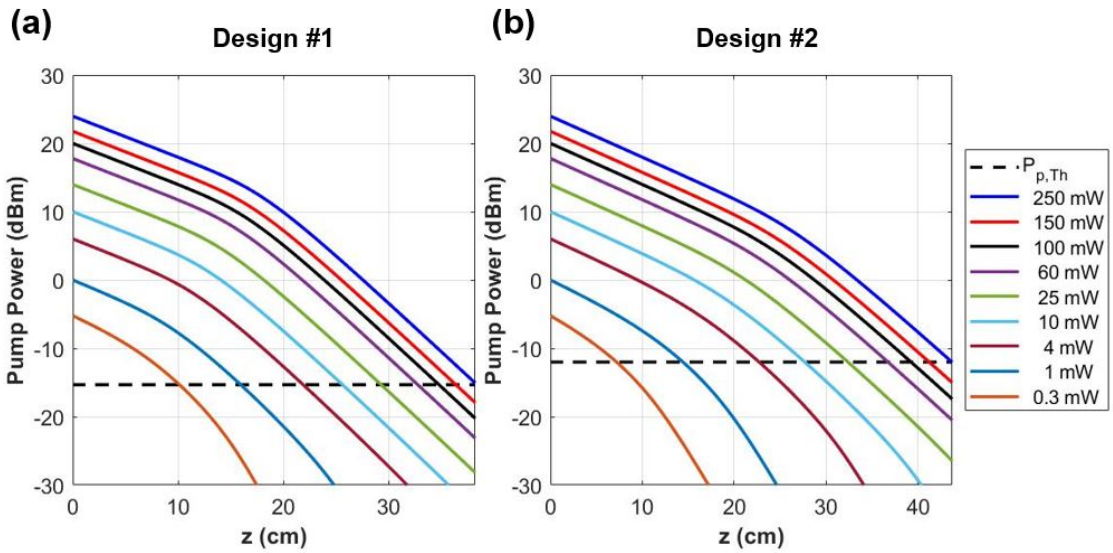

FIGURE 3.22: Position z along the optimal amplifier length vs. pump power for (a) Design #1 and (b) Design #2 at 1533 nm wavelength and various pump powers.

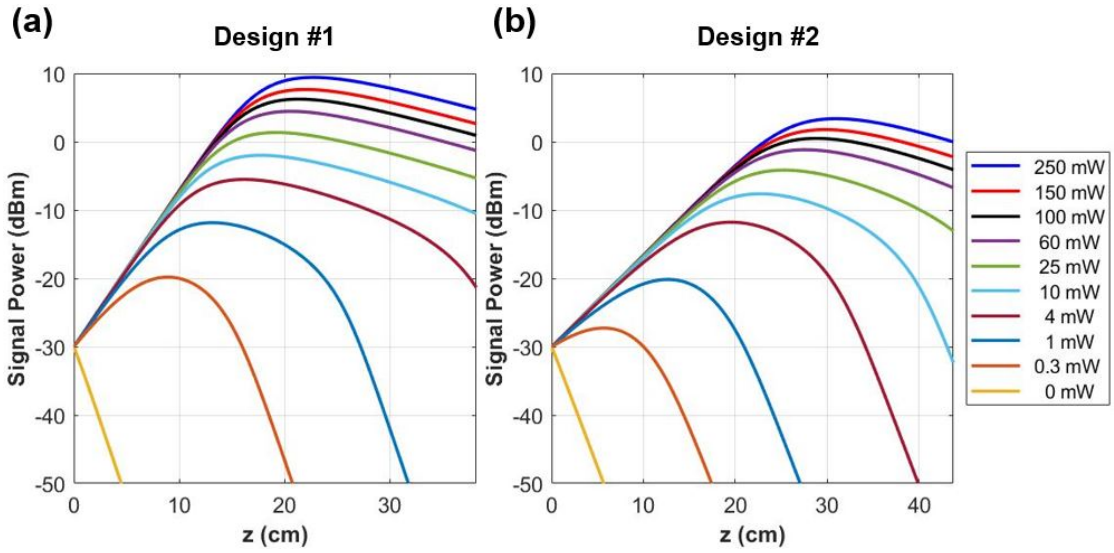

FIGURE 3.23: Position z along the optimal amplifier length vs. signal power for (a) Design #1 and (b) Design #2 at 1533 nm wavelength and various pump powers.

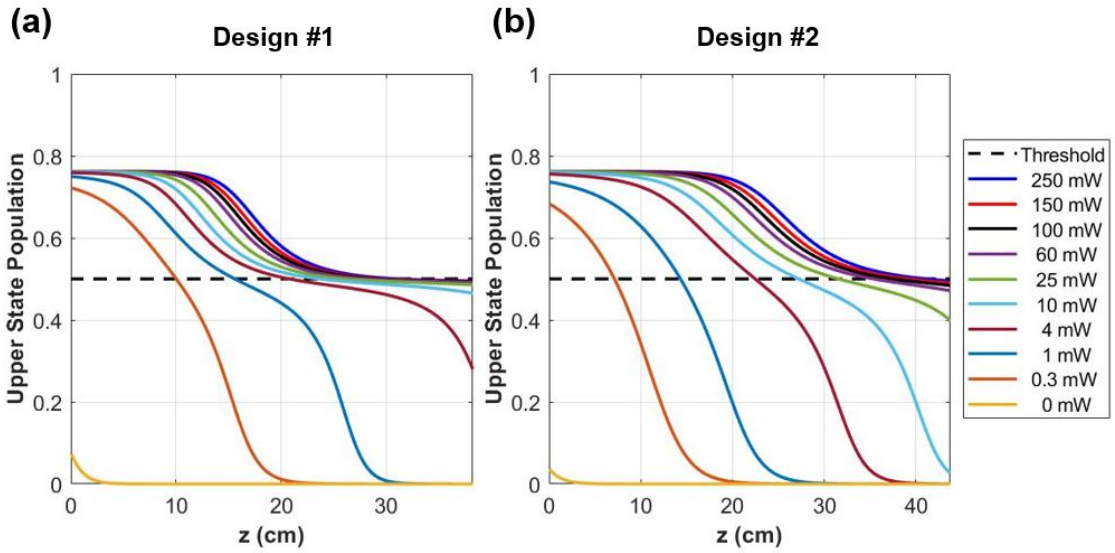

FIGURE 3.24: Position z along the optimal amplifier length vs. upper state population for (a) Design #1 and (b) Design #2 at 1533 nm wavelength and various pump powers.

gap between the optimal amplifier lengths of each design is expected due to the vastly different erbium concentrations in each design. However, the low TeO_2 confinement factor in Design #1 lessens the rapid absorption we would expect from an amplifier with a high erbium concentration. This is evident by a more gradual decline of optimal amplifier length as the erbium concentration is increased in Figure 3.21 for Design #1.

Once the model is run again with the new optimal amplifier lengths calculated above, the results similar to those in Figures 3.16, 3.17 and 3.18 are redrawn and shown in Figures 3.22, 3.23 and 3.24, respectively. Now with the amplifier lengths optimized, the saturation of the signal power is observed for each design as shown in Figure 3.23. This is caused by degradation of the pump power until it falls below the threshold pump power, calculated in Eq. (2.32) and depicted in Figure 3.22 as a black dotted line. Once this occurs, the signal power encounters a maxima as it goes from increasing to decreasing. Population inversion is also lost near this position as the upper state population falls below 0.5 in Figure 3.24. This turning point occurs much sooner along the z propagation

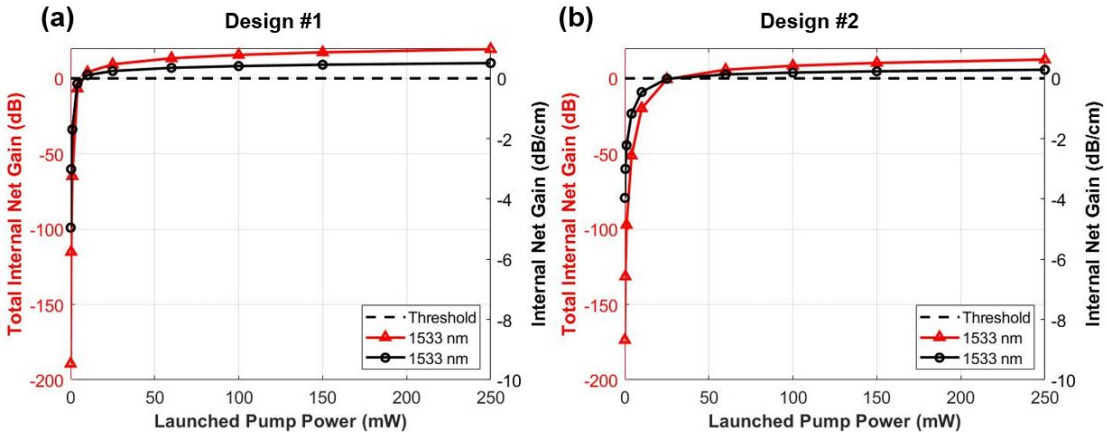

FIGURE 3.25: Launched pump power vs. total internal net gain and internal net gain per unit length for (a) Design #1 and (b) Design #2 with optimal amplifier lengths and at 1533 nm wavelength.

axis in Design #1 than in Design #2 due to the larger overall Er^{3+} dopant concentration in the system.

Using the results from Figure 3.23, the total internal net gain and internal net gain per unit lengths results may also be replotted again for the corresponding optimal amplifier lengths. This is shown in Figure 3.25 against various launched pump powers for 1533 nm wavelength. From this figure, total internal net gain values of 19.37 dB and 12.42 dB and internal net gain per unit length values of 0.51 dB/cm and 0.28 dB/cm are calculated for Design #1 and Design #2, respectively. Figure 3.26 shows total internal net gain and internal net gain per unit length plotted against wavelength for various launched pump powers. The total internal net gain maintains 1-dB bandwidths of 37 nm (1528 - 1565 nm) and 33 nm (1529 - 1562 nm) for Design #1 and Design #2, respectively, stretching across the entire C-band. The total internal net gain here is significantly greater than those reported for the fabricated lengths for both designs as light-interaction occurs over a greater length. However, the internal net gain per unit length is smaller due to the significantly longer length. This would reduce much further if losses due to active processes were also accounted for. Thus, from this analysis, we can conclude that longer waveguides are able to achieve much higher internal gain while shorter waveguides are

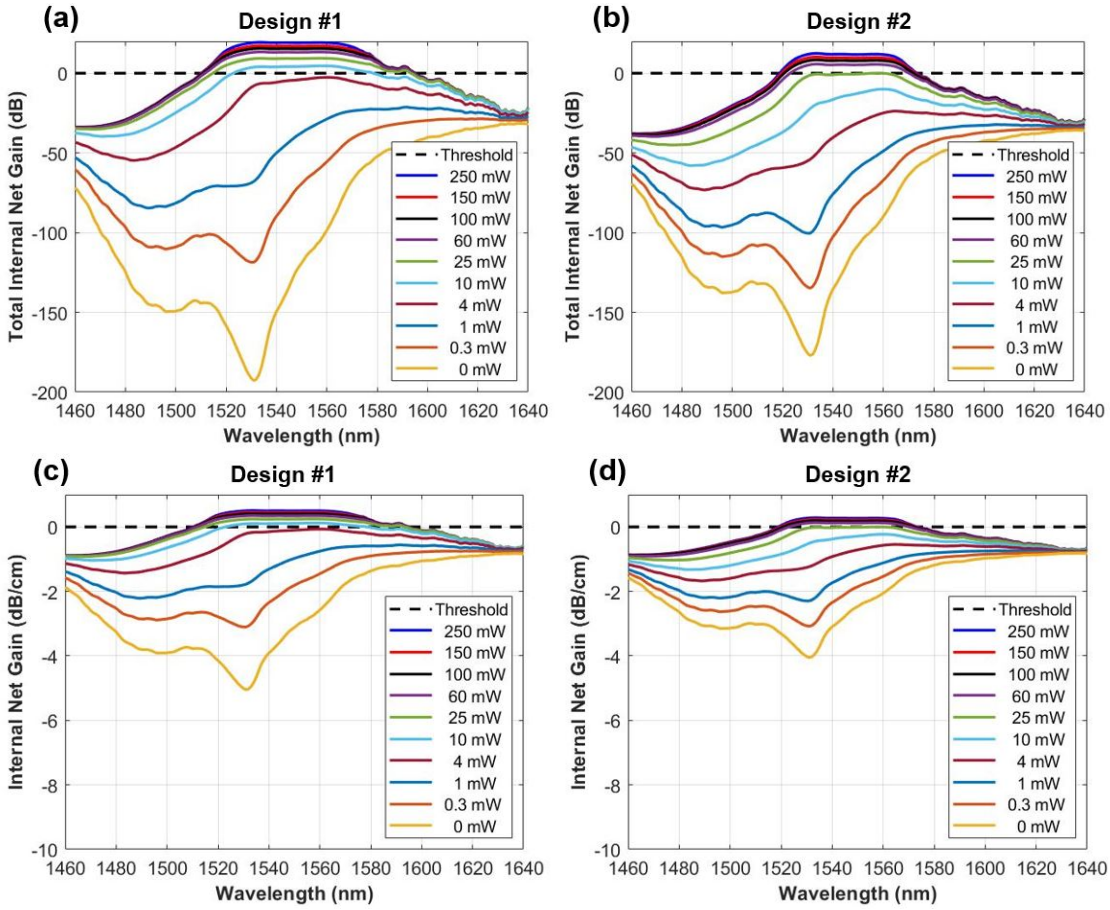

FIGURE 3.26: Wavelength vs. (a-b) total internal net gain and (c-d) internal net gain per unit length for (a,c) Design #1 and (b,d) Design #2 with optimal amplifier lengths and at various launched pump powers.

better suited for applications that require higher internal net gain per unit length. All parameters and gain results (for both non-optimal and optimal lengths) from our model are summarized in Table 3.6. The validation model parameters and results from [19] listed in Table 3.4 are also relisted in Table 3.6 for direct comparison.

TABLE 3.6: TeO_2:Er^{3+} amplifier model summary table. Dual values under [This work]* column correspond to [Design #1, Design #2].

Parameter Variables	Symbol	[19]	[This work]*	Source*
Pump Wavelength (nm)	λ_p	1475	1477	[This work]
Signal Wavelength (nm)	λ_s	1535	1533	[This work]
Mode effective area, pump (μm^2)	$A_{\text{eff,p}}$	5.24	[0.15, 0.33]	[This work]
Mode effective area, signal (μm^2)	$A_{\text{eff,s}}$	5.32	[0.17, 0.37]	[This work]
TeO_2 confinement factor, pump (%)	Γ_p	90	[14.7, 61.4]	[This work]
TeO_2 confinement factor, signal (%)	Γ_s	90	[15.3, 62.4]	[This work]
Abs. cross section, pump (10^{-21} cm^2)	$\sigma_p^{(a)}$	3.54	3.78	[27]
Abs. cross section, signal (10^{-21} cm^2)	$\sigma_s^{(a)}$	6.49	7.05	[27]
Em. cross section, pump (10^{-21} cm^2)	$\sigma_p^{(e)}$	1.03	1.18	[45]
Em. cross section, signal (10^{-21} cm^2)	$\sigma_s^{(e)}$	6.91	7.19	[45]
Fluorescent lifetime (ms)	τ	1.3	2.6	[57]
Background loss, pump (dB/cm)	α_p	0.6	0.6	[19]
Background loss, signal (dB/cm)	α_p	0.4	0.4	[18]
Parameters of Interest	//	//	//	//
Amplifier length (cm)	L	5	[0.93, 1.7]	[This work]
Er concentration (10^{20} cm^{-3})	N	2.2	[10.0, 1.68]	[This work]
Launched power, signal (μW)	$P_{s,0}$	10	1	[This work]
Launched power, pump (mW)	$P_{p,0}$	250	250	[This work]
Results Pt.1	//	//	//	//
Total internal net gain (dB)	G	13.87	[1.61,1.58]	[This work]
Internal net gain (dB/cm)	γ	2.77	[1.73,0.93]	[This work]
Results Pt.2	//	//	//	//
Optimal amplifier length (cm)	L_{opt}	N/A	[38.22,43.75]	[This work]
Total internal net gain (dB)	G	N/A	[19.37,12.42]	[This work]
Internal net gain (dB/cm)	γ	N/A	[0.51,0.28]	[This work]

One significant difference between this work and the others we have compared to [19, 41, 57] is the presence of the silicon waveguide. SOI waveguides are notorious for high waveguide losses, primarily due to interface induced scattering, which can result in losses ranging from 0.8-36 dB/cm for waveguides with 220 nm SOI thickness [59].

The background loss used in our model is 0.6 dB/cm and 0.4 dB/cm for the pump and signal light, respectively, and is taken from [19, 20], which only contains TeO_2 in a rib waveguide structure. Although the incorporation of TeO_2 as a cladding material will significantly decrease the scattering loss in comparison to silicon-based devices using conventional lower index claddings, such as SiO_2, we expect the total background loss in our waveguides to be much higher than the values < 1 dB/cm that we currently use in our model. However, this loss has not yet been quantified.

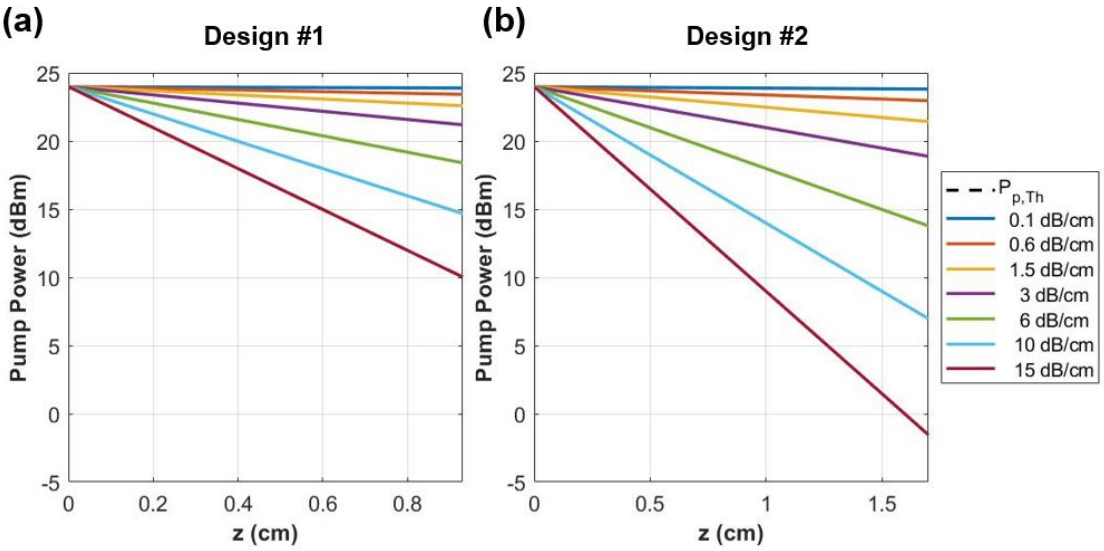

FIGURE 3.27: Position z along the amplifier length vs. pump power for (a) Design #1 and (b) Design #2 with various background losses at 1533 nm wavelength.

We adjust the model once again to simulate various background losses in our fabricated waveguide structures and provide an estimate of what losses we should expect upon measuring them. Figures 3.27 and 3.28 show the simulated pump power and signal power, respectively, as the light travels along the length of the amplifiers described in Table 3.5. Figure 3.28, in particular, shows the magnitude of the effect the varying background loss has on the final output signal power. The total internal net gain and internal net gain per unit length of these simulations are shown in Figure 3.29 as a function of total background loss for both designs. As expected, the gain decreases

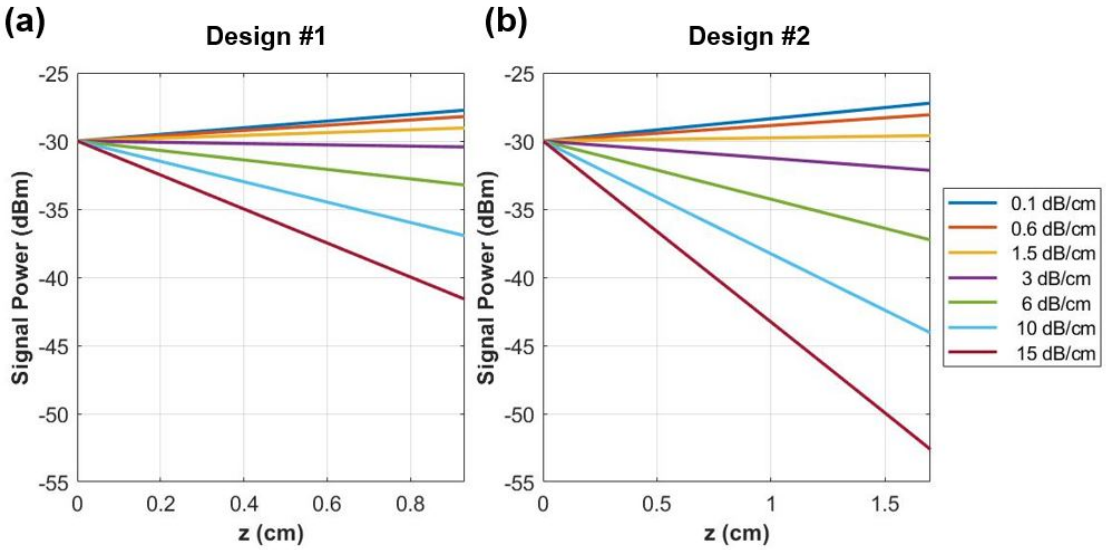

FIGURE 3.28: Position z along the amplifier length vs. signal power for (a) Design #1 and (b) Design #2 with various background losses at 1533 nm wavelength.

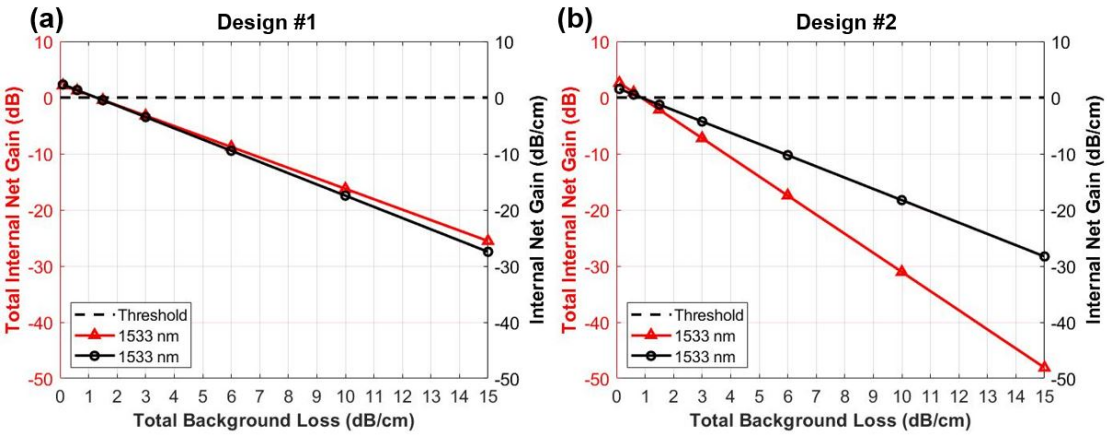

FIGURE 3.29: Total background loss vs. total internal net gain and internal net gain per unit length for the fabricated waveguide amplifiers for (a) Design #1 and (b) Design #2 described in Table 3.5 with 250 mW launched pump power and at 1533 nm wavelength.

drastically with increased background loss. Using the linear relationship depicted by the line in each plot, the total internal net gain threshold, in which no gain is achieved in the device (0 dB), is crossed at 1.3 and 0.8 dB/cm total background loss for Design #1 and Design #2, respectively. We use these values as a goal for what background loss we hope to experimentally measure in order to achieve positive gain in our amplifier. The measurement results will be discussed in the next chapter.

Chapter 4

Results

In this chapter, we discuss the experimental results of the fabricated SOI wire waveguide structures coated in both undoped and erbium-doped tellurium oxide. First, the passive results are given, including waveguide propagation and coupling losses for all samples that are determined using the cutback method and linear regression fits of measured transmission data from our samples at a 1640 nm wavelength. Erbium absorption characteristics are also considered and calculated during this stage. Next, we look at the signal enhancement measurements and use them in addition to the waveguide loss measurements to determine the achievable internal net gain in our waveguide structures. Maximum signal enhancements of 1.43 dB and 3.84 dB are reported for our high-confinement waveguides (HCWGs) and high-overlap waveguides (HOWGs), respectively. Discussion of the results as well as future steps for improvement and other design ideas are presented as a conclusion to the chapter.

4.1 Passive waveguide measurements and results

Passive loss measurements are performed to characterize the waveguide loss in every waveguide on our sample chips. The cutback method has been used extensively over the years for various loss measurements in optical waveguides [59, 60]. We measure

the experimental transmission spectra of our waveguides with varying length and then apply the cutback method by performing a linear regression fit of the data at a specific wavelength to extract the waveguide propagation and coupling losses.

4.1.1 Passive measurement setup

We measured the optical propagation loss of our fabricated SOI wire waveguide structures using a fiber edge coupling setup that is depicted in Figure 4.1. A tunable 1550 nm laser source was coupled into the chip via lensed fibers with a 2.5 ± 0.5 μm mode field diameter. The polarization of the incident light was controlled using a paddle-based polarization controller from Thorlabs prior to the fiber input into the chip. Both input and output fibers are mounted onto xyz alignment stages to enable simple fiber-chip edge coupling. The transmitted signal at the output was measured using an InGaAs photodetector. A single measurement is performed using a GPIB connection between the tunable laser, photodetector and a PC laptop. The laptop runs a Matlab script that creates a GPIB object to communicate with the tunable laser and sweeps the input wavelength between 1510 and 1640 nm. The transmission data obtained by the photodetector is then stored into a readable data file on the laptop for analysis.

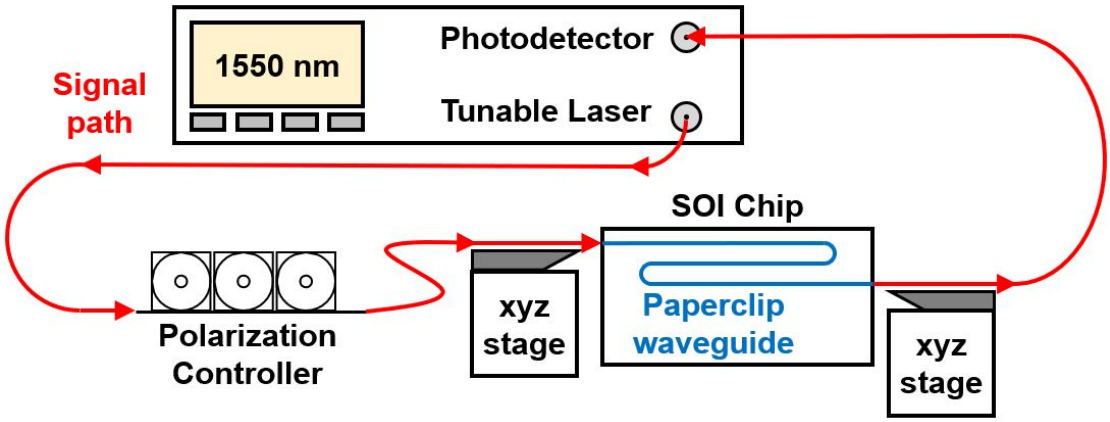

FIGURE 4.1: Passive experimental setup used for waveguide loss measurements.

4.1.2 Waveguide propagation and coupling loss results

Following experimental measurements, the data is gathered and analyzed thoroughly. For clarity, we number our measured sample chips and detail them in Table 4.1. Figure 4.2 shows the mode profiles simulated using RSoft FemSIM for each of these waveguides as well.

TABLE 4.1: Summary of sample chip details, waveguide simulation results and waveguide loss measurement results. All results correspond to $\lambda = 1640$ nm.

Chip #	1	2	3	4
Foundry	AMF	AMF	ANT	ANT
Chip name	C13	C48	B357	B93
Cladding material	TeO_2	TeO_2:Er^{3+}	TeO_2	TeO_2:Er^{3+}
TeO_2 thickness (nm)	101±5	121±5	225±5	330±5
TeO_2 film index (from VASE)	2.04±0.01	1.99±0.02	2.07±0.01	2.07±0.02
Er concentration (10^{20} cm^{-3})	N/A	10.0±0.1	N/A	1.68±0.02
Waveguide width (nm)	450	450	200	200
Waveguide facet width (nm)	180	180	200	200
RSoft simulation results	//	//	//	//
Waveguide mode effective index	2.33±0.01	2.32±0.01	1.80±0.01	1.90±0.01
Waveguide loss (dB/cm)	0.34±0.01	0.34±0.01	0.08±0.01	0.06±0.01
Facet mode effective index	1.47±0.01	1.50±0.01	1.80±0.01	1.90±0.01
Measurement results	//	//	//	//
Propagation loss (dB/cm)	3.9±0.4	4.4±0.2	14.6±1.4	11.6±8.0
Coupling loss (dB/facet)	1.6±0.2	1.7±0.1	8.4±1.0	11.5±5.5

We first adjust the transmission spectra of each measured waveguide to compensate for the input signal power and any system losses, such as fiber-to-fiber insertion loss, thus isolating the waveguide losses. Transmission spectra of waveguides with equivalent geometry but varying length are plotted against each other, as seen in Figure 4.3. A Savitsky-Golay smoothing filter is lightly applied to each spectrum to reduce noise and improve clarity of the data. Analysis of noise and local features in the data due to Fabry-Perot resonances are not discussed in this thesis.

From the plots in Figure 4.3, loss is then characterized by extracting the insertion loss of each waveguide at 1640 nm wavelength, which is outside the range of erbium's

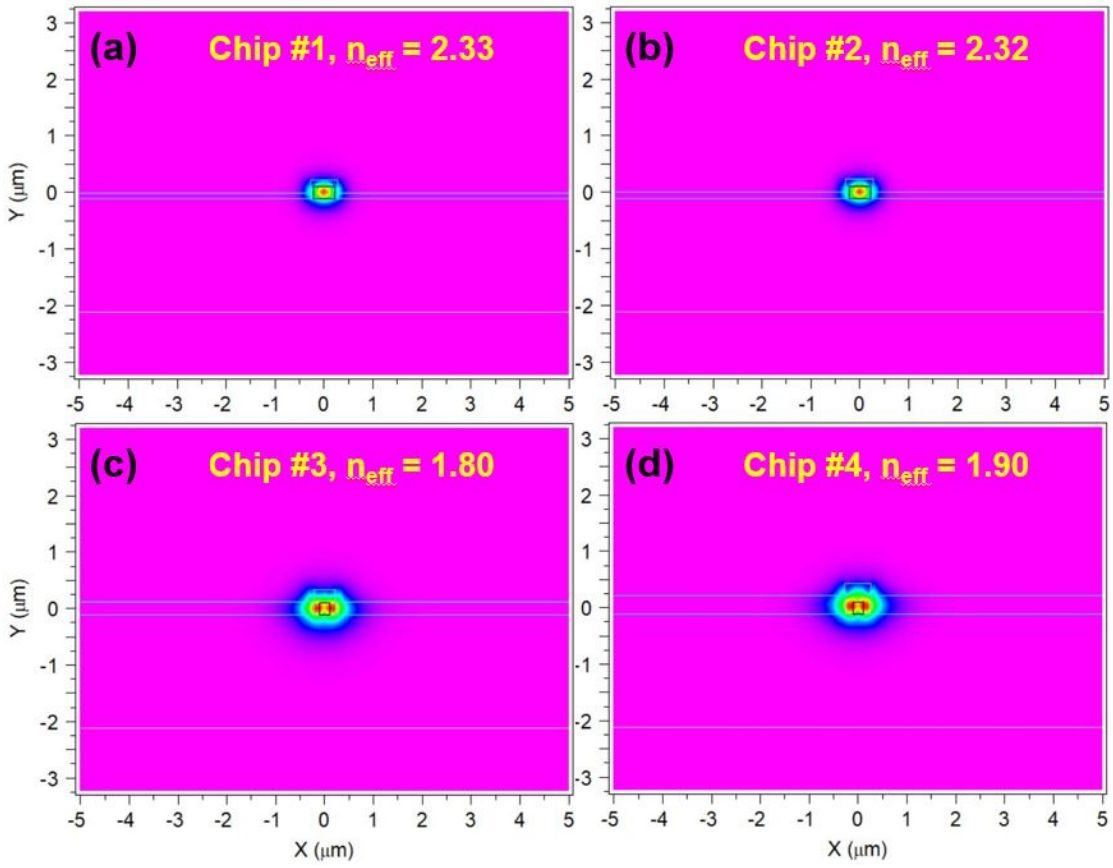

FIGURE 4.2: Simulated mode profiles of SOI wire waveguides on (a) Chip #1, (b) Chip #2, (c) Chip #3, and (d) Chip #4 described in Table 4.1.

absorption spectrum. Furthermore, 1640 nm wavelength exhibits the best transmission across each spectrum and is the least susceptible to other system losses that may have been unaccounted for. The insertion loss at 1640 nm wavelength for each waveguide is plotted against their respective lengths. A linear regression fit is then taken for each series of waveguides on each chip and is plotted against their respective data series as seen in Figure 4.4. The waveguide propagation and coupling losses are then estimated as the absolute of the slope and y-intercept of the linear regression fit for each data series, respectively. We characterize the coupling loss as fiber-chip coupling loss at one facet (in units of dB/facet) and therefore divide the extracted y-intercept value by 2 because our experimental setup involves fiber-chip coupling at 2 locations. The

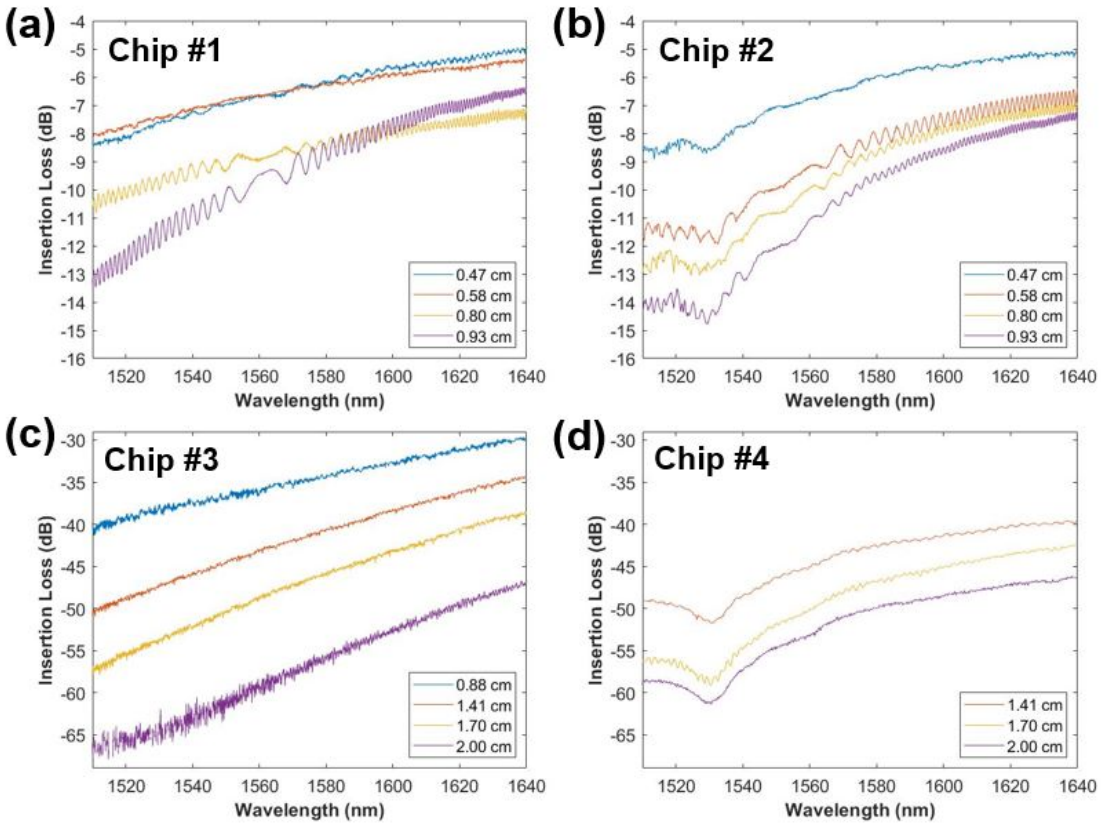

FIGURE 4.3: Measured transmission spectra of SOI wire waveguides with varying lengths on (a) Chip #1, (b) Chip #2, (c) Chip #3, and (d) Chip #4 described in Table 4.1.

waveguide propagation and coupling loss results are highlighted at the bottom of Table 4.1 under the chip details. The simulated waveguide loss is calculated using Eq. (3.1) and the imaginary refractive index results from the RSoft FemSIM simulation of each respective waveguide structure.

For the high-confinement waveguides (HCWGs), the propagation and coupling losses are 3.9±0.4 dB/cm and 1.6±0.2 dB/facet for the undoped sample (Chip #1), and 4.4±0.2 dB/cm and 1.7±0.1 dB/facet for the Er^{3+}-doped sample (Chip #2), respectively. The high confinement of these waveguides reduces loss caused by the interface induced scattering, which is the primary loss mechanism in optical SOI waveguides. The propagation loss is comparable to and, in some cases, better than the 1550 nm losses

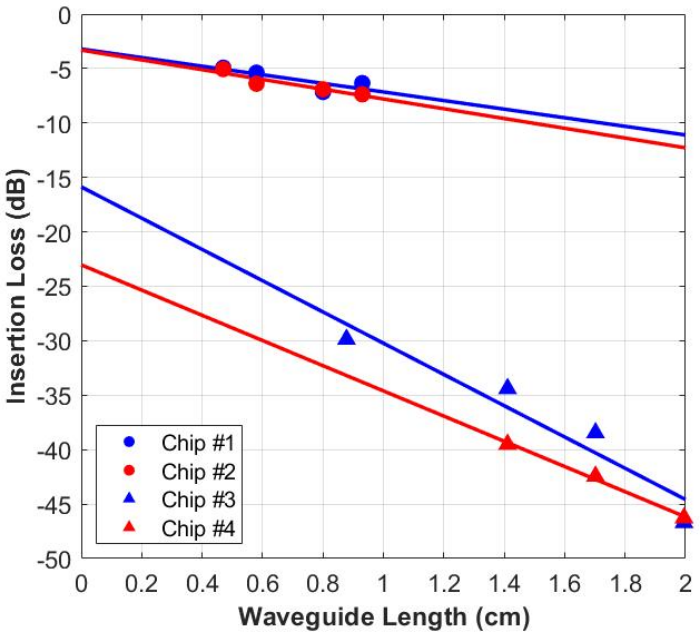

FIGURE 4.4: Waveguide length vs. insertion loss at 1640 nm wavelength for SOI wire waveguides from all chips described in Table 4.1.

reported for many other SOI waveguides with similar geometry utilizing air or SiO_2 as a top cladding [59]. The coupling loss is also relatively small due to the smaller waveguide width at the edge facet, thus enabling higher modal expansion and better modal overlap with the fiber mode. There is a high confidence level of these results with uncertainties of <0.5 dB/cm for propagation loss and <0.3 dB/facet for coupling loss. Both propagation loss and coupling loss for the undoped and Er^{3+}-doped HCWG series are very similar and agree within their small uncertainties, primarily due to their comparable waveguide and cladding geometry. The undoped sample has a slightly higher TeO_2 refractive index (2.04±0.01 for undoped vs. 1.99±0.02 for Er^{3+}-doped), while the Er^{3+}-doped sample has a slightly thicker TeO_2 film layer (101±5 nm for undoped vs. 121±5 nm for Er^{3+}-doped). These balance out to enable a similar mode effective index ($n_{eff} \approx 2.32$) and area between each waveguide sample. It is noted that the similarities in the measured results here are for 1640 nm wavelength. The transmission at 1533 nm wavelength will

be much more different for the two sample chips due to the presence of erbium and its strong absorptive properties at this wavelength. This will be discussed in the next section.

For the HOWGs, the propagation and coupling losses are 14.6±1.4 dB/cm and 8.4±1.0 dB/facet for the undoped sample (Chip #3), and 11.6±8.0 dB/cm and 6.0±5.5 dB/facet for the Er^{3+}-doped sample (Chip #4), respectively. The large uncertainties for both loss values of Chip #4 are due to the lack of a data point for the 0.88 cm length waveguide, as this waveguide was damaged prior to measurement and outputted skewed results. Unlike the relationship between the undoped and Er^{3+}-doped HCWGs, the undoped and Er^{3+}-doped HOWGs display very different propagation and coupling losses that only agree with each other due to the large uncertainties of Chip #4. This could be due to the large difference in TeO_2 cladding thickness, with 225 nm thickness in the undoped sample and 330 nm in the Er^{3+}-doped sample, resulting in an index difference of 0.1, which is much larger than the 0.01 index difference of the HCWGs.

Both propagation and coupling losses for the HOWGs are much larger than those reported from the HCWGs. The coupling loss can be explained using the effective index results of the facet modes highlighted under RSoft simulation results in Table 4.1. Coupling efficiency is increased as the effective index contrast between the optical fiber mode ($n \sim 1.44$) and the waveguide facet mode are reduced. For the HCWGs, the facet mode effective indices are 1.47±0.01 and 1.50±0.01, which are very close to the fiber mode effective index $\sim$ 1.44 and output coupling losses of 1.6±0.2 and 1.7±0.1 for Chip #1 and Chip #2, respectively. On the other hand, the facet mode effective indices for the HOWGs are 1.80±0.01 and 1.90±0.01 for Chip #3 and Chip #4, respectively. Thus, the high index contrast ($\Delta \sim 0.4$) results in high coupling losses of 8.4±1.0 and 11.5±5.5 for Chip #3 and Chip #4, respectively. Higher coupling loss is a natural consequence of incorporating TeO_2 as a top cladding since its high index widens the index contrast

between the fiber and the chip. Tapering the waveguide width at the edge facet, as was done for the HCWG designs, is one simple solution to reducing the coupling loss. However, this was not implemented on the HOWG designs and could have signficantly reduced the coupling loss, especially with the smaller minimum feature size available on the ANT platform ($\sim$ 60 nm). Other solutions to reducing coupling loss are still being explored and are outside the scope of this thesis.

As for the high propagation losses in the HOWGs, there are many possible explanations. Bend loss can be ruled out as a catalyst for higher waveguide loss per the discussion given in Section 3.2.1 and the results depicted in Figure 3.12 showing < 0.2 dB/cm radiation loss from bent waveguides with over 0.2 μm TeO_2 cladding thickness and 50 μm bend radius. It may be suggested that the TeO_2 itself played a role in introducing additional loss to the system, given that the TeO_2 thickness is much higher on the chips with the HOWG designs. However, other works utilizing the same deposition system have determined background film propagation losses of $\sim$ 0.1 dB/cm for 0.2-0.4 μm-thick undoped TeO_2 films [17] and 0.4$\pm$0.3 dB/cm for a 0.34 μm-thick TeO_2:Er^{3+} film [27]. Furthermore, higher TeO_2 thicknesses at this magnitude actually reduce waveguide loss, as stated by the simulated waveguide loss results stated in Table 4.1. Instead, the most plausible explanation points to interface induced scattering loss. Though TeO_2 cladding on silicon waveguides significantly reduces the loss factor in comparison to lower index cladding, interface induced scattering still plays a major role in the loss. Looking at the mode profiles of the measured HOWG waveguides in Figure 4.2(c-d), the optical intensity strength is noticeably focused more on the Si-TeO_2 interface, as indicated by red. On the other hand, the optical intensity of the HCWGs is strongest at the center of the waveguide core, as indicated in Figure 4.2(a-b). Though this represents normalized intensity, it implies that the HOWGs experience much more interaction with the waveguide sidewalls than the HCWGs do, and therefore suffer from higher interface induced scattering losses. Quantification of this loss is complex and

outside the scope of this thesis. However, it is noted that more consideration of these mode profiles and the spread of the optical intensity should be taken when determining the optimal waveguide geometry.

The lithographic techniques used by each foundry may also have an impact on the loss. AMF advertises waveguide losses < 1.5 dB/cm on their SOI platform [46], while ANT reports 1.5 dB/cm and 3.8 dB/cm loss for their straight and curved silicon waveguides, respectively [47]. Overall, this suggestion, and the relationship of these values to our work, is speculative. However, in future design comparisons, it is best to compare and characterize designs that use the same fabrication techniques and services.

4.1.3 Peak erbium absorption measurements

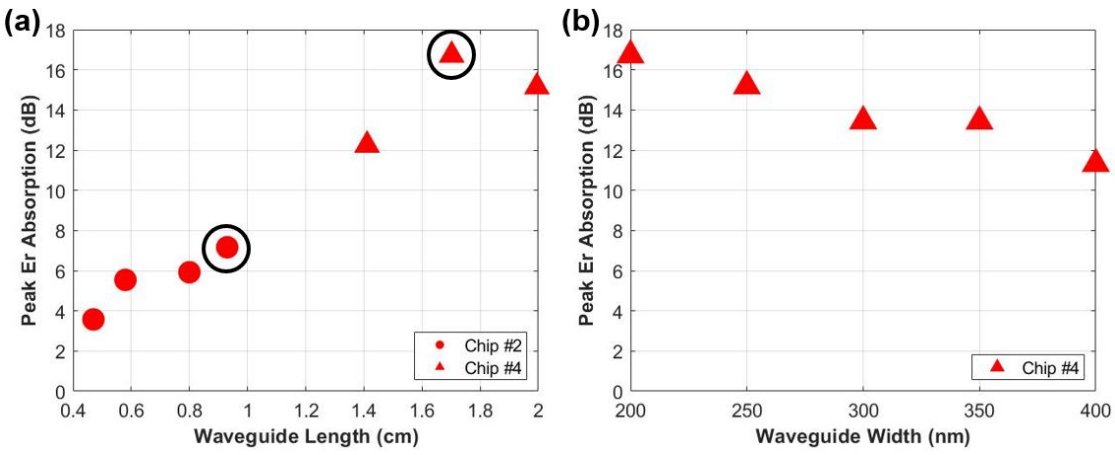

FIGURE 4.5: Peak erbium absorption measurement results with respect to (a) waveguide length and (b) waveguide width. Circular and triangular data points correspond to waveguides on Chip #2 and #4 described in Table 4.1, respectively. Black circles indicate waveguides used for active measurements described in Section 4.2.2. Waveguides in (b) have 1.70 cm length.

The peak erbium absorption is measured as the difference in insertion loss between 1530 nm and 1640 nm wavelengths. Erbium in our TeO_2 films introduces loss to specific wavelengths dependent on their location in its absorption spectrum [27]. 1530 nm light

is at the heart of the erbium absorption spectrum and will therefore carry the highest absorption losses. Meanwhile, 1640 nm is outside of the spectrum and losses due to erbium interactions are almost considered negligible. The peak erbium absorption measurements are plotted for a variety of waveguides covered in our erbium-doped films in Figure 4.5. Longer waveguides allow longer interaction time between the light and the gain material containing the erbium that absorbs the light. Furthermore, thinner waveguides have a larger mode size and higher modal overlap with the gain material. Therefore, erbium absorption will increase in thinner and longer waveguides. Figure 4.5 supports this statement as waveguides with smaller width and higher length exhibit the highest peak erbium absorption measurements. We take note of the results for the two waveguides surrounded by black circles as these waveguides will be measured and used to characterize gain in the following sections. The peak erbium absorption is 7.2 dB and 16.7 dB for these waveguides on Chip #2 and Chip #4, respectively. These values will substitute as the absorption loss due to active processes, which is equivalent to $\alpha_{act}(\lambda)$ from Eq. (2.18). Further analysis may be done for characterization of the Er^{3+}-doped films, but this is not within the realm of this thesis.

4.2 Active waveguide measurements and results

Following passive loss measurements, active measurements are performed to characterize the gain in our TeO_2:Er^{3+}-coated SOI waveguides.

4.2.1 Active measurement setup

The experimental setup changes slightly for gain measurements performed on our waveguide structures to include the pump source, as depicted in Figure 4.6. Wavelength division multiplexing (WDM) couplers are implemented to couple the signal and pump sources onto the same fiber for simultaneous entrance onto the chip and to de-couple the sources after leaving the chip to eliminate pump source interference during detection

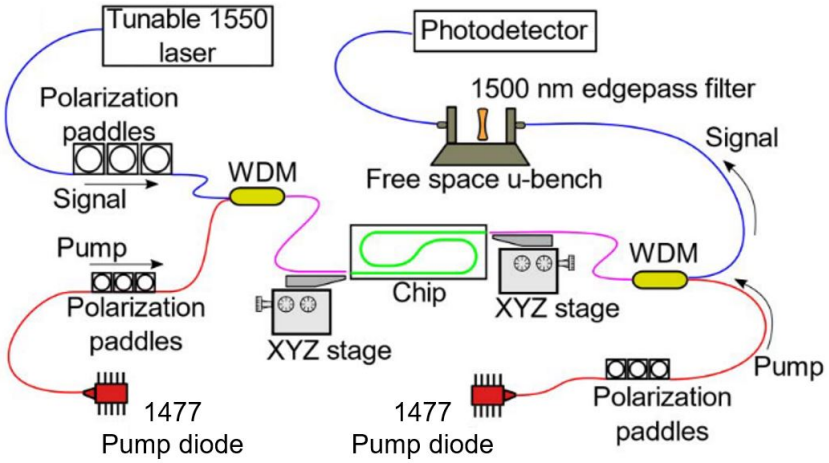

FIGURE 4.6: Active experimental setup used for signal enhancement measurements. Adapted from [27].

of the amplified signal light. The pump source is generated and received by separate 1477 nm high-power laser diodes, which each have a fixed wavelength but adjustable pump powers. A free space edgepass filter is also utilized to help isolate any additional unwanted pump light from the detected signal.

4.2.2 Signal enhancement and gain results

Characterization of gain in our waveguide amplifiers begins by analyzing the signal enhancement. This is an experimental quantity measured as:

$$SE(\lambda) = 10 \cdot \log_{10}(I_p(\lambda)/I_u(\lambda)), \tag{4.1}$$

where $I_p(\lambda)$ and $I_u(\lambda)$ are the measured intensities of the signal light with the pump on and off, respectively [61]. From this result, the measured total internal net gain (dB) and internal net gain per unit length (dB/cm) may then be calculated:

$$G(\lambda) = SE(\lambda) - \alpha_{Total}(\lambda), \tag{4.2}$$

$$\gamma(\lambda) = G/L, \tag{4.3}$$

where $\alpha_{Total}(\lambda)$ is total measured losses at wavelength λ (dB/cm) and L is the total amplifier length (cm). $\alpha_{Total}(\lambda)$ has a similar meaning to its mathematical definition in Eq. (2.18). Experimentally, it is the sum of the measured propagation loss and Er absorption loss, which were each determined for both waveguide structures in Sections 4.1.2 and 4.1.3, respectively. Table 4.2 restates the details of the Er^{3+}-doped chips (#2 and #4) and their waveguide loss results discussed in Section 4.1.2, and highlights the signal enhancement measurements and gain results described by the equations above.

TABLE 4.2: Summary of signal enhancement measurements and gain results.

Chip # (see Table 4.1)	2	4
Foundry / chip name	AMF / C48	ANT / B93
TeO_2:Er^{3+} thickness (nm)	121±5	330±5
TeO_2:Er^{3+} film index (from VASE)	1.99±0.02	2.07±0.02
Er concentration (10^{20} cm^{-3})	10.0±0.1	1.68±0.02
Waveguide width (nm)	450	200
Waveguide facet width (nm)	180	200
Waveguide length (cm)	0.93 (L6)	1.70 (L2)
Passive results	//	//
Propagation loss (dB/cm)	4.4±0.2	11.6±8.0
Coupling loss (dB/facet)	1.7±0.1	11.5±5.5
Peak Er absorption (dB)	7.2	16.7
Active results	//	//
Peak signal wavelength (nm)	1533	1533
Maximum pump power (mW)	83.7	377.0
Peak signal enhancement (dB)	1.43	3.84
Total internal net gain (dB)	-9.86	-32.58
Internal net gain (dB/cm)	-10.60	-19.16

First, we look at the results for the HCWGs from Chip #2, which are depicted in Figure 4.7. Due to the limited bandwidth of the WDM couplers, we are only able to measure gain within a small window of the C-band (1525–1545 nm). The figure displays a nice curve as the pump power increases. Unlike the simulated gain curve from the

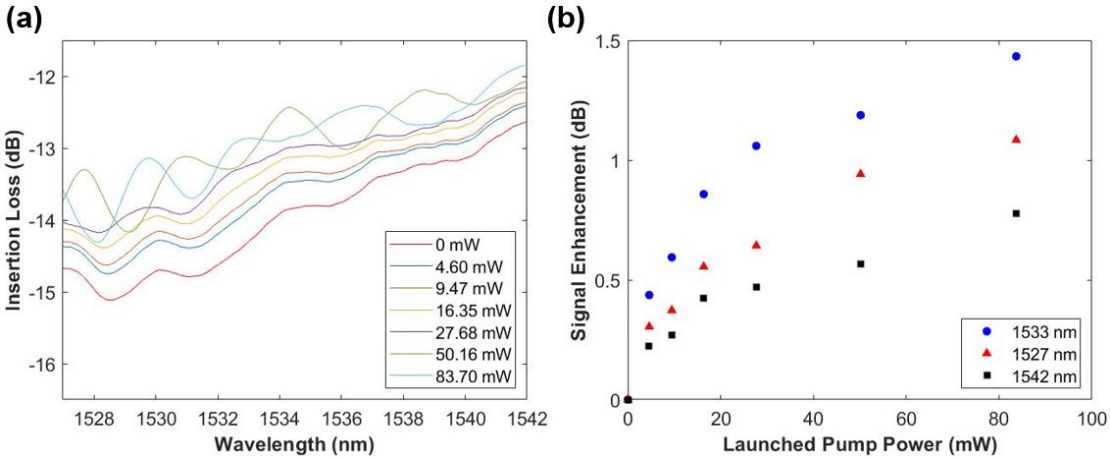

FIGURE 4.7: (a) Measured transmission spectra with various launched pump powers and (b) signal enhancement results for various launched pump powers for the high-confinement waveguide on Chip #2 described in Table 4.2.

amplifier model in Figure 3.19, the signal enhancement does not saturate, which could be due to losses present in the experimental measurements that were not considered in the model. We expect to have lower signal enhancement results for these waveguides compared to the HOWGs due to the limited overlap with the gain material and the shorter waveguide length. Coupling stability is difficult to manage above 50 mW pump power due to the high confinement, so we are only able to utilize pump powers up to 100 mW. The maximum measured signal enhancement of 1.43 dB is achieved at a 1533 nm peak wavelength with a launched pump power of 83.7 mW. While signal enhancement is restricted by the very thin layer of TeO_2:Er^{3+} (t_{clad} = 121 nm) and the small waveguide length (0.93 cm), the high erbium concentration (10^{21} cm^{-3}) significantly helps to increase the achievable signal enhancement. The reported total internal net gain and internal net gain per unit length are -9.86 dB and -10.60 dB/cm for this waveguide, respectively. Unfortunately, the negative net gain concludes that the background losses overwhelm the signal enhancement and signal gain is not achieved in these waveguides.

Next, we analyze the results for the HOWGs from Chip #4, shown in Figure 4.8.

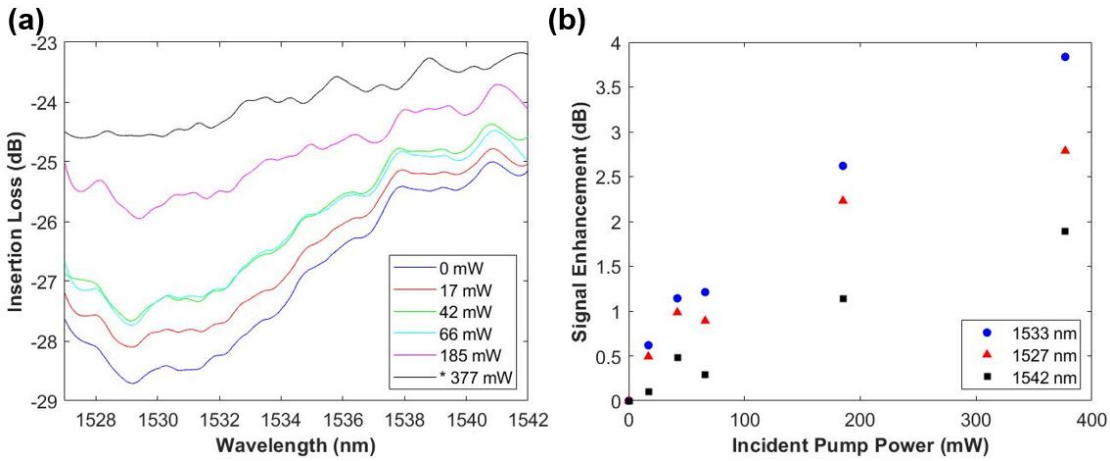

FIGURE 4.8: (a) Measured transmission spectra with various launched pump powers and (b) signal enhancement results for various launched pump powers for the high-overlap waveguide on Chip #4 described in Table 4.2.

These waveguides also display a nice trend along with a much higher signal enhancement than the HCWGs, as expected. Similar to the HCWGs, the gain curve appears to be more linear, indicating that the gain saturation regime has not yet been reached. Therefore, higher signal enhancement may be possible with increased launched pump power. The maximum measured signal enhancement of 3.84 dB is achieved at a 1533 nm peak wavelength with an incident pump power of 377.0 mW. The longer waveguide length and higher maximum pump power enable realization of a higher signal enhancement. The latter is achieved via double pumping into both ends of the waveguide through both input and output fibers. The reported total internal net gain and internal net gain per unit length are -32.58 dB and -19.16 dB/cm for this waveguide, respectively. Like the HCWGs, the negative gain indicates that the losses outweigh the signal enhancement. These gain results are much lower than the HCWGs, which is subject to the longer waveguide length increasing the Er^{3+} absorption loss and the higher propagation loss found from unpumped waveguide measurements. On the bright side, green light emission is observed in Figure 4.9 from this waveguide structure.

A full summary and discussion of the results from Table 4.2 is provided next. The

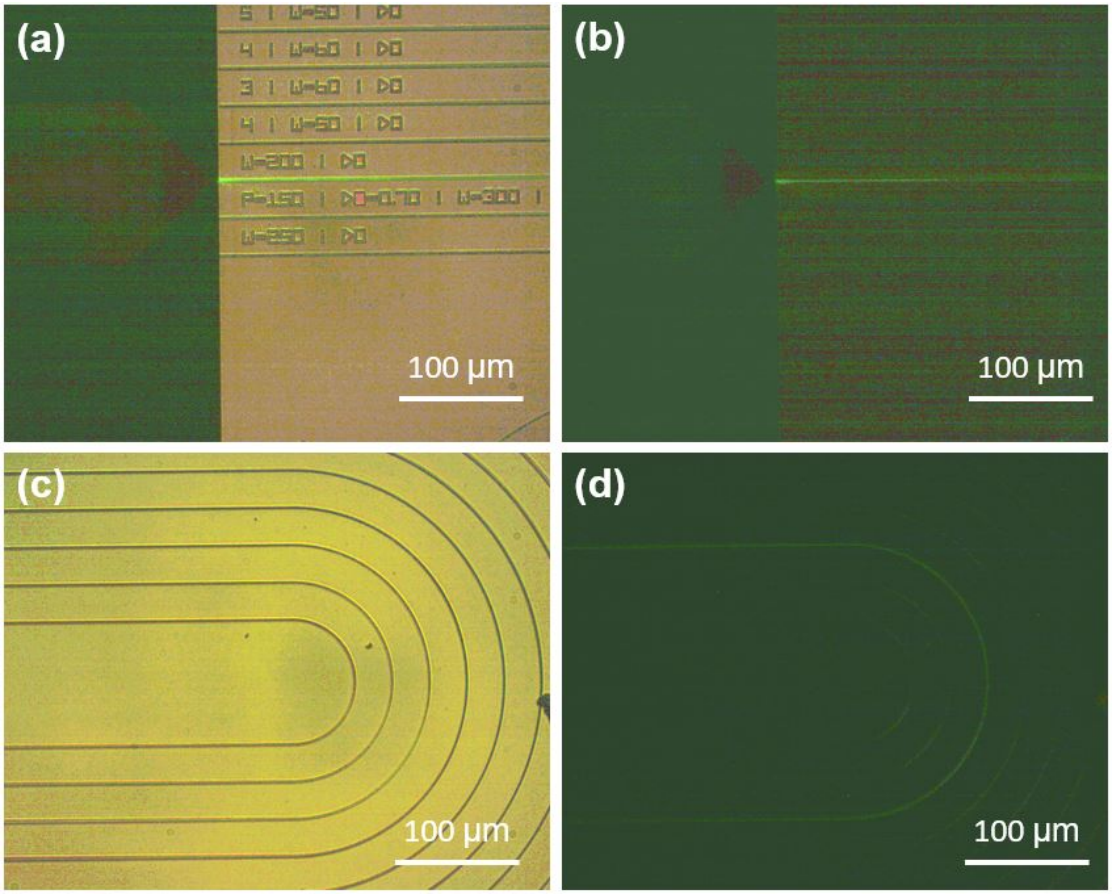

FIGURE 4.9: Green light emission in one of our high-overlap waveguides with 200 nm width and 1.7 cm length at the (a-b) edge facet and (c-d) waveguide bend. (a) and (c) include backlighting to show the structures, while (b) and (d) exclude backlighting to focus on the emitted green light.

measured signal enhancements are 1.43 dB and 3.84 dB for the HCWG from Chip #2 and HOWG from Chip #4, respectively. Using these results, as well as the measured waveguide propagation loss (4.4 dB/cm and 11.6 dB/cm for the HCWG and HOWG, respectively) and erbium absorption loss (7.2 dB and 16.7 dB for the HCWG and HOWG, respectively), the total internal net gain and internal net gain per unit length are calculated as -9.86 dB and -10.60 dB/cm for the HCWG, and -32.58 dB and -19.16 dB/cm for the HOWG, respectively.

Overall, the negative gain values indicate that both waveguides are too lossy to

amplify the signal light in this setup. Both gain curves in the signal enhancement results shown in Figures 4.7(b) and 4.8(b) do not exhibit gain saturation characteristics like those found in the amplifier model (Figure 3.19). This implies that higher signal enhancement may be possible if the launched pump power increases. At this stage, we cannot tell if this is accurate since coupling into the waveguide becomes difficult at such high pump powers.

The main factors affecting the overall net gain are the high measured losses. The analysis behind background loss given in Section 3.2.2 supports that overall loss reduction is the best way to achieve positive net gain in our SOI waveguide amplifiers. Figure 3.29 stated that positive gain was achieved only if the total background loss is lower than 1.3 and 0.8 dB/cm for the waveguides in Design #1 and Design #2, respectively. This corresponds to minimum total background losses of 1.21 dB and 1.36 dB for the measured HCWG and HOWG discussed here, respectively. From the passive results in Table 4.2, these reported measured losses are much higher than these background losses hoped for back in Chapter 3. These high losses were expected due to the implementation of Si waveguides. Many solutions may be implemented in future designs to reduce this loss and aim for better net gain.

As discussed in Section 4.1.2, the propagation losses range from moderate to high for SOI waveguides. The HOWGs are on the higher end of this due to the majority of the optical intensity overlapping the Si-TeO_2 sidewall interfaces, as seen in Figure 4.2(c-d), which will significantly raise loss caused by interface induced scattering–the prime culprit for waveguide loss. Re-optimizing the waveguide geometry, as well as the cladding geometry, with this modal behaviour in mind will definitely help to reduce the propagation loss, which in turn will significantly raise the overall internal net gain. There is also the loss caused by erbium absorption, which is very high at its peak even for short waveguide lengths (< 2 cm). From the results in Section 4.1.3, the erbium

absorption per unit length is averaged at 8.8±1.1 dB/cm. It is noted that this is the "peak" erbium absorption that represents the difference between insertion loss at 1640 nm and 1530 nm wavelengths of the same waveguide, which expresses the maximum value of erbium absorption loss possible in each sample. A better representation of the actual erbium absorption in each TeO_2 film would be realized by comparing these peak erbium absorption values between the undoped and Er^{3+}-doped chips. However, this was not performed in this study as large differences in cladding geometry and characteristics used on each sample chip would raise much uncertainty in the results.

To reduce erbium absorption, the amplifier model from Section 3.2.2 should be revisited. Simulations in this section, with results taken from Table 3.6, noted optimal amplifier lengths of 38.22 cm and 43.75 cm for Design #1 and Design #2, respectively, which are too long to include on the design spaces provided by the fabrication services we employed. Furthermore, the simulated internal net gain per unit length was higher for the fabricated waveguides with shorter lengths (1.73 dB/cm and 0.93 dB/cm for Design #1 and Design #2, respectively) in comparison to the equivalent waveguides with the calculated optimal lengths (0.51 dB/cm and 0.28 dB/cm for Design #1 and Design #2, respectively). This is because longer amplifier lengths increase the magnitude of the overall background loss and absorption loss, so shorter amplifier lengths (< 20 cm) will be more optimal in the end. Increasing the erbium concentration would reduce these optimal lengths, which is acceptable given their current excessive lengths. Another factor in the model that would increase the gain is the TeO_2 confinement factor. Though Design #1 has a high Er concentration of 10^{21} cm^{-3}, the gain was limited due to a low TeO_2 confinement factor of 15.3% for the 1533 nm wavelength signal. Increasing this would raise the overlap with the gain material, resulting in higher gain output, as well as shorter optimal amplfiier length.

We compare our signal enhancement results to those of [61], which uses a similar

waveguide structure but with erbium-doped alumina (Al_2O_3:Er^{3+}) cladding as the gain material. Here, the Si waveguide structure has 450 nm width (equivalent to our HCWGs) and 1.35 cm length, and the Al_2O_3:Er^{3+} cladding layer has a thickness of 1030 nm and erbium concentration of 2.70×10^{20} cm^{-3}. A 7.2 dB signal enhancement is achieved at a 1533 nm peak wavelength with a launched pump power of 53 mW. This is significantly higher than the results we show here and serves as a good comparison to test current and future designs against. In the next chapter, we will summarize our results again and conclude with suggestions for future work.

Chapter 5

Conclusion

5.1 Thesis overview

The objective of this project was to fabricate an erbium-doped waveguide amplifier (EDWA) on a silicon-based waveguide platform for integrated optics and to demonstrate the active capabilities of such a device. The purpose of developing such a device is to provide a viable solution to overcoming silicon as a poor light emitting material while still utilizing its popular infrastructure in silicon photonics (SiP). Thus, establishing positive gain would enable stimulated emission of light on-chip, unlocking potential for realization of a silicon-based photonic integrated circuit (PIC) capable of performing all optical functions necessary for data communications applications on a single microchip.

The amplifier model used to characterize the ideal gain performance in the device was based off previous models either created or adapted by the research group [41, 57]. Modifications were made to the model to account only for a two-level Er^{3+} energy system. This model was scripted in Matlab and the full code can be found in Appendix A. Based on the dimensions of the fabricated waveguide structures, total internal net gain values of 1.61 dB and 1.58 dB for the high-confinement waveguides (HCWGs) and high-overlap waveguides (HOWGs) were simulated, respectively, enabling 1.73 dB/cm

and 0.93 dB/cm internal net gain per unit length for 250 mW launched pump power and 1 μW launched signal power, as highlighted in Table 3.6.

The Synopsys RSoft software suite was used in the design phases of the project to characterize the optical mode field patterns within the waveguide structure. Through this process, optimal geometric waveguide parameters were calculated and applied on a design mask layout constructed in Mentor Graphics Pyxis. The mask layout was sent to silicon photonics foundries, Advanced Micro Foundry (AMF) and Applied Nanotools (ANT), for separate fabrication runs of the various waveguide structures. Tellurium oxide (TeO_2) deposition took place at McMaster University using the reactive magnetron sputtering system operated by the Centre for Emerging Device Technologies (CEDT) [62]. Highly qualified personnel from the research group carried out these deposition tasks and reported details regarding the quality of the deposited films back to the primary researcher.

The primary researcher then performed experimental measurements to characterize waveguide loss and gain from the device. Waveguide propagation losses of 4.4 dB/cm and 11.6 dB/cm, as well as fiber-chip coupling loss of 1.7 dB/facet and 11.5 dB/facet, were reported for the measured HCWGs and HOWGs, respectively. Final signal enhancement results of 1.43 dB and 3.84 dB were reported for the 0.93 cm-long HCWG and 1.70 cm-long HOWG, respectively. The high propagation losses outweigh the signal enhancements, resulting in negative internal net gain for both waveguide designs. These results do not match those of the amplifier model, though many parameters affecting the output are also different, including launched pump power and launched signal power. Furthermore, the model does not account for other processes, such as amplified spontaneous emission (ASE), that are parasitic to and potentially present in the experimental gain results. All the above results are highlighted in Table 4.2.

5.2 Future work

A direct comparison to a similar device utilizing Al_2O_3:Er^{3+} active cladding [61] reveals a significantly lower signal enhancement and gain yield in this work. Many steps may be taken to improve the performance of these devices:

- *Utilization of the same foundry for fabrication of all waveguides under review*: Employing different fabrication services makes direct comparison between the various waveguide structures difficult. Propagation losses provide small details into which foundry delivers higher quality waveguides that exhibit smaller loss primarily caused by interface induced scattering from sidewall interactions, which lithographic patterning techniques have a strong effect on. From these results, AMF is the better choice for these waveguides.

- *Optimization of and consistency in waveguide and cladding geometry*: The mode profiles in Figure 4.2 show how the position and strength of different areas of the waveguide mode relate to propagation loss. Furthermore, keeping the geometry between comparable sample chips and designs will allow the results to be more consistent and establish higher confidence in the final results.

- *Amplifier model re-optimization to balance erbium concentration and amplifier length*: The amplifier model claims that higher gain may be realized in both designs if the amplifier length is optimized to a particular erbium concentration. However, the outputted lengths for the current erbium concentrations outputs values that are unrealistic for fabrication. Optimizing this, as well as the above point, will allow a realistic erbium concentration and amplifier length, as well as good waveguide geometry, that may realize higher net gain in our amplifiers.

- *Design better fiber-chip edge couplers*: High coupling loss causes degradation of the signal at the entrance of the waveguide, which may leave nothing but noise level

outputs once the signal has travelled through the waveguide. Tapering the width of the waveguide at the chip edge increases the mode effective area, allowing higher overlap with the fiber mode.

Other silicon waveguide structures have been explored for the purposes of on-chip optical amplification. One such structure is the **slot waveguide**. This waveguide consists of two thin silicon waveguide rails that travel parallel to one another, leaving a small sub-micron size gap, or slot, between them. Optical modes that traverse this waveguide are enhanced in the lower-index slot as a superposition of the discontinuous electric fields from the high index silicon rails overlaps into this region [63]. The main issue with these waveguide amplifiers, however, arises from the high waveguide loss caused by scattering due to light interaction with the two silicon rails, which is usually higher than the outputted gain [64]. Another issue that may arise comes from the deposition onto the waveguide. As the film is laid, its particles begin to nucleate to the silicon rail structures and may do so across the slot region, leaving the slot unfilled and only containing air. This ceases the operation of the device as the light confined within the slot has no active material to overlap or interact with. This is a problem that this research group has run into, thus rendering the devices useless and the project abandoned.

Another promising candidate for silicon waveguide amplifiers is the **subwavelength grating (SWG) waveguide**. This periodic waveguide structure uses a series of subwavelength scale ($\Lambda < 300$ nm) silicon gratings in the longitudinal direction to create an effective medium of lower effective index than silicon that is determined by effective medium theory [65]. Light that travels through this medium propagates as Floquet-Bloch modes, which do not observe the discontinuities of the waveguide media that change periodically. The waveguide core effective index can be easily tuned during design phases to enable high overlap with an active top cladding material, thus increasing potential for high gain with loss similar to or less than that of a conventional wire waveguide.

These devices have not yet been demonstrated actively, but preliminary steps have been presented [24] and work towards this is well underway.

Other waveguide material platforms may also be explored. As mentioned in Chapter 1.3, silicon nitride (Si_3N_4) is a low loss, CMOS-compatible waveguide platform rising in popularity and has already been demonstrated as a TeO_2-coated waveguide amplifier for both the C-band [27] and 2 μm [28] telecom windows.

5.3 Skills acquired

Many skills were acquired by the primary researcher over the course of this project. First and foremost, the primary researcher gained valuable understanding and sufficient exposure to multiple photonic design and simulation tools, including software suite packages from Synopsys RSoft, Lumerical, Photon Design and Optiwave. Different mode computation methods, such as finite element method, finite difference method, beam propagation method, eigenmode expansion and finite-difference-time-domain method, were explored by the primary researcher and applied to this work as well as other projects. Part of the training for these programs came through attendance and participation of the Passive Silicon Photonics Fabrication Course offered through the NSERC Silicon Electronic-Photonic Integrated Circuits (SiEPIC) program [66], which was hosted by CMC Microsystems and took place at University of British Columbia (UBC) in Vancouver, Canada in August 2018. Other software-based skills that were improved upon include Matlab scripting and modelling, as well as design mask layout and GDS creation through Mentor Graphics Pyxis and KLayout.

Practical skills were amplified through use of optical and fiber optic equipment for measurements in the lab. Training on the operation and safe handling of low-wattage output tunable lasers, high-power pump laser diodes and EDFAs was provided in lab, and use of such equipment was executed by the primary researcher for both this work, as

well as other exploratory projects. Furthermore, prior knowledge of optical fiber cleaving, handling, safety and care from undergraduate experiences was enhanced through continual exposure and practice with such equipment.

Appendix A

Matlab Amplifier Model Code

```
% Amplifier Model
% TeO2:Er3+-coated SOI Wire Waveguide
% Master's Thesis

% Original code by Jonathan Bradley, September 2009
% Code adapted by Cameron Naraine, August 2020

% -------------------------------------------------------------------------
%% --- Simulation formatting --- %%
close all; clear; clc;
format long;

% % Other useful definitions
% I_15/2 = ground state
% I_13/2 = first excited energy state

% % References
% [19] K. T. Vu and S. J. Madden, Opt. Express 18(18), 19192-19200 (2010).
% [27] H. C. Frankis et al., Photonics Res. 8(2), 127-134 (2020).
% [41] J. D. B. Bradley, Ph.D. Thesis, University of Twente, (2009).
% [44] D. E. McCumber, Phys. Rev. 136(4A), 16-19 (1964).
% [56] C. Zhang, Master's Thesis, McMaster University, (2018).

% -------------------------------------------------------------------------
%% --- Physical constants --- %%
k = physconst('Boltzmann'); % Boltzmann's constant = 1.38064852e-23 (J/K)
h = 6.626068e-34;           % Planck's constant (J*s)
c = physconst('LightSpeed');% speed of light in vacuum = 299792458 (m/s)
e = exp(1);                 % e = 2.718281828
GPLfactor = 10*log10(e);    % gain/length factor for EDFA = 4.34294482 (dB)
% -------------------------------------------------------------------------
%% --- Load external data files --- %%
```

```
% TeO2 Confinement Factor [RSoft]
A = load('TeO2_Overlap_data.mat');
lambda_mat = A.lambda;
Gamma_mat = A.TeO2_Overlap; % [Design#1, Design#2]

% Mode effective area [RSoft]
A = load('Aeff_data.mat');
A_eff_mat = A.A_eff; % [Design#1, Design#2]

% Absorption Cross Section [27]
A = load('TeO2_AbsCS_data.mat');
sigma_a_mat = A.sigma_a;

% ------------------------------------------------------------------------
%% --- Simulation Selection --- %%
% sim_selection options:
%   0, [19] model verification
%   1, Design #1 as is on chip (vary Pp0)
%   2, Design #2 as is on chip (vary Pp0)
%   3, Design #1 to find optL (vary N)
%   4, Design #2 to find optL (vary N)
%   5, Design #1 SE & ING at optL (vary Pp0)
%   6, Design #2 SE & ING at optL (vary Pp0)
%   7, Design #1 as is on chip (vary alpha_p/s)
%   8, Design #2 as is on chip (vary alpha_p/s)
% design_sim indices:
%   0 = [19] Design
%   1 = Design #1 (AMF HCWG)
%   2 = Design #2 (ANT HOWG)

% Make selection (0 - 8)
sim_selection = 1;

% Get proper design details based on sim selection above
if sim_selection == 0
    design_sim = 0;
elseif sim_selection == 1 || ...
       sim_selection == 3 || ...
       sim_selection == 5 || ...
       sim_selection == 7
    design_sim = 1;
elseif sim_selection == 2 || ...
       sim_selection == 4 || ...
       sim_selection == 6 || ...
       sim_selection == 8
    design_sim = 2;
else % no selection, terminate program
    fprintf('Improper selection, terminating program...\n');
    quit;
end

% ------------------------------------------------------------------------
```

```
%% --- Parameters --- %%
% Constant parameters
T_room = 300;           % Room temperature (K)
lambda_m = 1532;        % source wavelength, mean (nm)
if design_sim == 0      % [19] model
    lambda_p = 1475;    % source wavelength, pump (nm)
    i_lambda_p = find(lambda_mat==lambda_p,1);
                        % wavelength index, pump
    lambda_s = [1535,1555,1600];
                        % source wavelength, signal (nm)
    Gamma_p = 0.9;      % TeO2 confinement factor, pump
    Gamma_s = 0.9 .* ones(size(lambda_mat));
                        % TeO2 confinement factor, signal
    A_eff_p = 5.24;     % mode effective area, pump (um^2)
    A_eff_s = 5.32 .* ones(size(lambda_mat));
                        % mode effective area, signal (um^2)
    sigma_p_a = sigma_a_mat(i_lambda_p);
                        % absorption cross section, pump (cm^2)
    sigma_s_a = sigma_a_mat;
                        % absorption cross section, signal (cm^2)
    tau = 1.3;          % I_13/2 lifetime (ms)
else                    % [This work]
    lambda_p = 1477;    % source wavelength, pump (nm)
    i_lambda_p = find(lambda_mat==lambda_p,1);
                        % wavelength index, pump
    lambda_s = [1533,1525,1565];
                        % source wavelength, signal (nm)
    Gamma_p = Gamma_mat(i_lambda_p,design_sim);
                        % TeO2 confinement factor, pump
    Gamma_s = Gamma_mat(:,design_sim);
                        % TeO2 confinement factor, signal
    A_eff_p = A_eff_mat(i_lambda_p,design_sim);
                        % mode effective area, pump (um^2)
    A_eff_s = A_eff_mat(:,design_sim);
                        % mode effective area, signal (um^2)
    sigma_p_a = sigma_a_mat(i_lambda_p);
                        % absorption cross section, pump (cm^2)
    sigma_s_a = sigma_a_mat;
                        % absorption cross section, signal (cm^2)
    tau = 2.6;          % I_13/2 lifetime (ms)
end
sigma_p_e = calc_sigma_e(lambda_p,lambda_m,sigma_p_a,T_room);
                    % emission cross section, pump (cm^2) [44]
sigma_s_e = calc_sigma_e(lambda_mat,lambda_m,sigma_s_a,T_room);
                    % emission cross section, signal (cm^2) [44]
alpha_p = 0.6;      % background absorption, pump (dB/cm)
alpha_s = 0.4;      % background absorption, signal (dB/cm)

% Define characteristics of signal wavelength array
lenlambda_s = length(lambda_s);     % signal wavelength array length
i_lambda_s = zeros(1,lenlambda_s);  % signal wavelength indices
for i = 1:lenlambda_s
    i_lambda_s(i) = find(lambda_mat>=round(lambda_s(i)),1);
```

```
end

% ------------------------------------------------------------------------
%% --- Parameters of interest (POI) --- %%
% Fixed POI based on simulation selection
if sim_selection == 0     % [19] model
    L = 5;                  % amplifier length (cm)
    N = 2.2 * 1e20;         % initial total population in entire system
    Ps0 = 0.01;             % launched signal power (mW)
elseif sim_selection == 1 % Design #1 as is on chip
    L = 0.93;               % amplifier length (cm)
    N = 10.0 * 1e20;        % initial total population in entire system
    Ps0 = 0.001;            % launched signal power (mW)
elseif sim_selection == 2 % Design #2 as is on chip
    L = 1.7;                % amplifier length (cm)
    N = 1.68 * 1e20;        % initial total population in entire system
    Ps0 = 0.001;            % launched signal power (mW)
elseif sim_selection == 3 || ...
       sim_selection == 4 % To find optL (either design)
    L = 70;                 % amplifier length (cm)
    Pp0 = 250;              % launched pump power (mW)
    Ps0 = 0.001;            % launched signal power (mW)
elseif sim_selection == 5 % Design #1 @ optL
    L = 38.22;              % optimal amplifier length (cm)
    N = 10.0 * 1e20;        % initial total population in entire system
    Ps0 = 0.001;            % launched signal power (mW)
elseif sim_selection == 6 % Design #2 @ optL
    L = 43.75;              % optimal amplifier length (cm)
    N = 1.68 * 1e20;        % initial total population in entire system
    Ps0 = 0.001;            % launched signal power (mW)
elseif sim_selection == 7 % Design #1 as is on chip
    L = 0.93;               % amplifier length (cm)
    N = 10.0 * 1e20;        % initial total population in entire system
    Pp0 = 250;              % launched pump power (mW)
    Ps0 = 0.001;            % launched signal power (mW)
elseif sim_selection == 8 % Design #2 as is on chip
    L = 1.7;                % amplifier length (cm)
    N = 1.68 * 1e20;        % initial total population in entire system
    Pp0 = 250;              % launched pump power (mW)
    Ps0 = 0.001;            % launched signal power (mW)
end

% Variable POI based on simulation selection + labels for printing/plotting
if sim_selection == 3 || sim_selection == 4 % vary N
    POI = [0.5,1,1.68,2,3,5,10];
    N = POI .* 1e20;        % initial total population in entire system
    unitStr = 'x 10^2^0 cm^-^3';
    POI_label = sprintf('Er Concentration (%s)',unitStr);
elseif sim_selection == 7 || sim_selection == 8 % vary alpha_p/s
    POI = [0.1,0.6,1.5,3,6,10,15];
    alpha_s = POI;          % background absorption, signal (dB/cm)
    alpha_p = POI;          % background absorption, pump (dB/cm)
    unitStr = 'dB/cm';
```

```
    POI_label = sprintf('Total Background Loss (%s)',unitStr);
else % vary Pp0
    POI = [0,0.3,1,4,10,25,60,100,150,250];
    Pp0 = POI;              % launched pump power (mW)
    unitStr = 'mW';
    POI_label = sprintf('Launched Pump Power (%s)',unitStr);
end
lenPOI = length(POI);

% Print POI
fprintf('--- Parameters of Interest ---\n');
fprintf('L = \n\t%.4g cm\n',L);
fprintf('Ps0 = \n\t%g mW\n',Ps0);
fprintf('Pp0 = \n');
for i = 1:length(Pp0)
    fprintf('\t%.4g mW\n',Pp0(i));
end
fprintf('N = \n');
for i = 1:length(N)
    fprintf('\t%.4gE20 cm^-3\n',N(i)*1e-20);
end
fprintf('alpha_s = \n');
for i = 1:length(alpha_s)
    fprintf('\t%.4g dB/cm\n',alpha_s(i));
end
fprintf('\n');

% % If considering Er absorption loss ...
% Calculate Er absorption coefficient and total background loss
% aEr_p = sigma_p_a .* N .* Gamma_p;
% aEr_s = sigma_s_a .* N .* Gamma_s;
% alphaEr_p = aEr_p .* GPLfactor;
% alphaEr_s = aEr_s .* GPLfactor;
% alpha_p = alpha_p + alphaEr_p;
% alpha_s = alpha_s + alphaEr_s;

% ------------------------------------------------------------------------
%% --- SI unit conversions --- %%
lambda_p = lambda_p * 1e-9;     % source wavelength, pump (m)
lambda_mat = lambda_mat .* 1e-9;% imported wavelength matrix(m)
a_p = alpha_p ./ GPLfactor ./ 1e-2;% absorption coefficient, pump (m^-1)
a_s = alpha_s ./ GPLfactor ./ 1e-2;% absorption coefficient, signal (m^-1)
sigma_p_a = sigma_p_a * 1e-4;   % absorption cross section, pump (m^2)
sigma_p_e = sigma_p_e * 1e-4;   % emission cross section, pump (m^2)
sigma_s_a = sigma_s_a .* 1e-4;  % absorption cross section, signal (m^2)
sigma_s_e = sigma_s_e .* 1e-4;  % emission cross section, signal (m^2)
A_eff_p = A_eff_p * 1e-12;      % mode effective area, pump (m^2)
A_eff_s = A_eff_s .* 1e-12;     % mode effective area, signal (m^2)
tau = tau * 1e-3;               % I_13/2 lifetime (s)

L = L .* 1e-2;                  % amplifier length (m)
N = N ./ 1e-6;                  % Er concentration (m^-3)
Pp0 = Pp0 .* 1e-3;              % launched pump power (W)
```

```
Ps0 = Ps0 .* 1e-3;              % launched signal power (W)
% ------------------------------------------------------------------------
%% --- Loop setup --- %%
% Calculate threshold intensities & powers
I_Th_p = h*c/(lambda_p*(sigma_p_a* ...
    (sigma_s_e(i_lambda_s(1))/sigma_s_a(i_lambda_s(1)))-sigma_p_e)*tau);
                                % threshold pump intensity (W/m^2)
P_Th_p = (10*log10((I_Th_p*A_eff_p)/0.001));
                                % threshold pump power (W -> dBm)

% Define length of arrays of POI
lenlambda = length(lambda_mat);
NumLoops = lenPOI*lenlambda;

% Longitudinal discretization
NumZ = 1000;                % # of propagation length steps
dz = L / NumZ;              % discretized slices along propagation axis (m)

% Initialize storage matrices
Ppz = zeros(NumLoops,NumZ);     % pump intensity array for each dz
Psz = zeros(NumLoops,NumZ);     % signal intensity array for each dz

% Calculate initial populations
N2_0Perc = 1;                   % initial % of total population, I_13/2
N2_0 = N .* N2_0Perc/100;       % initial total population, I_13/2
N1_0 = N - N2_0;                % initial total population, I_15/2

% Initialize population storage matrices
N1z = ones(NumLoops,NumZ);      % I_15/2 population for each dz
N2z = ones(NumLoops,NumZ);      % I_13/2 population for each dz
if length(N) > 1                % sim_selection == 3 or 4
    for i = 1:lenPOI
        a = lenlambda*(i-1)+1;
        b = lenlambda*i;
        N1z(a:b,:) = N1z(a:b,:) .* N1_0(i);
        N2z(a:b,:) = N2z(a:b,:) .* N2_0(i);
    end
else
    N1z = N1z .* N1_0';
    N2z = N2z .* N2_0';
end

% ------------------------------------------------------------------------
%% --- Loop --- %%
POI_info = zeros(NumLoops,2);   % Sorting array for POI
row = 1;                        % iteration through loop
indN = 1; indPp0 = 1; inda = 1; % default POI indices

for indPOI = 1:lenPOI
    for jj = 1:lenlambda

        % Store POI info
        POI_info(row,1) = POI(indPOI);
```

```
POI_info(row,2) = lambda_mat(jj)*1e9;

% Define POI index
if length(N) > 1
    indN = indPOI;
elseif length(Pp0) > 1
    indPp0 = indPOI;
elseif length(a_s) > 1
    inda = indPOI;
end

% Initialize storage matrices for equation solutions
PpzNew = zeros(1,NumZ); % Pump intensity array for each dz
PszNew = zeros(1,NumZ); % Signal intensity array for each dz
N2zNew = zeros(1,NumZ); % I_13/2 population for each dz
N1zNew = zeros(1,NumZ); % I_15/2 population for each dz

% Initialize first element of power arrays
PpzNew(1) = Pp0(indPp0);
PszNew(1) = Ps0;

% Iterate through the waveguide longitudinally (z axis)
for ii = 1:NumZ
    % Calculate photon fluxes for pump and signal
    phi_p = (PpzNew(ii)/A_eff_p) / (h*c/lambda_p);
    phi_s = (PszNew(ii)/A_eff_s(jj)) / (h*c/lambda_mat(jj));

    % Solve rate equations using steady state conditions:
    %  (dN2/dt = -dN1/dt = 0 & N1 + N2 = N)
    numer = sigma_s_a(jj)*phi_s + sigma_p_a*phi_p;
    denom = 1/tau + phi_s*(sigma_s_a(jj)+sigma_s_e(jj)) ...
        + phi_p*(sigma_p_a+sigma_p_e);
    N2zNew(ii) = numer / denom * N(indN);
    N1zNew(ii) = N(indN) - N2zNew(ii);
    N1 = N1zNew(ii);
    N2 = N2zNew(ii);

    % Solve propagation equations ( Ip(z + dz) & Is(z + dz) )
    %  to determine power change in active region over dz
    dIpdz = (N2*sigma_p_e - N1*sigma_p_a);
    dIsdz = (N2*sigma_s_e(jj) - N1*sigma_s_a(jj));

    % Calculate power change in active and passive regions
    % - Active regions use propagation equation sol'n's above
    % - Passive regions only encounter background loss
    Ppz_act = PpzNew(ii)*Gamma_p * exp((dIpdz-a_p(inda))*dz);
    Ppz_pas = PpzNew(ii)*(1-Gamma_p) * exp(-a_p(inda)*dz);
    Psz_act = PszNew(ii)*Gamma_s(jj) * exp((dIsdz-a_s(inda))*dz);
    Psz_pas = PszNew(ii)*(1-Gamma_s(jj)) * exp(-a_s(inda)*dz);

    % Calculate change in total power after iteration in dz
    PpzNew(ii+1) = Ppz_act + Ppz_pas;
    PszNew(ii+1) = Psz_act + Psz_pas;
```

```
        end

        % Fill original z-dependent arrays with temp new arrays
        Ppz(row,:) = PpzNew(2:NumZ+1);
        Psz(row,:) = PszNew(2:NumZ+1);
        N1z(row,:) = N1zNew;
        N2z(row,:) = N2zNew;

        % Next row
        row = row + 1;
    end
end

% ---------------------------------------------------------------------
%% --- Convert back from SI Units --- %%
Ppz = 10.*log10(Ppz./0.001);    % pump power array for each dz (dBm)
Psz = 10.*log10(Psz./0.001);    % signal power array for each dz (dBm)

N1z = N1z ./ 1e6;               % I_15/2 population for each dz (cm^-3)
N2z = N2z ./ 1e6;               % I_13/2 population for each dz (cm^-3)

L = L .* 1e2;                   % amplifier length (cm)
N = N ./ 1e6;                   % Er concentration (cm^-3)
Ps0 = Ps0 .* 1e3;               % launched signal power (mW)
Pp0 = Pp0 .* 1e3;               % launched pump power (mW)
dz = dz .* 1e2;                 % discretized slices along propagation axis (cm)

lambda_p = lambda_p * 1e9;      % source wavelength, pump (nm)
lambda_mat = lambda_mat .* 1e9; % imported wavelength matrix (nm)
tau = tau * 1e3;                % I_13/2 lifetime (ms)
a_p = a_p ./ 1e2;               % absorption coefficient, pump (cm^-1)
a_s = a_s ./ 1e2;               % absorption coefficient, signal (cm^-1)
sigma_p_a = sigma_p_a * 1e4;    % absorption cross section, pump (cm^2)
sigma_p_e = sigma_p_e * 1e4;    % emission cross section, pump (cm^2)
sigma_s_a = sigma_s_a .* 1e4;   % absorption cross section, signal (cm^2)
sigma_s_e = sigma_s_e .* 1e4;   % emission cross section, signal (cm^2)
A_eff_p = A_eff_p * 1e12;       % mode effective area, pump (um^2)
A_eff_s = A_eff_s .* 1e12;      % mode effective area, signal (um^2)

% ---------------------------------------------------------------------
%% --- PLOTS --- %%
% Plot Settings
sz = 100;
lw = 2;
fs1 = 13;
fs2 = 14;
colA = {'b','r','k','g','c','m','y','w'};

fix_y_axes = 0;
if sim_selection == 3 || sim_selection == 4
    fix_y_axes = 0;
end
```

```
% ------------------------------------------------------------------------
%% --- Position vs. ... Plots --- %%
xx = 1:NumZ;
xx = xx .* dz';
loc = 'EastOutside';

% vs. Pump Power
figure;
xlimit = [0 L];
if sim_selection == 0; ylimit = [-30 30];
elseif sim_selection == 1 || sim_selection == 2; ylimit = [-20 30];
elseif sim_selection == 5 || sim_selection == 6; ylimit = [-30 30];
elseif sim_selection == 7 || sim_selection == 8; ylimit = [-5 25]; end

plot(xlimit,[P_Th_p P_Th_p],'--k', ...
    'DisplayName','P_p_,_T_h', ...
    'LineWidth',lw);
hold on;
if length(alpha_s) > 1
for j = 1:lenPOI
    ROI = findROI(POI_info,POI(j),lambda_s(1));
    pl = plot(xx,Ppz(ROI,:), ...
        'DisplayName',sprintf('%5.4g %s',POI(j),unitStr), ...
        'LineWidth',lw);
    if j > 7; pl.Color = colA{lenPOI-j+1}; end
end
else
for j = lenPOI:-1:1
    if ~(lenPOI == length(Pp0) && j == 1)
        ROI = findROI(POI_info,POI(j),lambda_s(1));
        pl = plot(xx,Ppz(ROI,:), ...
            'DisplayName',sprintf('%5.4g %s',POI(j),unitStr), ...
            'LineWidth',lw);
        if j > 7; pl.Color = colA{lenPOI-j+1}; end
    end
end
end
hold off;
xlim(xlimit);
if fix_y_axes; ylim(ylimit); end
set(gca, 'fontsize', fs1);
xlabel('z (cm)', 'fontweight', 'bold', 'fontsize', fs2);
ylabel('Pump Power (dBm)', 'fontweight', 'bold', 'fontsize', fs2);
legend('Location',loc);
box on; grid on;

% vs. Signal Power
figure;
if sim_selection == 0; ylimit = [-60 0];
elseif sim_selection == 1 || sim_selection == 2; ylimit = [-36 -26];
elseif sim_selection == 5 || sim_selection == 6; ylimit = [-50 10];
elseif sim_selection == 7 || sim_selection == 8; ylimit = [-55 -25]; end
hold on;
```

```
if length(alpha_s) > 1
for j = 1:lenPOI
    ROI = findROI(POI_info,POI(j),lambda_s(1));
    pl = plot(xx,Psz(ROI,:), ...
        'DisplayName',sprintf('%5.4g %s',POI(j),unitStr), ...
        'LineWidth',lw);
    if j > 7; pl.Color = colA{lenPOI-j+1}; end
end
else
for j = lenPOI:-1:1
    ROI = findROI(POI_info,POI(j),lambda_s(1));
    pl = plot(xx,Psz(ROI,:), ...
        'DisplayName',sprintf('%5.4g %s',POI(j),unitStr), ...
        'LineWidth',lw);
    if j > 7; pl.Color = colA{lenPOI-j+1}; end
end
end
hold off;
xlim(xlimit);
if fix_y_axes; ylim(ylimit); end
set(gca, 'fontsize', fs1);
xlabel('z (cm)', 'fontweight', 'bold', 'fontsize', fs2);
ylabel('Signal Power (dBm)', 'fontweight', 'bold', 'fontsize', fs2);
legend('Location',loc);
box on; grid on;

% vs. Upper State Population
if sim_selection < 7
figure;
plot(xlimit,[0.5 0.5],'--k','DisplayName','Threshold','LineWidth',lw);
hold on;
for j = lenPOI:-1:1
    if length(N) == 1; indN = 1; else; indN = j; end
    ROI = findROI(POI_info,POI(j),lambda_s(1));
    pl = plot(xx,N2z(ROI,:)./N(indN), ...
        'DisplayName',sprintf('%5.4g %s',POI(j),unitStr), ...
        'LineWidth',lw);
    if j > 7; pl.Color = colA{lenPOI-j+1}; end
end
hold off;
xlim(xlimit);
if sim_selection == 7 || sim_selection == 8
    xticks(min(xlim):3:max(xlim));
end
ylim([0 1]);
set(gca, 'fontsize', fs1);
xlabel('z (cm)', 'fontweight', 'bold', 'fontsize', fs2);
ylabel('Upper State Population', 'fontweight', 'bold', 'fontsize', fs2);
legend('Location',loc);
box on; grid on;
end
% ------------------------------------------------------------------------
%% --- POI vs. ... Plots --- %%
```

```
optL = zeros(1,lenPOI);              % Optimal amplifier length (cm)
i_optL = zeros(1,lenPOI);            % Index of optimal amplifier length
USP = zeros(2,lenPOI);               % Upper state population (%)
g = zeros(lenlambda_s,lenPOI);       % Internal gain (dB)
G = zeros(lenlambda_s,lenPOI);       % Internal net gain (dB)
gamma = zeros(lenlambda_s,lenPOI);   % Internal net gain (dB/cm)

xlimit = [0 max(POI)];
for j = 1:lenPOI
    if length(N) == 1; indN = 1; else; indN = j; end
    if length(alpha_s) == 1; inda = 1; else; inda = j; end
    ROI = findROI(POI_info,POI(j),lambda_s(1));
    % Solve optimal amplifier length
    opt = find(Ppz(ROI,:)<=P_Th_p,1);
    if isempty(opt)
        optL(j) = L;
        i_optL(j) = NumZ;
    else
        optL(j) = opt * dz;
        i_optL(j) = find(xx>=optL(j),1);
    end
    % Solve upper state population
    USP(1,j) = N2z(ROI,NumZ)/N(indN); % USP @ z = L
    USP(2,j) = N2z(ROI,i_optL(j))/N(indN); % USP @ z = optL
    % Solve internal gain, total internal net gain &
    %  internal net gain per unit length
    for i = 1:lenlambda_s
        ROI = findROI(POI_info,POI(j),lambda_s(i));
        g(i,j) = (Psz(ROI,NumZ) - Psz(ROI,1));
        G(i,j) = g(i,j) - alpha_s(inda)*L;
        gamma(i,j) = G(i,j) / L;
    end
end

if sim_selection == 3 || sim_selection == 4
    loc = 'NorthEast';
else
    loc = 'SouthEast';
end

% vs. Optimal Amplifier Length
if sim_selection >= 3 && sim_selection < 7
figure;
scatter(POI,optL, ...
    sz,sprintf('%sx',colA{1}), ...
    'DisplayName',sprintf('%d nm',lambda_s(1)), ...
    'LineWidth',lw);
xlim(xlimit);
ylim([0 L]);
set(gca, 'fontsize', fs1);
xlabel(POI_label, 'fontweight', 'bold', 'fontsize', fs2);
ylabel('Optimal Amplifier Length (cm)', ...
    'fontweight', 'bold', 'fontsize', fs2);
```

```
legend('Location',loc);
box on; grid on;
if sim_selection == 3 || sim_selection == 4
save(sprintf('S%dD%d_N_v_optL_%d_LPP%d_V11', ...
    sim_selection,design_sim,lambda_s(1),Pp0) ...
    ,'POI','optL');
end
end

% vs. Upper State Population
if sim_selection < 7
figure;
plot(xlimit,[0.5 0.5],'--k', ...
    'DisplayName','Threshold', ...
    'LineWidth',lw);
hold on;
scatter(POI,USP(1,:), ...
    sz,sprintf('%sx',colA{1}), ...
    'DisplayName',sprintf('L = %g cm',L), ...
    'LineWidth',lw);
scatter(POI,USP(2,:), ...
    sz,sprintf('%sx',colA{2}), ...
    'DisplayName','L = optL', ...
    'LineWidth',lw);
hold off;
xlim(xlimit);
ylim([0 1]);
set(gca, 'fontsize', fs1);
xlabel(POI_label, 'fontweight', 'bold', 'fontsize', fs2);
ylabel('Upper State Population (z = L_o_p_t)', ...
    'fontweight', 'bold', 'fontsize', fs2);
title(sprintf('%d nm',lambda_s(1)));
legend('Location',loc);
box on; grid on;
end

% vs. Gain (setup) ------------------------------------------------------
figure;
if sim_selection == 0
    ylim_G = [-35 15]; ylim_GPL = [-7 3];
elseif sim_selection == 1 || sim_selection == 2
    ylim_G = [-7 2]; ylim_GPL = ylim_G;
elseif sim_selection == 5 || sim_selection == 6
    ylim_G = [-200 20]; ylim_GPL = [-10 1];
elseif sim_selection == 7 || sim_selection == 8
    ylim_G = [-50 10]; ylim_GPL = ylim_G;
    tickX = 1;
end

if sim_selection == 3 || sim_selection == 4
    loc = 'South';
elseif sim_selection == 7 || sim_selection == 8
    loc = 'SouthWest';
```

```
else
    loc = 'SouthEast';
end

% vs. Internal Gain
plot(xlimit,[0 0],'--k', ...
    'DisplayName','Threshold', ...
    'LineWidth',lw);
hold on;
for i = 1:lenlambda_s
    plot(POI,g(i,:), ...
        sprintf('-%ss',colA{i}), ...
        'DisplayName',sprintf('%d nm',lambda_s(i)), ...
        'LineWidth',lw);
end
hold off;
xlim(xlimit);
if sim_selection == 7 || sim_selection == 8
    xticks(min(xlim):tickX:max(xlim));
end
if fix_y_axes; ylim(ylim_G); end
set(gca, 'fontsize', fs1);
ylabel('Internal Gain (dB)', 'fontweight', 'bold', 'fontsize', fs2);
xlabel(POI_label, 'fontweight', 'bold', 'fontsize', fs2);
legend('Location',loc);
box on; grid on;

% vs. Total Internal Net Gain
figure;
plot(xlimit,[0 0],'--k', ...
    'DisplayName','Threshold', ...
    'LineWidth',lw);
hold on;
for i = 1:lenlambda_s
    plot(POI,G(i,:), ...
        sprintf('-%s^',colA{i}), ...
        'DisplayName',sprintf('%d nm',lambda_s(i)), ...
        'LineWidth',lw);
end
hold off;
xlim(xlimit);
if sim_selection == 7 || sim_selection == 8
    xticks(min(xlim):tickX:max(xlim));
end
if fix_y_axes; ylim(ylim_G); end
set(gca, 'fontsize', fs1);
ylabel('Total Internal Net Gain (dB)', 'fontweight', 'bold', 'fontsize', fs2);
xlabel(POI_label, 'fontweight', 'bold', 'fontsize', fs2);
legend('Location',loc);
box on; grid on;

% vs. Internal Net Gain per Unit Length
figure;
```

```
plot(xlimit,[0 0],'--k', ...
    'DisplayName','Threshold', ...
    'LineWidth',lw);
hold on;
for i = 1:lenlambda_s
    plot(POI,gamma(i,:), ...
        sprintf('-%so',colA{i}), ...
        'DisplayName',sprintf('%d nm',lambda_s(i)), ...
        'LineWidth',lw);
end
hold off;
xlim(xlimit);
if sim_selection == 7 || sim_selection == 8
    xticks(min(xlim):tickX:max(xlim));
end
if fix_y_axes; ylim(ylim_GPL); end
set(gca, 'fontsize', fs1);
ylabel('Internal Net Gain (dB/cm)', 'fontweight', 'bold', 'fontsize', fs2);
xlabel(POI_label, 'fontweight', 'bold', 'fontsize', fs2);
legend('Location',loc);
box on; grid on;

% vs. All internal net gain values at 1533 nm
i = 1;
figure;
plot(xlimit,[0 0],'--k','DisplayName','Threshold','LineWidth',lw);
hold on;
yyaxis left;
plot(POI,G(i,:), ...
    sprintf('-%s^',colA{2}), ...
    'DisplayName',sprintf('%d nm',lambda_s(1)), ...
    'LineWidth',lw);
hold off;
ylabel('Total Internal Net Gain (dB)', 'fontweight','bold', 'fontsize',fs2);
if fix_y_axes; ylim(ylim_G); end
set(gca, 'YColor', colA{2});
yyaxis right;
plot(POI,gamma(i,:), ...
    sprintf('-%so',colA{3}), ...
    'DisplayName',sprintf('%d nm',lambda_s(1)), ...
    'LineWidth',lw);
ylabel('Internal Net Gain (dB/cm)', 'fontweight', 'bold', 'fontsize', fs2);
if fix_y_axes; ylim(ylim_GPL); end
set(gca, 'YColor', colA{3});
set(gca, 'fontsize', fs1);
xlabel(POI_label, 'fontweight', 'bold', 'fontsize', fs2);
xlim(xlimit);
if sim_selection == 7 || sim_selection == 8
    xticks(min(xlim):tickX:max(xlim));
end
legend('Location',loc);
box on; grid on;
```

```
% ------------------------------------------------------------------------
%% --- Wavelength vs. ... Plots --- %%
if sim_selection ~= 0

% loc = 'EastOutside';
loc = 'SouthEast';
tickSpac = 20;
gW = zeros(lenPOI,lenlambda);    % Internal gain (dB)
GW = zeros(lenPOI,lenlambda);    % Total internal net gain (dB)
gammaW = zeros(lenPOI,lenlambda);  % Internal net gain PUL (dB/cm)
xlimit = [1460 1640];

% vs. Internal Gain
figure(10);
plot(xlimit,[0 0], ...
    '--k', ...
    'DisplayName','Threshold', ...
    'LineWidth',lw);
hold on;

% vs. Total Internal Net Gain
figure(11);
plot(xlimit,[0 0], ...
    '--k', ...
    'DisplayName','Threshold', ...
    'LineWidth',lw);
hold on;

% vs. Internal Net Gain per Unit Length
figure(12);
plot(xlimit,[0 0], ...
    '--k', ...
    'DisplayName','Threshold', ...
    'LineWidth',lw);
hold on;

for i = lenPOI:-1:1

    for j = 1:lenlambda
        if length(alpha_s) == 1; inda = 1; else; inda = i; end
        ROI = findROI(POI_info,POI(i),lambda_mat(j));
        % Solve internal gain, total internal net gain &
        %  internal net gain per unit length
        gW(i,j) = Psz(ROI,NumZ) - Psz(ROI,1);
        GW(i,j) = gW(i,j) - alpha_s(inda)*L;
        gammaW(i,j) = GW(i,j) / L;
    end

    figure(10);
    pl = plot(lambda_mat,gW(i,:), ...
        'DisplayName',sprintf('%5.4g %s',POI(i),unitStr), ...
        'LineWidth',lw);
    if i > 7; pl.Color = colA{lenPOI-i+1}; end
```

```
    figure(11);
    pl = plot(lambda_mat,GW(i,:), ...
        'DisplayName',sprintf('%5.4g %s',POI(i),unitStr), ...
        'LineWidth',lw);
    if i > 7; pl.Color = colA{lenPOI-i+1}; end

    figure(12);
    pl = plot(lambda_mat,gammaW(i,:), ...
        'DisplayName',sprintf('%5.4g %s',POI(i),unitStr), ...
        'LineWidth',lw);
    if i > 7; pl.Color = colA{lenPOI-i+1}; end

end

figure(10);
hold off;
set(gca, 'fontsize', fs1);
ylabel('Internal Gain (dB)', 'fontweight', 'bold', 'fontsize', fs2);
if fix_y_axes; ylim(ylim_G); end
xlim(xlimit);
xticks(1460:tickSpac:1640);
xlabel('Wavelength (nm)', 'fontweight', 'bold', 'fontsize', fs2);
legend('Location',loc);
box on; grid on;

figure(11);
hold off;
set(gca, 'fontsize', fs1);
ylabel('Total Internal Net Gain (dB)', 'fontweight','bold', 'fontsize',fs2);
if fix_y_axes; ylim(ylim_G); end
xlim(xlimit);
xticks(1460:tickSpac:1640);
xlabel('Wavelength (nm)', 'fontweight', 'bold', 'fontsize', fs2);
legend('Location',loc);
box on; grid on;

figure(12);
hold off;
set(gca, 'fontsize', fs1);
ylabel('Internal Net Gain (dB/cm)', 'fontweight', 'bold', 'fontsize', fs2);
if fix_y_axes; ylim(ylim_GPL); end
xlim(xlimit);
xticks(1460:tickSpac:1640);
xlabel('Wavelength (nm)', 'fontweight', 'bold', 'fontsize', fs2);
legend('Location',loc);
legend('Location','SouthEast');
box on; grid on;

end

% ------------------------------------------------------------------------
%% --- FUNCTIONS  --- %%
```

```
function ROI = findROI(POI_mat,POI,lambda_s)
    tol = 1e-6;
    ROI = find( ...
        POI_mat(:,1)>=POI-tol & ...
        POI_mat(:,2)>=lambda_s-tol , ...
        1);
end

function sigma_e = calc_sigma_e(lambda,lambda_mean,sigma_a,T)
    % McCumber theory states [44]:
    % % sigma_e(v) = sigma_a(v) * exp [(epsilon-hv)/kT];
    % % % where: v = c / lambda;

    % Inputted units:
    % % lambda in (nm); lambda_mean in (nm); sigma_a in (cm^2); T in (K);
    k = physconst('Boltzmann');      % Boltzmann's constant (J/K)
    E_mean = 1e7 ./ lambda_mean;     % epsilon (cm^-1)
    E_hv = 1e7 ./ lambda;            % hv (cm^-1)
    kT = (k * T) / 1.9863e-23;       % thermal distribution term (cm^-1)
    eTerm = (E_mean-E_hv) ./ kT;     % exp term in McCumber Equation
    sigma_e = sigma_a .* exp(eTerm);% Solve sigma_e using McCumber Equation
end

% ------------------------------------------------------------------------
```

Bibliography

[1] G. T. Reed, "The optical age of silicon," Nature **427**, 595-–596 (2004).

[2] G. T. Reed, G. Z. Mashanovich, F. Y. Gardes, and D. J. Thomson, "Silicon optical modulators," Nat. Photonics **4**(8), 518—526 (2010).

[3] M. Lipson, "Guiding, modulating, and emitting light on Silicon - Challenges and opportunities," J. Light. Technol. **23**(12), 4222-–4238 (2005).

[4] D. Thomson, A. Zilkie, J. E. Bowers, T. Komljenovic, G. T. Reed, L. Vivien, D. Marris-Morini, E. Cassan, L. Virot, J.-M. Fédéli, J.-M. Hartmann, J. H. Schmid, D.-X. Xu, F. Boeuf, P. O'Brien, G. Z. Mashanovich, and M. Nedeljkovic, "Roadmap on silicon photonics," J. Opt. **18**(7), 1—20 (2016).

[5] R. A. Soref, "The Past, Present, and Future of Silicon Photonics," IEEE J. Sel. Top. Quantum Electron. **12**(6), 1678-–1687 (2006).

[6] E. J. Harvey, "Design and fabrication of silicon on insulator optical waveguide devices," Master's Thesis, Rochester Institute of Technology (2006).

[7] L. Pavesi, "Routes toward silicon-based lasers," Mater. Today **8**(1), 18-–25 (2005).

[8] G. T. Reed and A. P. Knights, *Silicon Photonics: An Introduction*, First Edition, John Wiley and Sons Inc., (2004).

[9] T. K. Liang, L. R. Nunes, T. Sakamoto, K. Sasagawa, T. Kawanishi, M. Tsuchiya, G. R. A. Priem, D. Van Thourhout, P. Dumon, R. Baets, and H. K. Tsang, "Ultrafast all-optical switching by cross-absorption modulation in silicon wire waveguides," Opt. Express **13**(19), 7298-–7303 (2005).

[10] A. J. Kenyon, "Erbium in silicon," Semicond. Sci. Technol. **20**(12), (2005).

[11] I. P. Kaminow and T. Li, textitOptical Fiber Telecommunications IVA: Components, Academic Press, (2002).

[12] D.-X. Xu, J. H. Schmid, G. T. Reed, G. Z. Mashanovich, D. J. Thomson, M. Nedeljkovic, X. Chen, D. Van Thourhout, S. Keyvaninia, and S. K. Selvaraja, "Silicon Photonic Integration Platform—Have We Found the Sweet Spot?," IEEE J. Sel. Top. Quantum Electron. **20**(4), (2014).

[13] A. J. Kenyon, "Recent developments in rare-earth doped materials for optoelectronics," Prog. Quantum Electron. **26**(1), 225-–284 (2002).

[14] A. Mori, "Tellurite-based fibers and their applications to optical communication networks," J. Ceram. Soc. Japan **116**(10), 1040—1051 (2008).

[15] R. El-Mallawany, "The optical properties of tellurite glasses," J. Appl. Phys. **72**(5), 1774-–1777 (1992).

[16] A. Jha, B. Richards, G. Jose, T. Teddy-Fernandez, P. Joshi, X. Jiang, and J. Lousteau, "Rare-earth ion doped TeO_2 and GeO_2 glasses as laser materials," Prog. Mater. Sci. **57**(8), 1426—1491 (2012).

[17] H. C. Frankis, K. M. Kiani, D. B. Bonneville, C. Zhang, S. Norris, R. Mateman, A. Leinse, N. D. Bassim, A. P. Knights, and J. D. B. Bradley, "Low-loss TeO_2-coated

Si_3N_4 waveguides for application in photonic integrated circuits," Opt. Express **27**(9), 12529-–12540 (2019).

[18] S. J. Madden and K. T. Vu, "Very low loss reactively ion etched Tellurium Dioxide planar rib waveguides for linear and non-linear optics," Opt. Express **17**(20), 17645–17651 (2009).

[19] K. T. Vu and S. J. Madden, "Tellurium dioxide Erbium doped planar rib waveguide amplifiers with net gain and 2.8 dB/cm internal gain," Opt. Express **18**(18), 19192-–19200 (2010).

[20] K. Vu, S. Farahani, and S. J. Madden, "980 nm pumped erbium doped tellurium oxide planar rib waveguide laser and amplifier with gain in S, C and L band," Opt. Express **23**(2), 747-–755 (2015).

[21] G. C. Righini and M. Ferrari, "Photoluminescence of rare-earth-doped glasses," Riv. del Nuovo Cim. **28**(12), 1—53 (2005).

[22] H. C. Frankis, K. M. Kiani, D. Su, R. Mateman, A. Leinse, and J. D. B. Bradley, "High-Q tellurium-oxide-coated silicon nitride microring resonators," Opt. Lett. **44**(1), 118—121 (2019).

[23] J. H. Schmid, A. Delâge, B. Lamontagne, J. Lapointe, S. Janz, P. Cheben, A. Densmore, P. Waldron, D.-X. Xu, and K. P. Yap, "Interference effect in scattering loss of high-index- contrast planar waveguides caused by boundary reflections," Opt. Lett. **33**(13), 1479-–1481 (2008).

[24] C. M. Naraine, J. W. Miller, H. C. Frankis, D. E. Hagan, P. Mascher, J. H. Schmid, P. Cheben, A. P. Knights, and J. D. B. Bradley, "Subwavelength grating metamaterial waveguides functionalized with tellurium oxide cladding," Opt. Express **28**(12), 18538—18547 (2020).

[25] R. Nayak, V. Gupta, A. L. Dawar, and K. Sreenivas, "Optical waveguiding in amorphous tellurium oxide thin films," Thin Solid Films **445**, 118–126 (2003).

[26] S. M. Pietralunga, M. Lanata, M. Feré, D. Piccinin, G. Cusmai, M. Torregiani, and M. Martinelli, "High-contrast waveguides in sputtered pure TeO_2 glass thin films," Opt. Express **16**(26), 21662–21670 (2008).

[27] H. C. Frankis, H. M. Mbonde, D. B. Bonneville, C. Zhang, R. Mateman, A. Leinse, and J. D. B. Bradley, "Erbium-doped TeO_2-coated Si_3N_4 waveguide amplifiers with 5 dB net gain," Photonics Res. **8**(2), 127—134 (2020).

[28] K. M. Kiani, H. C. Frankis, H. M. Mbonde, R. Mateman, A. Leinse, A. P. Knights, and J. D. B. Bradley, "Thulium- doped tellurium oxide waveguide amplifier with 7.6 dB net gain on a silicon nitride chip," Opt. Lett. **44**(23), 5788—5791 (2019).

[29] F. L. Pedrotti, L. M. Pedrotti and L. S. Pedrotti, *Introduction to Optics*, Third Edition, Pearson Prentice Hall, (2007).

[30] R. G. Hunsperger, *Integrated Optics: Theory and Technology*, Sixth Edition, Springer Media, (2009).

[31] E. A. J. Marcatili, "Dielectric Rectangular Waveguide and Directional Coupler for Integrated Optics," Bell Syst. Tech. J. **48**, 2071—2102 (1969).

[32] Synopsis RSoft Photonic Device Tools: https://www.synopsys.com/photonic-solutions/rsoft-photonic-device-tools.html

[33] J. D. Jackson, *Classical Electrodynamics*, Third Edition, John Wiley and Sons Inc., (1998), pp. 310.

[34] K. McGarvey-Lechable, "Design of Slow Light Modes in Photonic Crystal Ring Resonators," Master's Thesis, Concordia University, Canada (2015).

[35] F. P. Payne and J. P. R. Lacey, "A theoretical analysis of scattering loss from planar optical waveguides," Opt. Quantum Electron. **26**, 977-–986 (1994).

[36] A. G. Rickman, G. T. Reed, and F. Namavar, "Silicon-on-Insulator Optical Rib Waveguide Loss and Mode Characteristics," J. Light. Technol. **12**(10), 1771-–1776 (1994).

[37] P. C. Becker, N. A. Olsson and J. R. Simpson, *Erbium-Doped Fiber Amplifiers: Fundamentals and Technology*, First Edition, Academic Press, (1999).

[38] M. J. F. Digonnet, *Rare-Earth-Doped Fiber Lasers and Amplifiers*, Second Edition, Marcel Dekker Inc., (2001).

[39] H. Steinkemper, S. Fischer, M. Hermle, and J. C. Goldschmidt, "Stark level analysis of the spectral line shape of electronic transitions in rare earth ions embedded in host crystals," New J. Phys. **15**, (2013).

[40] E. Desurvire and J. R. Simpson, "Amplification of Spontaneous Emission in Erbium-Doped Single-Mode Fibers," J. Light. Technol. **7**(5), 835—845 (1989).

[41] J. D. B. Bradley, "Al_2O_3:Er^{3+} as a Gain Platform for Integrated Optics," Ph.D. Thesis, University of Twente, Netherlands (2009).

[42] W. Ryba-Romanowski, "Effect of temperature and activator concentration on luminescence decay of erbium-doped tellurite glass," J. Lumin. **46**, 163-–172 (1990).

[43] P. W. Milonni and J. H. Eberly, *Lasers*. New York: Wiley, (1988).

[44] D. E. McCumber, "Einstein relations connecting broadband emission and absorption spectra," Phys. Rev. **136**(4A), 16-–19 (1964).

[45] W. J. Miniscalco and R. S. Quimby, "General procedure for the analysis of Er^{3+} cross sections," Opt. Lett. **16**(4), 258—260 (1991).

[46] Advanced Micro Foundry: http://www.advmf.com/

[47] Applied NanoTools: https://www.appliednt.com/

[48] H. C. Frankis, D. B. Bonneville, D. Su, and J. D. B. Bradley, "Silicon waveguide integrated with a tellurium oxide whispering gallery resonator on chip (Conference Presentation)," Proc. SPIE 10923, Silicon Photonics XIV, 109230D (4 March 2019).

[49] N. Li, M. Xin, Z. Su, E. S. Magden, N. Singh, J. Notaros, E. Timurdogan, Purnawirman, J. D. B. Bradley, and M. R. Watts, "A Silicon Photonic Data Link with a Monolithic Erbium-Doped Laser," Scientific Reports **10**, 1114 (2020).

[50] E. S. Magden, N. Li, Purnawirman, J. D. B. Bradley, N. Singh, A. Ruocco, G. S. Petrich, G. Leake, D. D. Coolbaugh, E. P. Ippen, M. R. Watts, and L. A. Kolodziejski, "Monolithically-integrated distributed feedback laser compatible with CMOS processing," Opt. Express **25**(15), 18058—18065 (2017).

[51] K. H. Huebner, D. L. Dewhirst, D. E. Smith, T. G. Byrom, "The Finite Element Method for Engineers," Wiley-Interscience, (2001).

[52] M. Koshiba, "Optical Waveguide Theory by the Finite Element Method," IEICE Trans. Electron. **E97.C**(7), 625—635 (2014).

[53] A. Kichidis, N. Pleros, and A. Miliou, "Development of a Finite Element Method Mode Solver Application for Optical Waveguides," in Balkan Conference of Informatics **1036**, 25-–31 (2013).

[54] L. Chrostowski, and M. Hochberg, "Silicon Photonics Design," Cambridge University Press, (2015).

[55] J. M. Heaton, M. M. Bourke, S. B. Jones, B. H. Smith, K. P. Hilton, G. W. Smith, J. C. H. Birbeck, G. Berry, S. V. Dewar, and D. R. Wight, "Optimization of Deep-Etched, Single-Mode GaAs/AlGaAs Optical Waveguides Using Controlled Leakage into the Substrate," J. Light. Technol. **17**(2), 267—281 (1999).

[56] H. Huang, K. Liu, B. Qi, and V. J. Sorger, "Re-Analysis of Single-Mode Conditions for Silicon Rib Waveguides at 1550 nm Wavelength," J. Light. Technol. **34**(16), 3811—3817 (2016).

[57] C. Zhang, "Design of Erbium-Doped Tellurium Oxide Optical Amplifiers on a Low-Loss Silicon Nitride Waveguide Platform," Master's Thesis, McMaster University, Canada (2018).

[58] R. Rolli, M. Montagna, S. Chaussedent, A. Monteil, V. K. Tikhomirov, and M. Ferrari, "Erbium-doped tellurite glasses with high quantum efficiency and broadband stimulated emission cross section at 1.5 μm," Opt. Mater. (Amst). **21**(1), 743—748 (2003).

[59] Y. A. Vlasov and S. J. McNab, "Losses in single-mode silicon-on-insulator strip waveguides and bends," Opt. Express **12**(8), 1622—1631 (2004).

[60] D. B. Keck and A. R. Tynes, "Spectral Response of Low-Loss Optical Waveguides," Appl. Opt. **11**(7), 1502–1506 (1972).

[61] L. Agazzi, J. D. B. Bradley, M. Dijkstra, F. Ay, G. Roelkens, R. Baets, K. Wörhoff, and M. Pollnau, "Monolithic integration of erbium-doped amplifiers with silicon-on-insulator waveguides," Opt. Express **18**(26), 27703-–27711 (2010).

[62] Centre for Emerging Device Technologies - McMaster University: https://www.eng.mcmaster.ca/centre-emerging-device-technologies-cedt-0

[63] V. R. Almeida, Q. Xu, C. A. Barrios, and M. Lipson, "Guiding and confining light in void nanostructure," Opt. Lett. **29**(11), 1209—1211 (2004).

[64] A. Tengattini, D. Gandolfi, N. Prtljaga, A. Anopchenko, J. M. Ramirez, F. F. Lupi, Y. Berencen, D. Navarro-Urrios, P. Rivallin, K. Surana, B. Garrido, J.-M. Fedeli, and L. Pavesi, "Toward a 1.54 μm Electrically Driven Erbium-Doped Silicon Slot Waveguide and Optical Amplifier," J. Light. Technol. **31**(3), 391-–397 (2013).

[65] P. Cheben, R. Halir, J. H. Schmid, H. A. Atwater, and D. R. Smith, "Subwavelength integrated photonics," Nature **560**, 565-–572 (2018).

[66] NSERC Silicon Electronic-Photonic Integrated Circuits Program: https://siepic.ubc.ca/, Accessed August 10, 2020.